Seismicity potential of geothermal operations in the North Sea Supergroup in the Roer Valley Graben

TNO Publiek | ONGERUBRICEERD Releasable to the public
TNO 2024 R12041
24 January 2025

Energy & Materials Transition
www.tno.nl
+31 88 866 42 56
info@tno.nl

TNO 2024 R12041 – 24 January 2025

Seismicity potential of geothermal operations in the North Sea Supergroup in the Roer Valley Graben

Author(s)	Frans Aben, Loes Buijze, Peter Fokker, Hans Veldkamp, Maartje Koning
Classification report	TNO Publiek | ONGERUBRICEERD Releasable to the public TNO Publiek
Report text	TNO Publiek
Number of pages	110 (excl. front and back cover)
Number of appendices	4
Sponsor	Energie Beheer Nederland B.V.
Project name	Studie naar seismiciteit bij ondiepe geothermie in de Roerdalslenk
Project number	060.59772

Contents

Contents

Executive summary

There is increased interest in the Netherlands in shallowly buried (<1500 m) sedimentary formations of Cenozoic age as potential reservoirs for geothermal heat production. The geothermal potential of such formations, all belonging to the North Sea Supergroup, is particularly high in the Roer Valley Graben (RVG), where extension in the recent tectonic history has resulted in thick and relatively deeply buried sequences of Cenozoic sediments. As for all geothermal projects, such projects will need to comply with the Mining Law and ensure safe geothermal production in terms of seismic hazard. The RVG is currently seen as a potentially high-risk area for geothermal exploitation, as natural seismicity occurs in the area (see section 2.1). Prior doublets in this area targeting Dinantian carbonates have been associated with events up to M_L 1.7 (Vörös & Baisch, 2022). However, for the shallower siliciclastic, poorly unconsolidated Cenozoic sediments that are also present in the RVG the potential for induced seismicity will likely be low(er), as a substantial contribution of inelastic (plastic) deformation is expected. Therefore, Energie Beheer Nederland B.V. (EBN) has commissioned TNO to investigate a first order reactivation potential and seismogenic potential of faults in the Cenozoic North Sea Groups in the RVG. The study considers the typical depth ranges and reservoir properties of the North Sea Group sediments in the RVG, and the effects of an inelastic reservoir reponse.

This study consists of the following components:

- Literature review and analysis of the KNMI seismicity catalog to assess whether there is evidence for prior natural seismicity nucleating in the North Sea Groups in the RVG.
- Inventory of currently-known reservoir, rock and fault properties, in-situ stresses and pressures of the North Sea Group sediments in the RVG. This inventory was used to generate an input deck for the geomechanical modeling of fault reactivation, and to identify gaps in available data which should be addressed in future data acquisition campaigns.
- Model study of fault reactivation due to geothermal operations at a few case study locations in the RVG, using the SRIMA (Seal and Reservoir Integrity Mechanical Analysis) tool that is currently used for fault reactivation in the policy domain (Fokker et al., 2023). In this tool, linear elasticity in assumed in the reservoir.
- Exploratory models of inclusion of elasto-plastic reservoir behaviour, using a Finite Element model. This model was applied to the same case study locations, and the output was compared to the linear elastic reference case (e.g. the SRIMA assumptions)

Within the framework of this study, it is essential to realize that fault reactivation does not equal seismic fault slip. For faults to become seismogenic, 1) the reactivation of such faults is required, and 2) the fault friction behaviour and nucleation length scales should be such that a dynamic instability can nucleate and emit seismic waves. In this study the focus lies primarily on the first step, fault reactivation, which was addressed by the model activities described above. It was beyond the scope of the study to perform extensive scenario-based modelling or address wide ranges of uncertainties in the modelling studies. The obtained first order responses can be used to define and steer follow-up modeling studies.

The results of each study component are summarized as follows:

The literature review indicated that the RVG's seismicity is primarily confined to deeper formations, with limited evidence of shallow seismic activity in the North Sea Supergroup. Historical geological records indicate significant surface-rupturing events, likely driven by the weight of the icesheets in glaciation periods, but these have not been observed in recent times. Note that such events likely nucleate at greater depth, but then propagate to the surface. The shallow events listed in the KNMI catalogue proved to have in fact an undefined hypocenter depth, as their depth could not be defined due to sparse network coverage and was set to a default value of 1.0 km depth. Further studies and improved seismic monitoring are therefore needed according to current literature to fully understand the seismogenic potential of the shallow sediments.

The data inventorisation indicated that there is a general lack of reliable data for the North Sea Group layers in the RVG due to limited and poor-quality data collection from few oil and gas exploration wells. Core data and petrophysical evaluations are rare. In general, the Breda Formation's composition varies significantly across different wells, making it difficult to provide a single lithological succession for the RVG area. Therefore, to understand the impact of these geological variations, four generic, but realistic case study locations were selected for the simulatiosn, aiming to represent different thicknesses, fault patterns and depth locations of the sediments of the RVG system.

The SRIMA calculations showed that in a substantial fraction of simulations (40-80%) fault reactivation was observed, under the conservative assumption that the fault is located near the injection well. When the fault is located further from the injection well, the probability for reactivation is reduced. In particular when the fault lies outside the cold front (i.e. for the cases here >300 – 500 m from the well). The probability for reactivation increased with injection time, injection volume, Young's modulus, reservoir thickness, and thermal expansion coefficient. However, including elasto-plastic reservoir behavior also has a non-negligible effect on the stress path, with fault stresses becoming less critical than in the linear elastic (SRIMA) case. Hence, including this more realistic reservoir behavior would lead to lower probabilities of reactivation. Moreover, as stated earlier, fault reactivation does not equate seismic slip. Though circumstantial, most literature evidence points towards a low probability of earthquakes nucleating within the North Sea Supergroup, and the typical friction parameters of siliciclastic material at the depths and temperatures of interest are also typically stable.

We strongly recommend that the seismogenic potential should be studied further by a combination of follow-up modeling, laboratory studies on fault stability, and local monitoring near future projects or active faults in the RVG. In addition, model results showed that the applicability of SRIMA (or any geomechanical simulation which assumes linear elasticity) may not properly represent material behaviour and stress build-up in the poorly consolidated reservoirs in the North Sea Supergroup. Hence, improvements of SRIMA or the use of alternative methods is recommended.

1 Introduction

1.1 The Roer Valley Graben

The Roer Valley Graben (RVG) is part of a rift system that has been active in the Mesozoic and Cenozoic (Geluk et al., 1994; Luijendijk et al., 2011; Siebels et al., 2024; van Balen et al., 2021). It is part of a series of rift basins in the Alpine foreland that extend southward toward the Rhone Valley – i.e. the Rhine Graben Rift System (Luijendijk et al., 2011). The RVG forms the northwestern branch of the Rhine Graben Rift system (Geluk et al., 1994). The RVG is bounded towards the northeast by the Peel Boundary Fault, separating it from the Peel Block (Figure 1). To the southwest, it is separated from the Campine Block by the Rijen, Veldhoven and Feldbiss fault systems (Siebels et al., 2024). All have a northwest-southeast direction except for the Veldhoven Fault system which is oriented westnorthwest – eastsoutheast. The Veldhoven Fault system separates the southeastern and northwestern parts of the RVG, which have undergone a different tectonic evolution (Geluk et al., 1994), and therefore have a different sediment infill (see Figure 7).

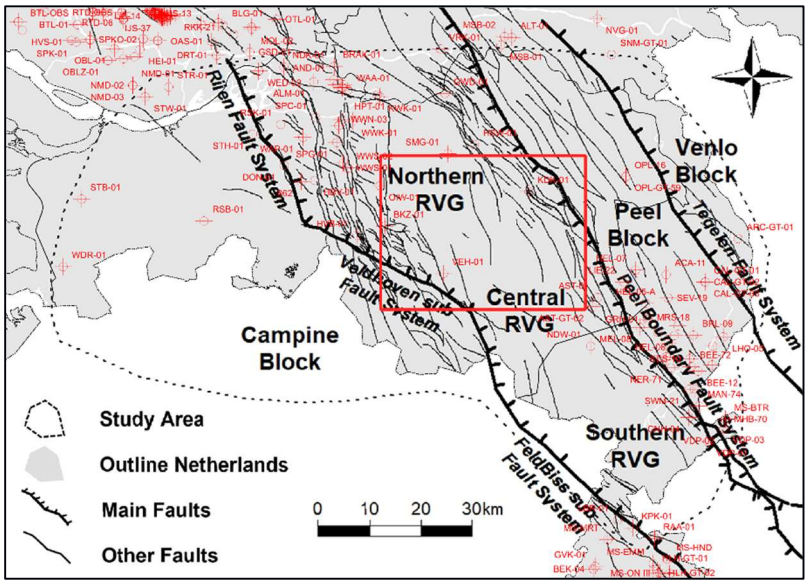

Figure 1 Location of the study area outlined in red, in relation to the structural elements, in between the 'northern' and 'central' RVG. Source: modified after (Siebels et al., 2024).

1.2 Main stratigraphic units in the Roer Valley Graben

In the RVG, a thick Permian-Triassic-Jurassic sequence was deposited. Outside the Graben this sequence was in some places eroded during Jurassic and Cretaceous erosion (Geluk et al., 1994). During the Cenozoic the RVG started to subside again. Subsidence curves for the Nederweert (NDW-01), Veldhoven (VEH-01) and Sint Michielsgestel (SMG-01) wells show a similar pattern of slow subsidence at the start of the Cenozoic, accelerating about halfway into the Cenozoic (Geluk et al., 1994; Zijerveld et al., 1992)– the Peel boundary fault was reactivated during the Late Oligocene, and increased subsidence along this fault is seen in the Miocene (Geluk et al., 1994). This is illustrated by the distribution of the members of the

Oligocene Veldhoven Formation (see Appendix C), where the older Voort and Wintelre Members can be found within and outside of the RVG, but the youngest Someren Member is only distinguished within the RVG. The direction of maximum extension changed from WNW-ESE to NW-SE over the Oligocene – Miocene boundary leading to new depocenters of subsidence for the Breda Formation(Michon & van Balen, 2006). The Early Miocene Unconformity (EMU) marks the boundary between the Veldhoven and Breda Formations. The Miocene sequence in the RVG is less well studied than that of the surrounding high blocks (Campine, Peel, Venlo) because of the deeper burial. The succession in the graben is therefore also thicker than on the surrounding blocks which helps in better understanding the internal structure of the Breda Formation (Munsterman et al., 2019b; Siebels et al., 2024). The depocenter was located in the southerneastern part of the RVG during the Early and Middle Miocene (Siebels et al., 2024). Marginal marine sands with continental elements, and open marine sands are deposited in the SE RVG, whereas mainly open marine sands are present in the C RVG . A hiatus from the latest Serravallian to the earliest Tortonian marks the mid-Miocene unconformity (MMU), which is the boundary between the lower part of the Breda Formation, known as the Groote Heide Formation, and the upper part, the Diessen Formation (Munsterman et al., 2019b). Deposition continued over the MMU in the C RVG, whereas a hiatus is present in the SE RVG. After the MMU, mainly open marine sands were deposited in the SE RVG, whereas marine clays are present in the C RVG in the Diessen Formation. The Breda Formation is overlain by the Oosterhout Formation (Appendix C, Table 12). The boundary between the two is again a hiatus referred to as the Late Miocene Unconformity.

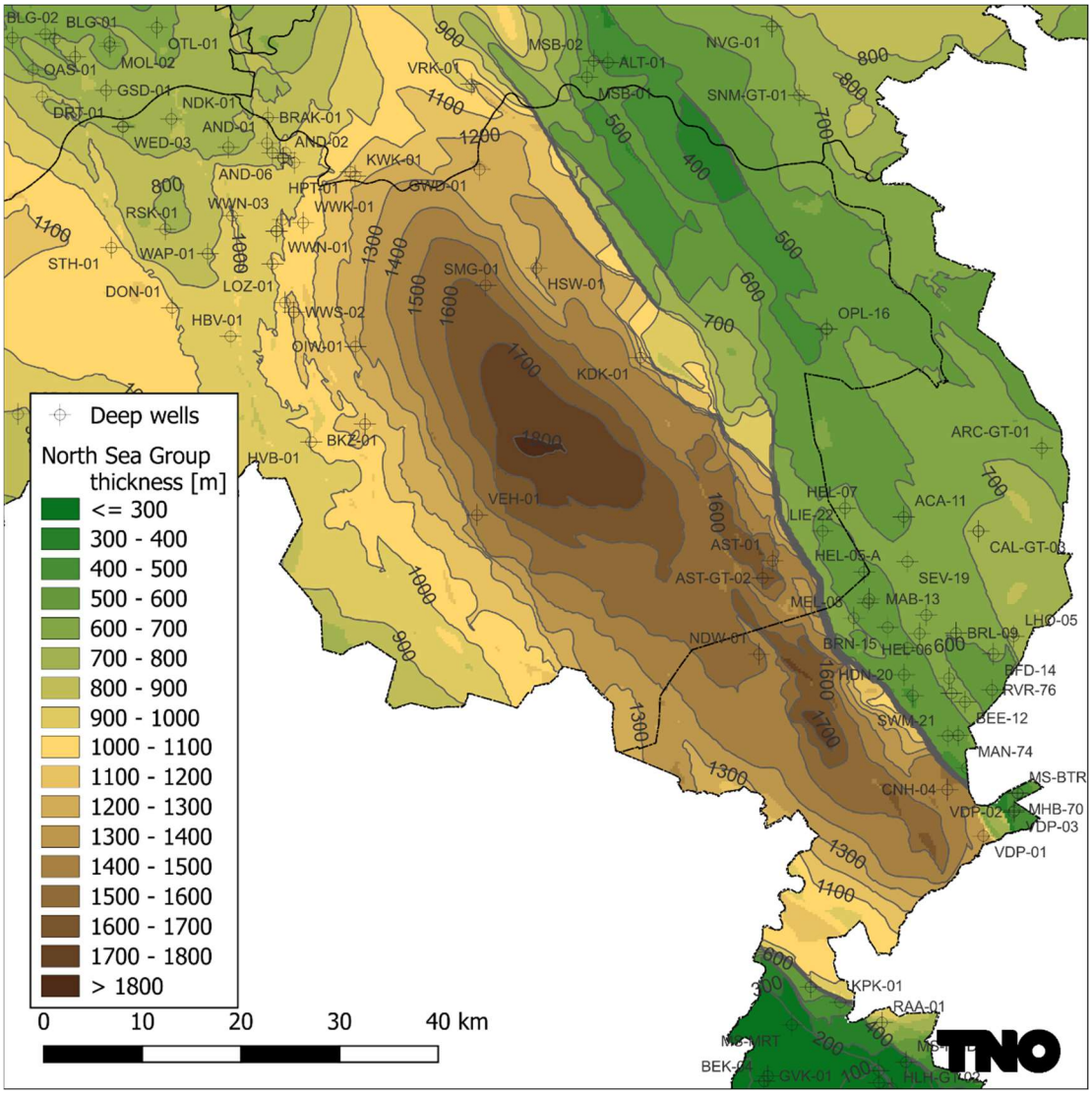

Figure 2 Gross thickness of sediments of the North Sea Supergroup in the RVG. Source: DGM v5.

1.3 Geothermal potential of North Sea Supergroup in the RVG

Porous sandstone layers within the North Sea Group have significant geothermal potential in the Netherlands (e.g., van Gils et al., 2020). Even though the reservoir temperatures are generally below 60 °C, these formations can be produced for direct-use applications with or without the aid of a heat pump. The advantage of these formations is their widespread occurrence, and cheaper drililng costs compared to deeper targets. In many places, the North Sea Group is buried to depths of less than 500 meters, making it particularly suitable for low-temperature geothermal energy. However, in the RVG, where active extension and subsidence have occurred in the recent geological past, the thickness of sediments of the North Sea Groups is up to 1800 meters (Figure 2). Moreover, the North Sea Group in the RVG contains relatively thick sand deposits. As a result, higher temperatures can be produced in substantial volumes in this area. A more detailed overview of layers with geothermal potential in the RVG can be found in Appendix C. Large uncertainty exists about the specific size of the potential because the aquifer properties (net-to-gross, permeability) are poorly constrained.

1.4 Fault reactivation due to geothermal operations in sedimentary reservoirs

Prior studies of fault reactivation due to geothermal operations in permeable sandstone aquifers have mainly focused on deeper geothermal projects (> 1.5 km depth) (Buijze et al., 2022; Hutka et al., 2023; Kivi et al., 2022; Mathur et al., 2024). The results of these geomechanical modelling studies show that cooling of the reservoir is the main driver for the stress changes in and near the reservoir and on faults in the reservoir. Near the well and early in the injection period, and in lower-permeability reservoirs, pressure increases, and poro-elasticity also play a role. All these studies assumed linear elastic reservoir behaviour.

The possibility of seismicity during geothermal activities in the shallower North Sea Supergroup formations of the RVG has not been previously investigated. This knowledge is necessary for further development of geothermal projects in these formations, for example, to prepare an appropriate Seismic Hazard and Risk Analysis (SHRA). Much is still unknown about the North Sea Groups, and there is only one geothermal site developed in the Netherlands that extracts geothermal energy from these formations.

1.5 Ingredients for seismic fault slip

It is essential to keep in mind that fault reactivation does not equate to seismic fault slip. Faults, once activated, start to slip slowly to relieve the strain on the fault. Slip may then accelerate in an unstable runaway manner to slip rates of >0.1 ms^{-1}, radiating seismic waves – i.e. an earthquake. In this case the fault is seismogenic. However, slip on the fault may also remain stable, meaning that the fault is not seismogenic. The slip behaviour, or fault stability behaviour, is determined by two factors:

- The intrinsic fault material behaviour. Unstable slip requires that significant weakening of fault friction or strength occurs as the slip or slip rates on the fault increase. This is called slip-weakening or velocity-weakening behaviour. As the fault weakens, stored elastic strain energy is released from the medium around the fault. Part of the energy is consumed by fracturing and frictional processes on the fault during rupture and slip, and part of the energy is emitted as seismic waves.

- The size of the reactivated area. A slip patch on a fault with unstable, velocity-weakening behaviour only develops into an earthquake if the area that slips can grow sufficiently large. This is known as the critical nucleation zone size (or nucleation length, whereby a circular geometry of the nucleation zone is assumed) and is dependent on fault friction characteristics and bulk material properties. The size of the fault area where the strength of the fault is surpassed needs to be of the same order as the nucleation length.

In this study the main focus is on fault reactivation; it is beyond the scope of the study to explore the slip- or rate-weakening aspects in the modelling analysis. However, we address the seismogenic potential of faults in the shallow sediments through the literature review of natural seismicity in Chapter 2. The most direct method of establishing whether faults in the RVG may already be critically stressed and can host and nucleate earthquakes, is to analyze whether seismicity has been observed on them (Section 2.1), or whether paleoseismic constraints have been found (Section 2.2). In addition, the likely rate-dependency of friction of unconsolidated sediments and the implication for seismic slip on faults in the RVG is discussed (Chapter 5, Discussion)

1.6 Current approach for seismic hazard analysis of geothermal projects

The Mining Law (version July 2023) requires of all geothermal operators that the expected surface movements (subsidence, seismicity) are described in the license applications. When applicable, also a description of the expected safety risks for the neighbouring population, the corresponding mitigation measures to avoid surface movements, and the measures that are taken to prevent damage at the surface must be provided. For seismicity, each project needs to perform a Seismic Hazard and Risk Analysis. A methodology for such an SHRA has been proposed by TNO-AGE and EBN (https://www.nlog.nl/sdra-geothermie-integriteit-afdichtend-pakket). This methodology has so far been applied to geothermal projects deeper than 1500 m – in this study its use for fault reactivation in shallower targets will be explored.

The methodology consists of multiple steps (Figure 3). First, a seismic hazard screening step (SDS) is performed. In this screening, a number of questions need to be answered, e.g. relating to data quality, overlap with other mining activities, or overlap with a major fault zone. There is also a criterion with relates to the RVG. If the reservoir is located within or overlaps with the RVG, additional seismic hazard analysis is required. In case the reservoir within the RVG is located within the North Sea Supergroup, the Standard Extensive SHRA needs to be applied to the project. If the reservoir is located in another litho-stratigraphic group, automatically a site-specific custom SHRA (Maatwerk SDRA in Figure 3) is required.

The Standard Extensive SHRA requires that the Largest Credible Earthquake magnitude is defined. This is analogous to the hazard screening methodology for Dutch small gas fields (SODM, 2016) and uses the affected fault area as a proxy for the resulting induced magnitude. For geothermal projects the SRIMA (Seal and Reservoir Integrity Mechanical Analysis) can be used, which will also be used in Section 4.1. In this tool, pressure and temperature changes in a horizontal seal-reservoir-base sequence around an injection well are computed. The resulting stress changes are transformed onto a fault plane and the reactivated area is computed and converted to magnitude. Note that some major assumptions lie at the basis of this model. In reality, slip on a fault may occur through progressive smaller events, slip on a fault may not be seismic, and slip may also propagate beyond the reactivated fault zone due to stress transfer. Hence, the concepts of seismic slip and fault stability as described in the previous section are not accounted for in this methodology. Also, contrary to the SHRA that is in place for the Groningen gas field (TNO, 2020), there is no calibration against observations, because for geothermal projects almost no seismic events have been recorded.

One of the questions is to what extent the stress changes computed in SRIMA, that, in addition to the above assumptions, were computed assuming linear elastic reservoir behaviour, are suitable for modelling of fault reactivation within North Sea Supergroup sediments in the RVG. This question is further addressed in the discussion in Chapter 5.

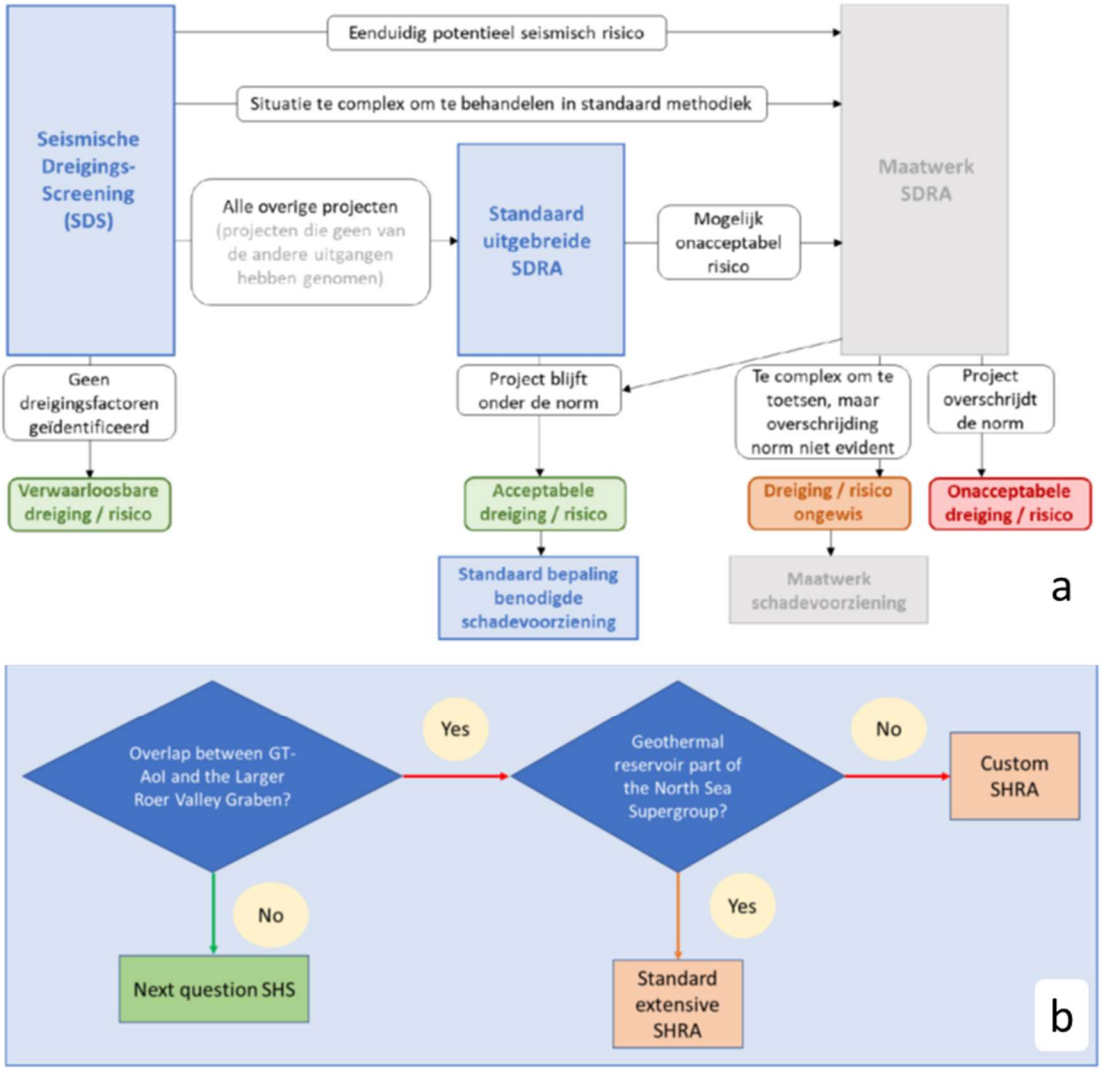

Figure 3 Methodology for seismic hazard and risk analysis for geothermal projects below 500 m (Mijnlieff et al., 2023).

1.7 Layout of the report

In Chapter 1 general background on the RVG, and the geothermal potential is provided. The state-of-the-art of fault reactivation studies in the framework of Dutch geothermal sector is summarized, as well as the ingredients required for seismic slip and the current Seismic Hazard and Risk Analysis (SHRA) methodology for geothermal projects in the Netherlands.

In Chapter 2 the review of observed seismicity in the RVG is summarized.

The data inventory of the North Sea Groups is summarized in Chapter 3. The lithological units of interest are identified, and the four case study locations used for the model simulations are introduced. The data inventory includes: reservoir hydrological parameters, in situ fluid properties, thermal and (thermo-) elastic properties, fault friction properties, plastic bulk properties and fault geometry. Values for the initial state of stress prior to geothermal activity are obtained from logs and well test data. The main data gaps that were idenified were well

and core based lithological descriptions and core derived porosity and permeability measurements, to be used for calibration of existing petrophysical evaluations.

Using the data inventory compiled in Chapter 3, simulations were performed for four case studies at three locations in the RGV. Where available, data is listed for these three locations. Where no location-specific data was available, data considered representative for the RVG was used. We explored two different material behaviours: a) Cold water injection into a poro-thermo-elastic reservoir (section 4.1), and b) cold water injection into an elasto-plastic reservoir (section 4.2). In Chapter 4.2 the first order effects of including inelastic reservoir behaviour were evaluated with DIANA Finite Element analysis. For the DIANA FEA models, pressure and temperature output from SRIMA were prescribed for the simulations, and Modified Cam-Clay plasticity was prescribed in the reservoir.

Chapter 5 discusses the main findings of the study and the applicability of the SRIMA method for poorly consolidated sediments, such as the North Sea Supergroup formations. Then, we discuss how fault reactivation potential changes when considering plasticity in addition to elastic behaviour. We then consider the implications for seismic hazard assessment in the RVG. Finally, we look at other considerations and discuss the gaps in data identified during this study, followed by recommendations to reduce these gaps.

Chapter 6 lists the conclusions and recommendations of this study.

2 Literature review on seismicity in shallow sedimentary formations

The RVG is a tectonically active area of continued normal faulting, resulting in abundant recordings of natural seismicity. The faulted strata are observed at depths of a few km's, but also in the shallow subsurface. It is not yet fully established whether the relatively shallow North Sea Supergroup sediments partake in the seismic activity: can faults within the North Sea Groups nucleate seismic events (i.e., are they seismogenic), and can they host earthquake ruptures from depth? An affirmation of the first question has direct implications for geothermal activity and the potential of such activities to induce seismic events. The answer to the second is of less importance for induced seismicity but remains valuable for triggered seismicity and for hazard assessments. In this section, we attempt to answer these questions by using existing data sources. We focus on the following data sources:

- Scientific literature on seismic activity in the shallow formations of the RVG.
- Recorded seismicity in the RVG.
- Scientific literature on seismic activity in similar type of settings and sedimentary formations world-wide, that may act as a precedent for seismic activity in the RVG.

From the above-mentioned data sources, we can establish whether the faults in these shallow formations are seismogenic and/or can host earthquake ruptures through two approaches:

1) Direct evidence of earthquake nucleation in the North Sea Groups. This can be established from epicentral locations (i.e., locations of nucleation) in seismic event catalogues. This approach covers a few decades of recordings of tectonic history.

2) Evidence of earthquakes from the geological record. This may establish if the studied fault can host events from depth by allowing rupture propagation but cannot determine earthquake nucleation.

2.1 Observed seismicity in the RVG

The tectonically active RVG can be described as an area with natural seismicity. A recent analysis of the seismicity in the area was performed by (Panterra, 2021).
The seismic activity is thought to be confined mostly to the mid- and lower crust in formations well below the North Sea Supergroup formations of interest. To check this assumption, during the current study the KNMI catalogues for tectonic and induced earthquakes (https://www.knmi.nl/kennis-en-datacentrum/dataset/aardbevingscatalogus) were analysed for seismicity on faults crosscutting the North Sea Supergroup sediments of the RVG. The catalogues include events recorded up to 19-03-2024, the minimum recorded magnitude M_{min} varies throughout the record with continued improvements of the seismic monitoring network. The KNMI catalogue does not include the uncertainty in depth determination, but the KNMI has published several maps for lateral and depth uncertainties in event locations (Ruigrok et al., 2023). We have combined these uncertainty maps with the catalogue.

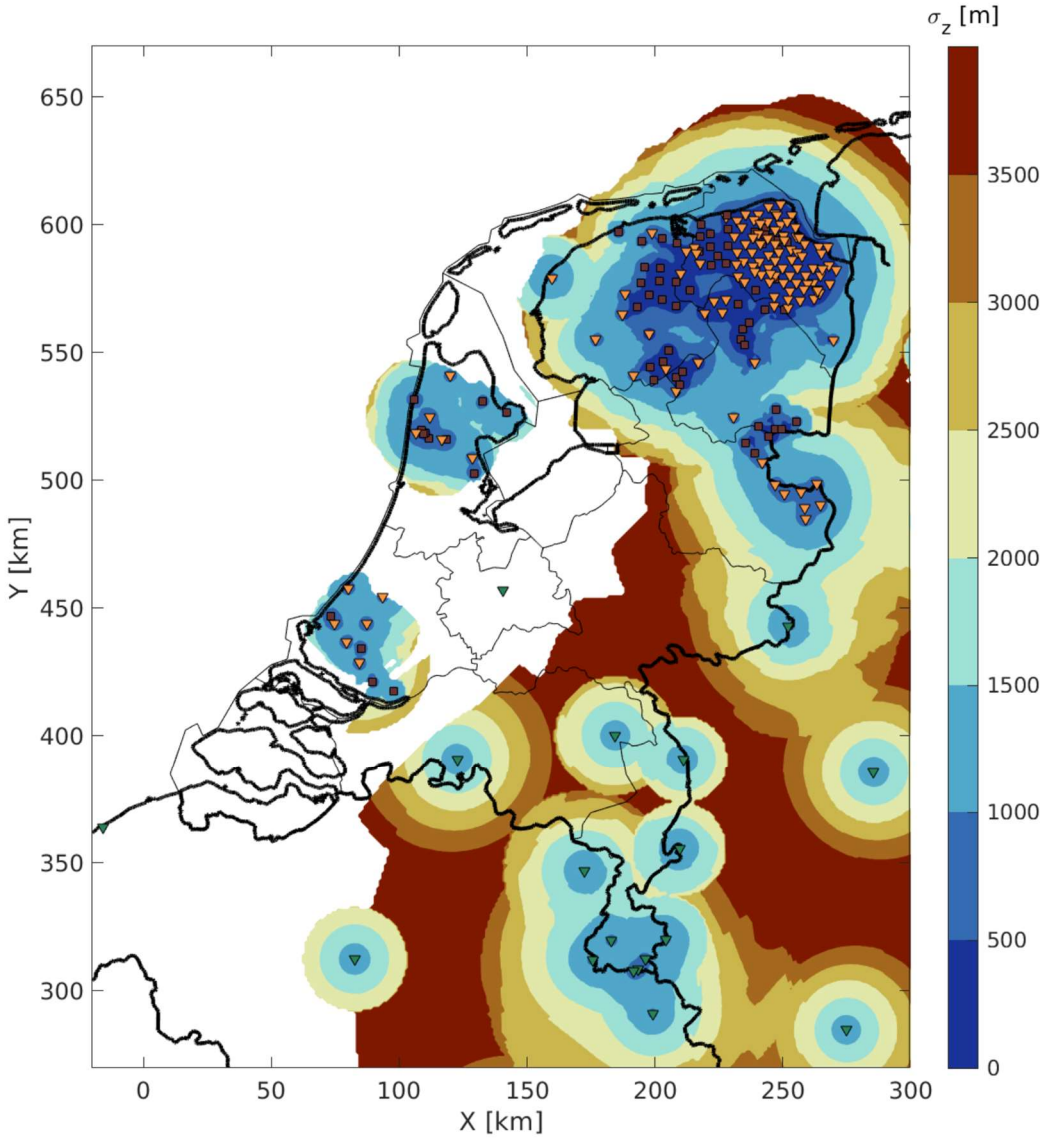

Figure 4: Hypocentre location depth uncertainty map for M1.5 events at a reference depth of 3 km, for the year 2022. Events of this magnitude can likely not be detected in the white areas. Markers indicate a variety of sensors Figure from (Ruigrok et al., 2023) (Figure D.11).

First, both catalogues were filtered spatially on the region of interest that includes the RVG (Figure 5, top panel). Zero induced events and 203 tectonic events occurred in the area. Of these events, 4 events date from the 1930's, 9 from between 1964 and 1987, and the remainder were recorded after 1990. The highest magnitude recorded was the Roermond 1992 M5.8 event. Most events were located in the south-east extremity of the Dutch RVG system, with a few events observed in the centre and north-western parts (Figure 5, top panel). The majority of events occurred in the middle crust between 5 and 25 km depth (Figure 5, centre panel). Three events were located well within the North Sea Supergroup depth range, at 1 km depth (Figure 5, centre panel; square markers on Figure 5, top panel).

We then combined the uncertainty maps with the catalogue: The maps contain the spatial uncertainty for a given magnitude event, at a reference level of 3km depth (see Figure 4 for an example). The uncertainty is unlikely to deviate much when another reference level is considered (KNMI, pers. comm.). It is assumed that the location uncertainties follow a

Gaussian distribution (Ruigrok et al., 2023). The maps are updated regularly with continued addition of new monitoring sites that improve the location certainty. Here, the uncertainty was applied to the filtered event catalogue by simply linear interpolation of the spatial-magnitudal locations of the events on the uncertainty tables. For temporal interpolation we only had access to uncertainties for the recent years 2021, 2022, and 2023. Since most events occurred before this time period, we took the mean uncertainty of these three years. The computed depth uncertainties are thus an underestimation for events prior to 2021, since the network at those event times likely yielded larger uncertainties.

The resulting standard deviations for the events in the RVG are shown in Figure 5 (bottom panel). This shows that there is some possibility that some of the recorded events occurred in the North Sea Supergroup, or that the three shallowest events occurred well below the base of the North Sea Supergroup. We mark these as initially suspect events for further analysis below. The suspect events are identified as such if its standard deviation overlaps with the top 1800 m. (summarized in Table 1). This is a conservative threshold: 1800 m is the greatest depth of the base of the North Sea Group in the RVG, at most localities the base will be at shallower depth.

Five suspect events were identified (Table 1). Three of these events have an undefined source depth, meaning that the KNMI's earthquake localization operational algorithm cannot place constraints on the depth solution of the inversion (KNMI, pers. comm.). For these undefined source depths, the algorithm allots a value of 1.0 km (hence why they appear as suspect in our analysis). A refined relocalization analyses can provide a depth constraint for undefined events, if sufficiently covered by seismometer stations (e.g., (Spetzler, 2023)): The study by (Hinzen et al., 2020), which comprised an extensive reanalysis of seismic data recorded between 1995-2018 in the Northern Rhine Area, includes an update of the hypocentre locations. The area around Roermond is included in this reanalysis. Of the 3 undefined depth locations in Table 1, the event near Maria-Hoop was included in the relocalized catalogue. The new hypocentre depth of this event is set to 8.6 km (Hinzen et al., 2020); i.e., it is not suspect anymore in our analysis. Another result is that no events near Roermond are located above 2 km depth (Figure 7 in (Hinzen et al., 2020)). Unfortunately, relocation of the other two undefined events may not be feasible due to a lack of sufficient station coverage (KNMI, pers. comm.). In particular, the Mariahout event located in the centre of the RVG is not well covered (see Figure 4). For the future, improved station coverage of the NW part of the RVG can greatly reduce such uncertainty in hypocentre depth location. For now, we exclude these two events from our conclusions on the depth range of natural seismicity. We do note that observed seismic nucleation in the North Sea Supergroup formations cannot be ruled out fully without reanalysis of these two particular events, when feasible.

This leaves two suspect events remaining in Table 1, the events at Sint Odiliënberg and Nederweert. These are located at 3.4 and 3.2 km depth, respectively, but with standard deviations that overlap with the top 1800 m. However, the base of the North Sea Group at these localities, based on the DGM, is at 865 m and 834 m depth. Using these local base depths, the depth uncertainty does not overlap with the North Sea Group formations.

In conclusion, observed seismicity in the RVG indicates that events for which depth constraints were determined occur below the North Sea Supergroup formations. Five initially suspect events were identified from the KNMI catalogue (Table 1), these were located at relatively shallow depth or lacked resolvable depth constraints (thereby carrying a default value of 1.0 km). Further analysis showed that three of five events were located below the North Sea Group formations, and two were discarded for undefined depth constraints.

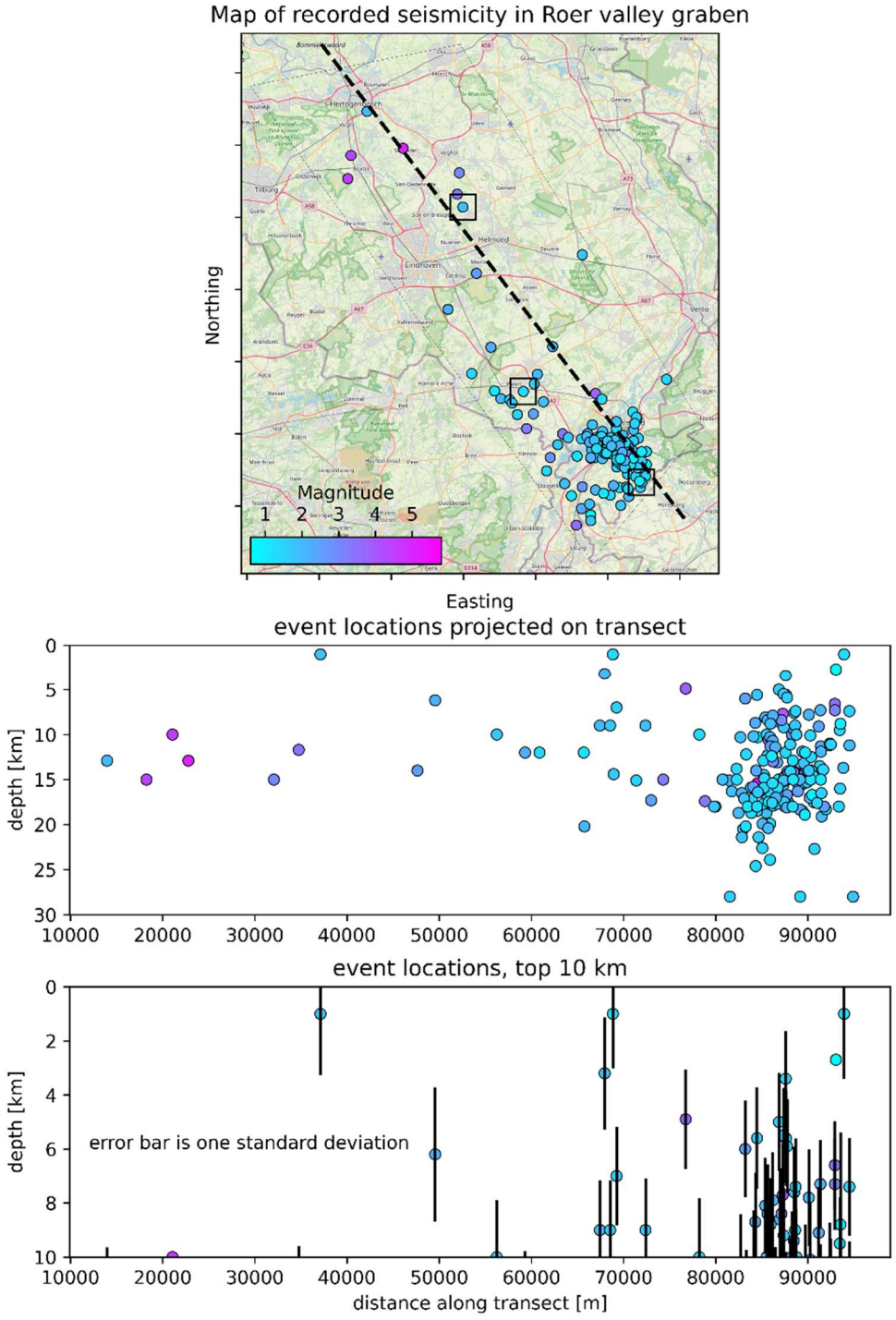
Map of recorded seismicity in Roer valley graben
Northing
Easting
Magnitude
1 2 3 4 5
event locations projected on transect
depth [km]
event locations, top 10 km
error bar is one standard deviation
distance along transect [m]

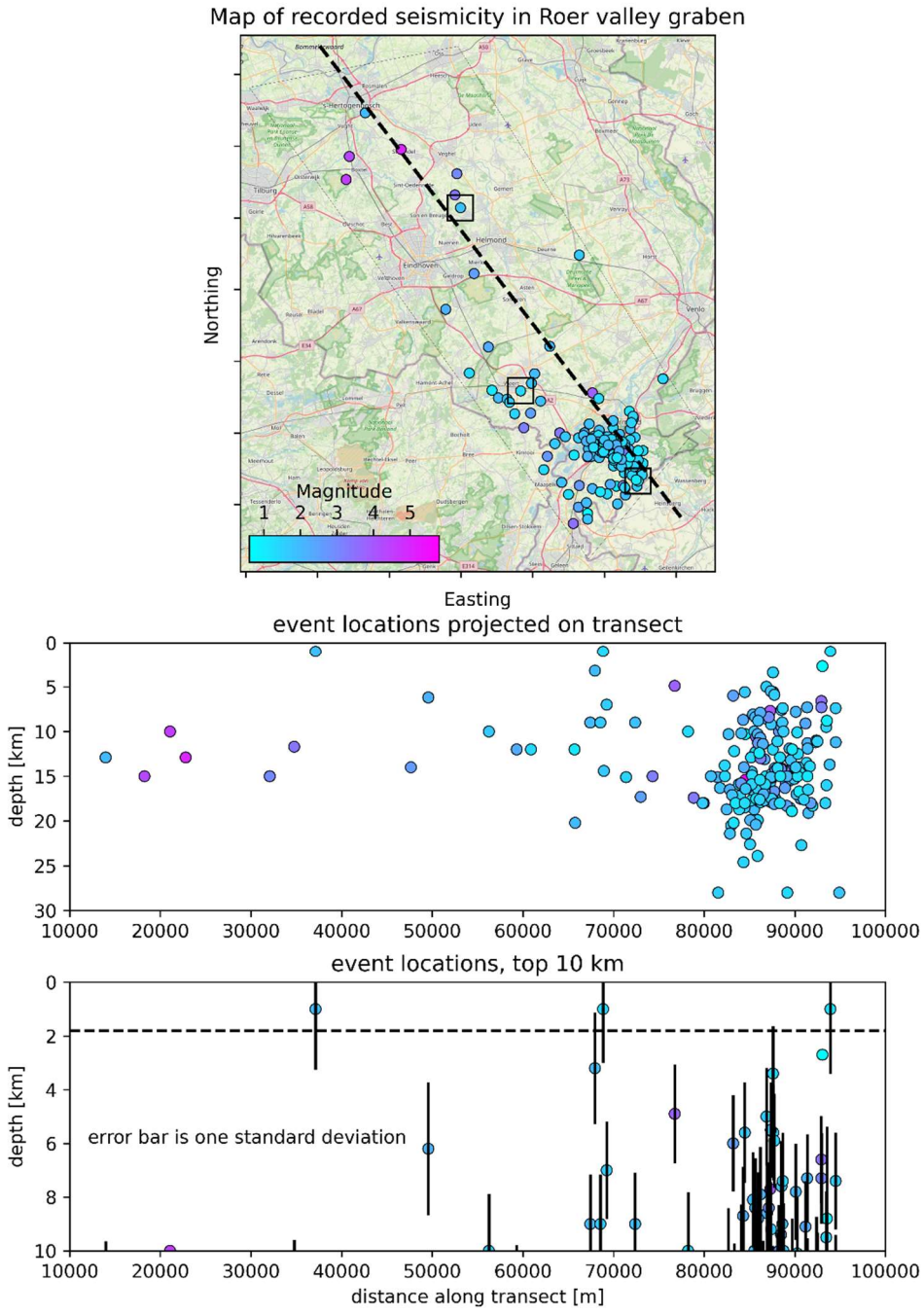

Figure 5: *Top panel:* Locations of earthquake events that occurred in the RVG approximate region of interest (delineated by the black tetragon). The colours of the event locations correspond to the magnitude of the events. The dashed line is the transect used in the panels below. Black squares indicate events that were placed at 1.0 km depth. *Centre panel:* Hypocentre depths of the events versus the horizontal distance along the transect on which they are projected. *Bottom panel:* Zoom of the first 10 km's. The dashed line represents the lower limit of the upper North Sea group formation in this region, at 1800 m depth. Thick error bars represent one standard deviation. Uncertainties were derived from the KNMI uncertainty maps (see text).

Table 1: Initially suspect shallow earthquake events in the RVG. Note that we infer that these events almost certainly did not occur in the North Sea Group formations (see text).

Geographical location	Depth [km]	Magnitude	Date
Sint Odiliënberg	3.4	1.5	13-04-1992
Nederweert	3.2	2.0	15-08-1997
Maria-Hoop	undefined* (8.6 after relocalization. by (Hinzen et al., 2020))	1.3	20-09-2006
Weert	undefined*	1.4	01-10-2020
Mariahout	undefined*	1.9	25-03-2023
*: Undefined source depths are set to 1.0 km depth in the KNMI catalogue			

2.2 Geological record for seismicity

Several publications report on the results of earthquake geology and geomorphology along the southern and northern major bounding faults of the RVG (e.g., (Houtgast et al., 2005), (van Balen et al., 2019; van Balen et al., 2021; van Balen et al., 2024)). These studies look at fault scarps at the surface and perform trenching studies for coseismic evidence in the shallow geological structural record. The results indicate that several earthquake ruptures breached the surface, resulting in surface ruptures of several 10s of km's. These events had likely magnitudes ranging between M6.2 and M7.0 and occurred in the Late Weichselian period (in the Late Pleniglacial to Late Glacial transition), between 15 ka to 13 ka. It is argued that the events, and the driving stresses, where affected by glacio-isostatic motions: The RVG area was located at the glacial fore-bulge, which collapsed during the Late Glacial period, resulting in tectonic stress changes that caused these large surface rupturing events. An additional tectonic driver is the active mantle plume underneath the Eifel area in Germany. This causes additional extensional stresses that are more pronounced in South-East of the RVG, where seismicity is higher. These seismo-tectonic considerations explain the lack of surface rupturing events on the bounding faults of the RVG in historical times, whereas several of them were measured in relatively short succession in the Late Weichselian.

In summary, the geological record reveals several surface-rupturing events that occurred on the major bounding faults of the RVG. This implies that faults cross-cutting the North Sea Supergroup formations can host sufficiently large events that nucleated at depth. Such events were likely driven by a period of glaciation and have not been observed in the last 13k years.

2.3 Seismicity in comparable formations abroad

On the large scale, for an idealized generic crust, the upper few km's of the crust are generally considered not seismogenic due to its inferred sedimentary cover (see for instance the seminal work by (Scholz, 1988)). Indeed, most observed seismicity, both tectonic and induced, occurs at depths greater than the 0 km to 2 km depth range explored in this study. The definition of "shallow" in seismological literature depends highly on context and may refer to events occurring above 15 km depth for plate-scale studies, or less than 4 km depth for induced seismicity studies in, amongst others, the Netherlands (e.g. Van Eck et al., 2006). There are exceptions, however: observations of very shallow (< 2km) natural seismicity are often linked to specific settings such as volcanoes, whereas very shallow induced events are recorded in very stiff, low porous rock (e.g., events at around 500m depth in a basaltic complex, Agurto-Detzel et al., 2017). Hence, there are no obvious cases of earthquake nucleation in comparable formations abroad.

3 Inventory of North Sea Supergroup data

In this chapter the data inventory of properties of relevant parts of the North Sea Supergroup in the RVG is summarized. The focus of the data inventory has been on those units that occur within the RVG and are currently targeted as geothermal reservoirs. Sediments belonging to the North Sea Supergroup occur in the entire onshore Netherlands (Figure 2). The thickest onshore succession is found in the RVG, both for the Upper North Sea Group (thickness up to 1300m), and the combined Lower and Middle North Sea Groups (up to 750m). It is therefore clear that most North Sea Supergroup reservoirs also have their thickest accumulation in the RVG. Most of them, belonging to the Lower and Middle North Sea Groups, have not yet been targeted with the exception of the Brussels Sand – which does not occur however in the RVG. These units will not be described in detail in this Chapter. Instead, they are outlined in Appendix C on the basis of the mapping results adapted from ThermoGIS. In this Chapter, emphasis is on the Miocene Breda Formation, which will be the target of the SCAN well that will be drilled near Eindhoven (as indicated on www.scanaardwarmte.nl).

Note that in an upcoming revision of the Breda Formation, it will be subdivided into a lower Groote Heide and upper Diessen Formation (Munsterman et al., 2019b). This proposal is followed by (Siebels et al., 2024) but it has not yet been formalised in the Stratigraphic Nomenclator of the Netherlands. In this report we refer to both the Breda Formation and the Groote Heide and Diessen Formations when applicable.

The aim of the inventory is to provide an input deck for the model simulations which are presented in Chapter 4. The data inventory is based on publicly accessible data sources from e.g. www.nlog.nl, as well as data provided directly by EBN. The data inventory covers geological properties such as formation depths and thicknesses, fault geometry, porosity and permeability, geomechanical properties, and in-situ stress. The selected parameter values for the simulations are summarized in Table 9. In addition, data gaps that were identified are summarized at the end of the chapter, as a recommendation for future data acquisition campaigns.

3.1 Data availability in the RVG

A general problem with regard to the Paleogene and Neogene layers in the RVG is the lack of reliable data. These layers were targeted by few O&G exploration wells only (Figure 6 for well locations). Because those wells targeted older stratigraphic units, data collection on Paleogene and Neogene layers was not considered important. Therefore, the data collection was often limited and of poor quality. Logs were seldomly collected extensively over the North Sea Group layers or starting at larger depth, or only after the casing was placed. Often the hole conditions were poor. Core data are rare, as are petrophysical evaluations. Within the WarmingUP and ThermoGIS projects, petrophysical evaluations were performed on wells that penetrated the Brussels Sand Member (Lower North Sea Group) and the Breda Formation. Focus for the latter was on the Zuiderzee Low and RVG areas. Apart from the fact that the quality of the log data is sometimes poor, the lack of core data prevents calibration of the evaluation results.

Sediments of the Paleogene and Neogene are buried to shallow depth in some parts of the Netherlands, such as parts of Zeeland, Noord-Brabant, Limburg and Twente. Here, detailed lithological description and measurements of the transmissivity can be obtained from shallow ground water drillings. However, it is not recommended to extrapolate this data over larger distances because of lateral facies changes, and differences in burial depth leading to compaction and diagenesis. Although at very shallow depth, porosity and permeability changes due to compaction and diagenesis are limited, a correction needs to be made when the sediments are buried to depth of hundreds of meters. The nature and size of the required corrections is at this moment unknown.

3.1.1 REGIS geo-hydrological model

Aquifers and aquitards that are part of the Upper North Sea Group are included in the Regional Geohydrological Information System (REGIS) (Hummelman et al., 2019; Vernes & van Doorn, T. H. M., 2005). The Breda Formation is the oldest unit described in REGIS. REGIS contains for all layers depth, thickness and hydraulic conductivity grids (for aquifers, the horizontal hydraulic conductivity, for aquitards, the vertical). Where the Breda Formation occurs at relatively shallow depth (<~100m), the descriptions may be considered reliable, but where the Breda Formation is buried deeply, such as in the RVG, the layer properties are based in little to no data, and/or extrapolated over large lateral and vertical distance. The REGIS model was therefore not considered as input for the current study.

Within the SCAN-program, data collection of relatively young stratigraphic units is planned, but until now only the Oranjeoord well (ORO-01) in the western part of Noord-Brabant has collected extensive data on Paleogene layers, especially on the Brussels Sand and Berg Members. However, the Brussels Sand Member does not occur in the RVG. Also, the depositional facies of the former is different from the Breda Formation. The Berg Member was also deposited in the RVG but is currently located at larger depths (~1600m), and the thickness is small (<35m). Data from the Oranjeoord well must therefore be used only with caution for the Breda Formation.

3.2 Case study locations

Three case study locations were selected (Figure 6) that form the basis for the simulations in Chapter 4. These are located along a transect across the RVG. Their locations are shown in Figure 6. They represent generic but realistic geological variations as observed in the RVG.
There are several wells in the vicinity of these cases, offering a relatively large amount of available data. The VEH-01 is characterized by a combination of NW-SE and WNW-ESE fault directions. The KDK-01 well has NW-SE as main fault direction. In addition, a case study in the middle of the RVG has been selected because the deep burial and large thickness of the Breda Formation at this location make it an attractive target for geothermal production.

@

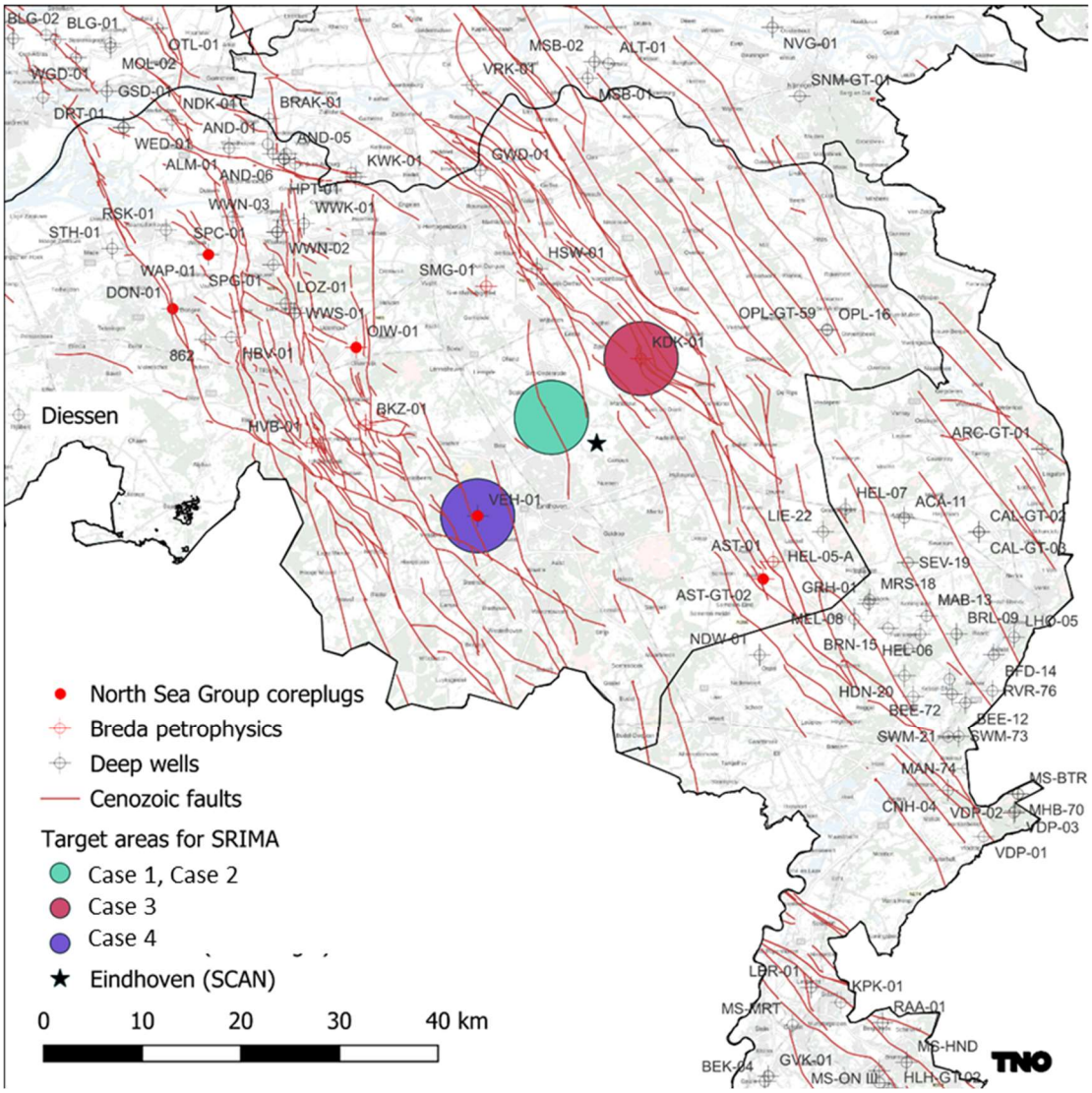

Figure 6 Deep wells and Cenozoic faults in the RVG. Coloured circles indicate case study locations (section 3.2). Note the different strike between the main NW-SE fault direction and the Veldhoven WNW-ESE system (purple circle). Source of faults: HIKE project.

3.3 Lithology of the Breda formation (based on local well data)

Owing to the limited quality and availability of extensive log suites in the deep wells of the RVG, in combination with the known complex geometry of the Breda Formation infill, it is not always possible to clearly define the depth range of the Breda Formation on basis of log interpretations. Palynological analyses are required to unambiguously define the depth range, but they sometimes suffer from low vertical resolution of the sampled cuttings, reworking and the dependence on rare species that are hard to determine. (Siebels et al., 2024) provide valuable insight into the regional geometry of the Breda Formation in the RVG because they based their interpretation on a combination of palynology, log interpretation and seismic interpretation. Figure 7, from (Siebels et al., 2024), shows that the Breda Formation as a whole mainly consists of marine sands with some continental influence in the SE, but that in the

Diessen Formation also lagoonal clays exist. The latter appears to exist especially in the central part of the graben, which is the study area.

In the absence of core data (only few Breda Formation core plug measurements are known from the well AST-GT-02), the available lithology descriptions are based on cutting descriptions which can be unreliable. This is illustrated for the VEH-01 well for which the lithology was interpreted by both the operator (NAM) and the Geological Survey (RGD). Important differences exist between the two. Generally speaking, based on petrophysical analysis of wells in the RVG (Peters et al., 2022) and Zuiderzee Low (Smit, 2022) in the WarmingUP project, the Diessen Formation shows the best reservoir quality. It should be noted however, based on (Siebels et al., 2024) that major lateral variations in lithology occur (Figure 7). Extrapolation over large distances is challenging. Results from the Zuiderzee Low are of limited relevance.

In the following sections, we describe in more detail well log data from the VEH-01 and KDK-01 wells, as well as the Asten well (AST-GT-02).

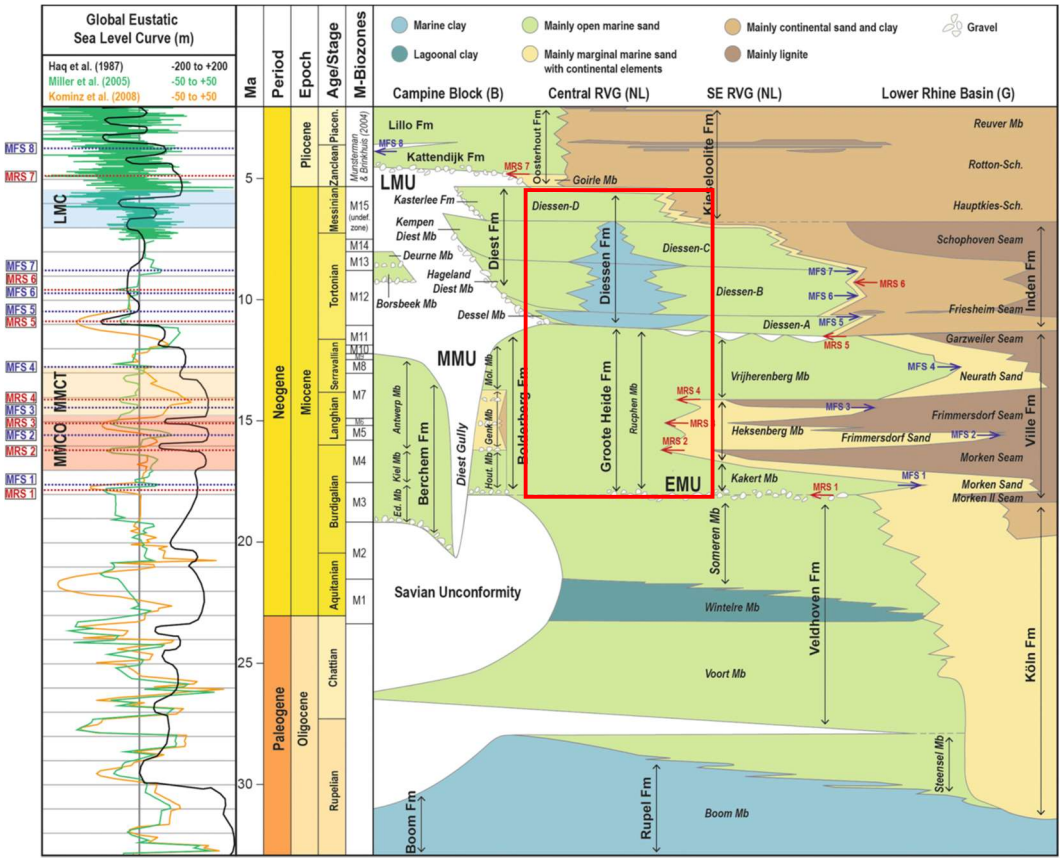

Figure 7 Schematic cross section over the Campine Block, the RVG and the Lower Rhine Basin (Siebels et al., 2024). The dominant lithology is marine sand, but in the central part of the Graben marine clay may prevail. Approximate study area outlined in red.

3.3.1 Keldonk-1

For KDK-01, a petrophysical evaluation of the Breda Formation was carried out in the WarmingUP project. The litholog of the KDK-01 well suggests that the formation consists mostly of sandy clay, but the petrophysics show a N/G >95% for most of the interval between 374 and 713 mTVD (~Diessen; NG track grey), while below this interval (~Groote Heide) the N/G is dominantly below the cutoff (20% porosity and 50% VSH; NG track green) all the way down to the bottom of the evaluated interval at 1047 mTVD (this is near the Rupel Clay). This layer could be interpreted as a bottom seal. Above the flow unit a layer interpreted dominantly as clay exists between 243 and 374 mTVD (~Oosterhout (Goirle), but the gamma ray is even lower than in the Diessen thereby suggesting that the content is more sandy than shaly which leaves the conclusion that no topseal exists at this location. It should be noted that interpretation of the net-to-gross from a gamma ray is challenging in the Breda Formation because of the presence of glauconite. This may explain the difference between the GR-based net-to-gross and the lithology description which shows mostly clay.

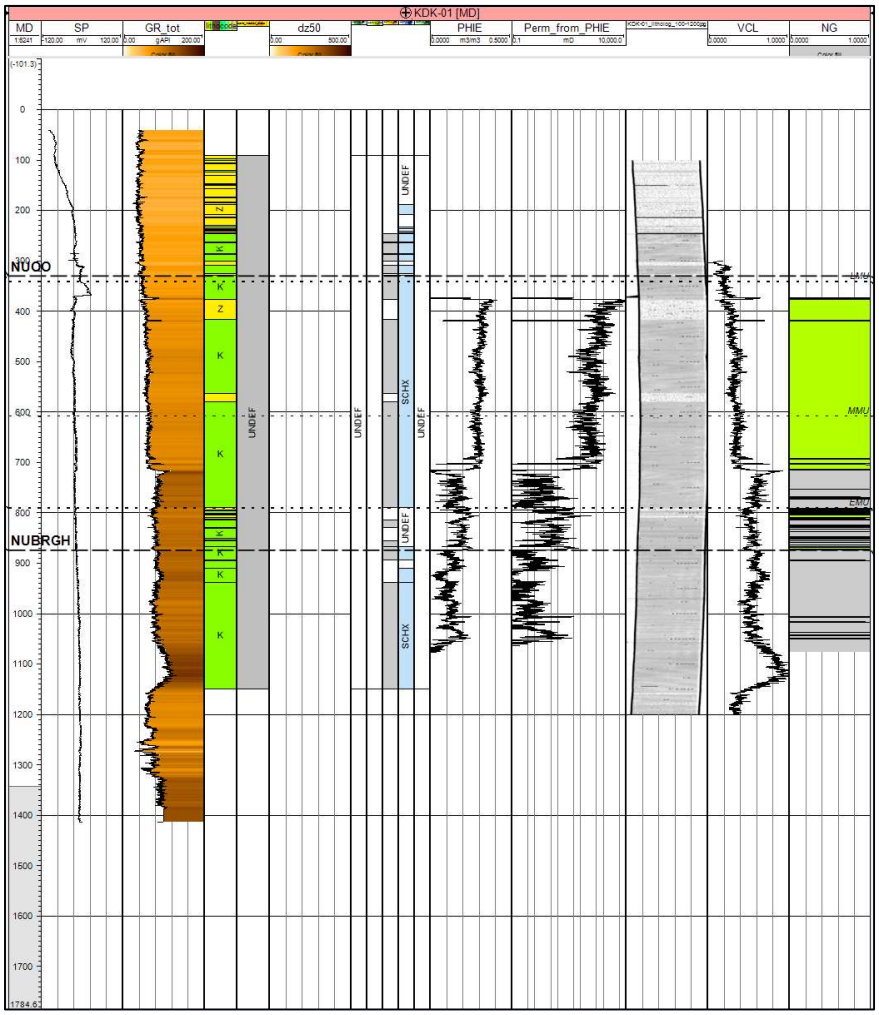

Figure 8 KDK-01 well panel. Lithology column based on the litholog, suggesting mainly clay and sandy clay. The codes in the lithology log are K=clay, Z=sand. Dashed lines welltops: NUOO=base Oosterhout=top Diessen, EMU=base Diessen, NUBRGH=base Groote Heide. Dotted lines: unpublished seismic interpretations EMU, MMU, LMU, deviations may exist with welltops.

3.3.2 Veldhoven-1

Few logs were run in the VEH-01 well, mainly an SP. The EOW (end of well report) describes the Tertiairy[1] section as 'sandy to very sandy and silty clays and various water bearing sand layers. A core obtained at a depth of 907 to 913 m (below base Breda) shows porosities between 26 and 35% and permeabilities up to 270 mD. The Breda is interpreted between 378 and 858 mTVD. The EOW describes the upper part of this section (375-685 mAH) as dominantly sandy which is in contrast to the description by RGD which states that no samples were available, and that sandy clay was interpreted on basis of the logs. The EOW description is preferred because it appears to be based on onsite cuttings descriptions. Below 685 mAH 30m of clayey sand and clay layers are found, and below 145m of sandy to very sandy locally glauconitic clays, which is in better accordance with the RGD description which describes sandy clay.

All in all, this description differs considerably from the Keldonk location which is about 25 km to the northeast but on the other edge of the Graben. The upper part is the most sandy and the lower the most shaly, but both should be considered 'ratty'. Below 860 mAH, down to ~1350 mAH, mostly clays occur which can be considered as bottom seal. Above the Breda, no top seal exists in the Oosterhout (fine sand).

[1] The Tertiairy period has become obsolete. It spanned the current Paleogene and Neogene periods.

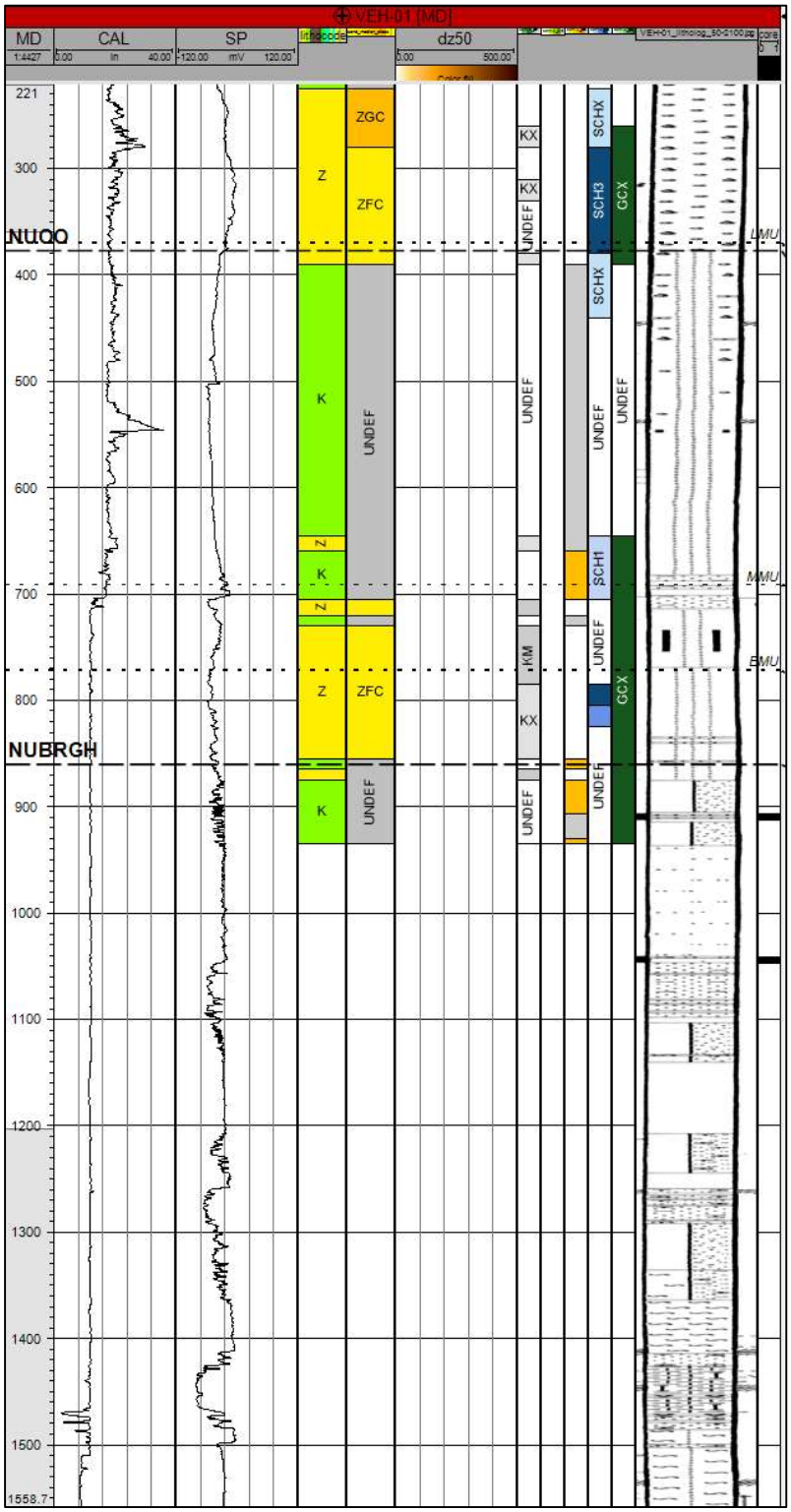

Figure 9 VEH-01 well panel. The lithocode column shows the RGD interpretation which is based on log data for the Breda interval. To the right is the litholog itself. Dashed lines welltops: NUOO: base Oosterhout, , NUBRGH: base Groote Heide. Dotted lines: unpublished seismic interpretations, deviations may exist with welltops. Lithology descriptions as for Figure 8, sand median description ZFC=sand fine category.

Figure 10, from (Siebels et al., 2024) shows the BKZ-01 well, close to VEH-01 in relation to the Groote Heide and Diessen Formations. Whereas the layering in the Groote Heide Formation is largely parallel, the Diessen Formation consists of clinoforms of which the top sets are cut by the overlying Oosterhout Formation. It illustrates that it is difficult to correlate the lithology in adjacent wells over larger distances as different Diessen subunits exist in different locations (DSN-A through -D).

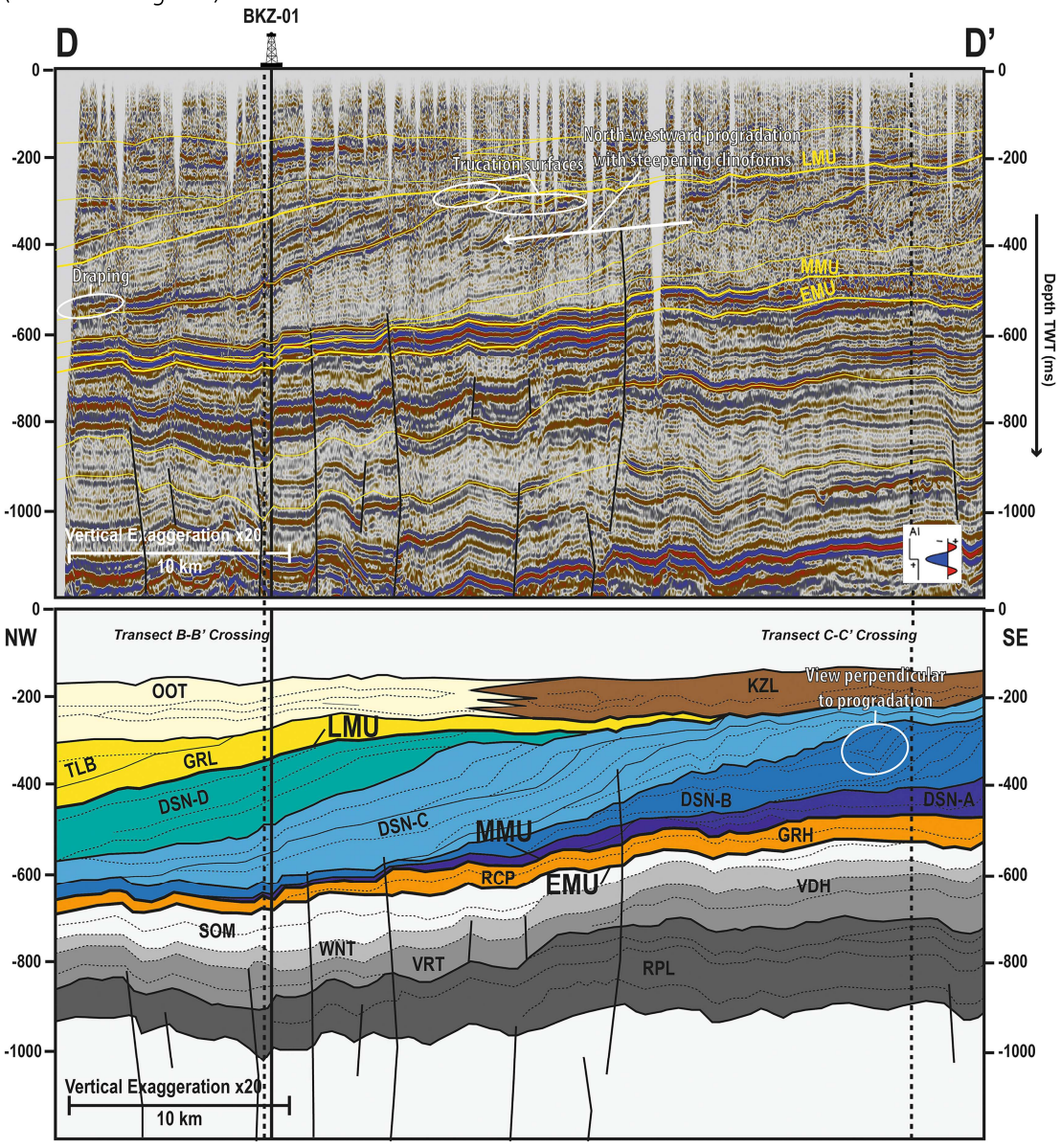

Figure 10 NW-SE seismic section parallel to the basin axis. The BKZ-01 (Broekzijde) well is located slightly NW of VEH-01 and therefore the succession is comparable. Source: (Siebels et al., 2024). RPL Rupel Fm, VDH Veldhoven Fm, VRT Voort Mb, WNT Wintelre Mb, SOM Someren Mb (all Veldhoven Fm), GRH Groote Heide Fm, RCP Rucphen Mb (Groote Heide Fm), DSN[B-C-D] Diessen Fm, OOT Oosterhout Fm, TLB Tilburg Mb, GRL Goirle Mb (both Oosterhout Fm) and KZL Kieseloolite Fm.

3.3.3 Asten-GT-02

The Asten GT-02 well is located about 25 km to the southeast of KDK-01. In contrast to the latter well, here the Groote Heide appears to have a better reservoir quality based on the net-to-gross but it should be noted that for the Groote Heide it is only based on the VCL and not

on the PHIE. Above the Breda Formation, the Oosterhout does not appear to have top sealing capability, consisting of find and coarse sand. Below the Breda, the Veldhoven Formation is clayey according to the lithological description, but the VCL is below the cutoff.

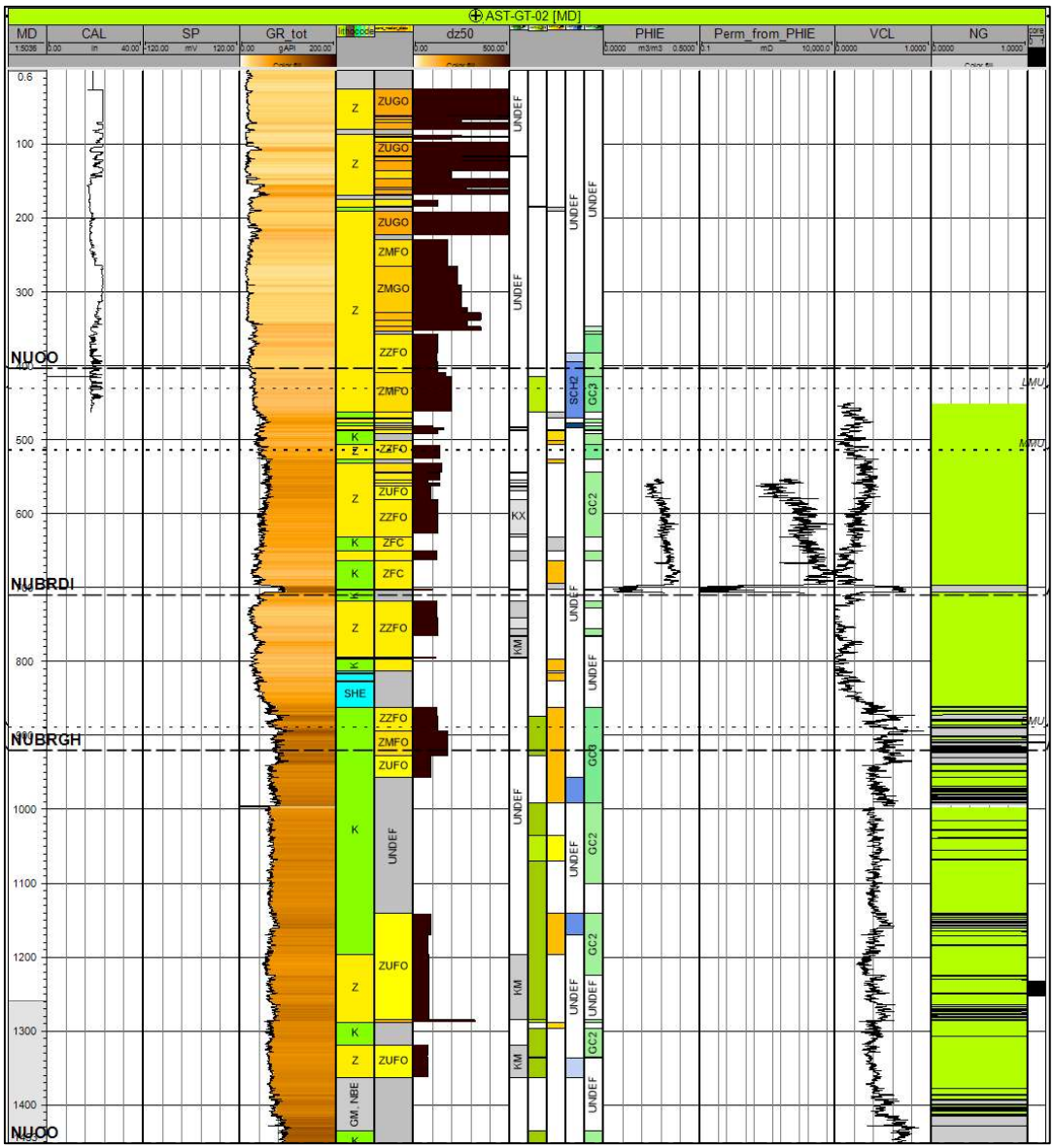

Figure 11 AST-GT-02 well panel. The litholog shows for the Breda a succession of clayey (very) fine sand and sandy clay. Lithology descriptions as for Figure 8, SHE=shells. Sand median size ZUGO=sand very coarse, ZMF(O)=sand moderately fine, ZZF(O)=sand very fine, ZUF(O)=sand extremely fine, ZFC=sand fine category. Dashed lines welltops: NUOO: base Oosterhout, , NUBRGH: base Groote Heide. Dotted lines: unpublished seismic interpretations EMU, MMU, LMU, deviations may exist with welltops.

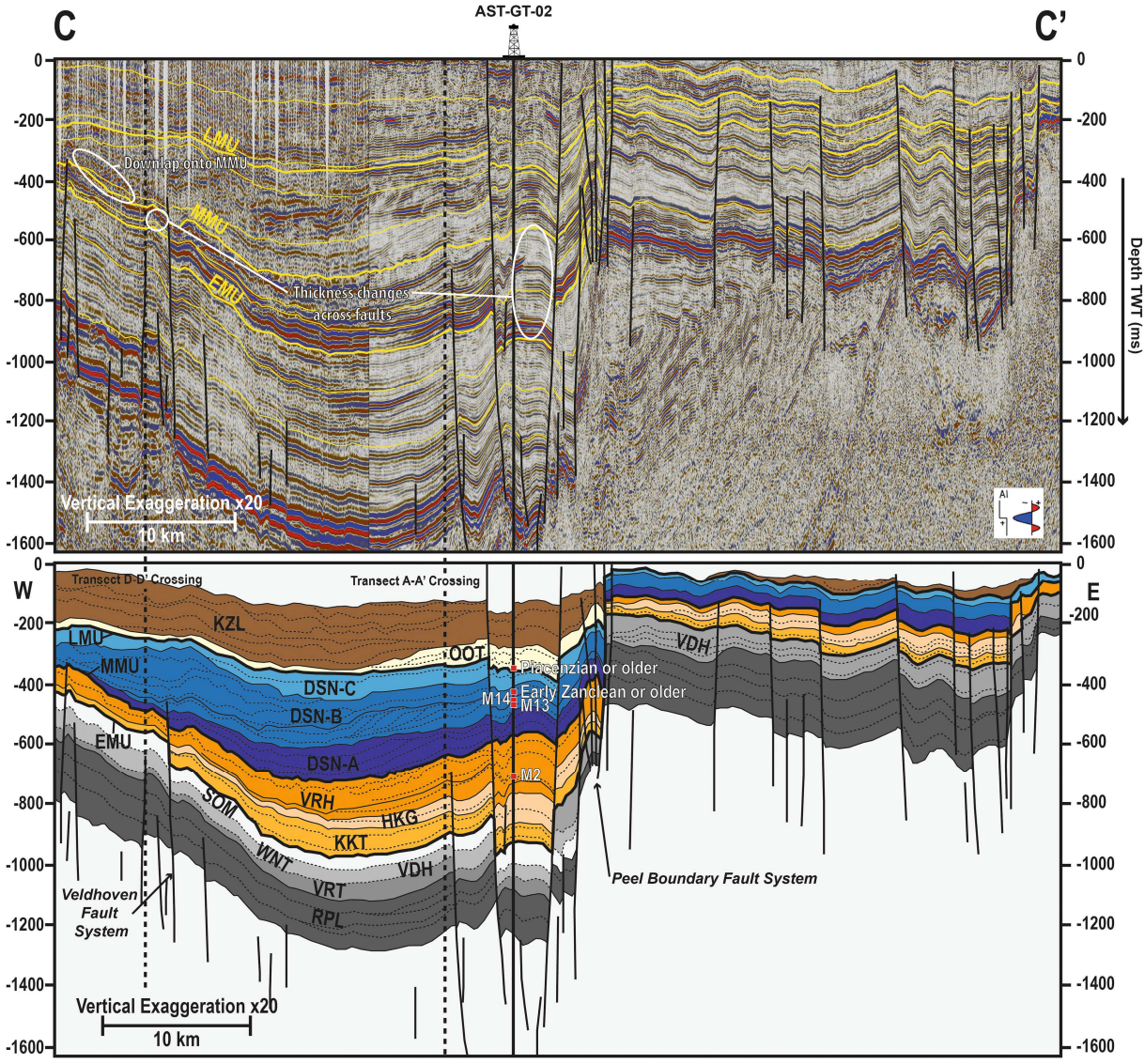

Figure 12 WSW-ENE seismic section perpendicular to the basin axis over the AST-GT-02 well. Source: (Siebels et al., 2024) RPL Rupel Fm, VDH Veldhoven Fm, VRT Voort Mb, WNT Wintelre Mb, SOM Someren Mb (all Veldhoven Fm), KKT Kakert Mb, HKG Heksenberg Mb, VRH Vrijherenberg Mb (all Groote Heide Fm), DSN[A-C] Diessen Fm, OOT Oosterhout Fm and KZL Kieseloolite Fm.

The different lithologies in the VEH-01, KDK-01 and AST-GT-20 wells, in combination with the seismic interpretations of Figure 10 and Figure 12 make it clear that the composition of the Breda Formation in the RVG is laterally varying, and that it is not possible to provide a single lithological succession other than clayey fine sand and sandy clay. Instead, the litholog descriptions of the nearest wells are chosen for the SRIMA calculations.

3.4 Reservoir thickness and depth

The thickness and depth of the Groote Heide and Diessen Formations were taken from unpublished seismic interpretations, described in (Siebels et al., 2024). Maps showing the depth and thickness of those units are in Appendix D. Table 2 shows the extracted values at the three case study locations.

Table 2 Depth and gross thickness of the Groote Heide and Diessen Formations as observed in wells nearby the three case study locations.

		VEH-01	Eindhoven	KDK-01
Diessen	depth top	340	470	320
	thickness	330	510	262
Groote Heide	depth top	670	970	590
	thickness	70	250	190

3.5 Reservoir permeability, porosity

Petrophysical data of the selected aquifers are relatively rare, the reason being that the aquifers were rarely considered an exploration target, and hence acquisition of well log data was limited and often of poor quality due to the borehole condition (either cased, or with large radius and/or washout).

Within the WarmingUP project, petrophysical analyses were carried out for the Breda Formation on deep wells located in the Zuiderzee Low and the northern part of the RVG (Peters et al., 2022; Smit, 2022).

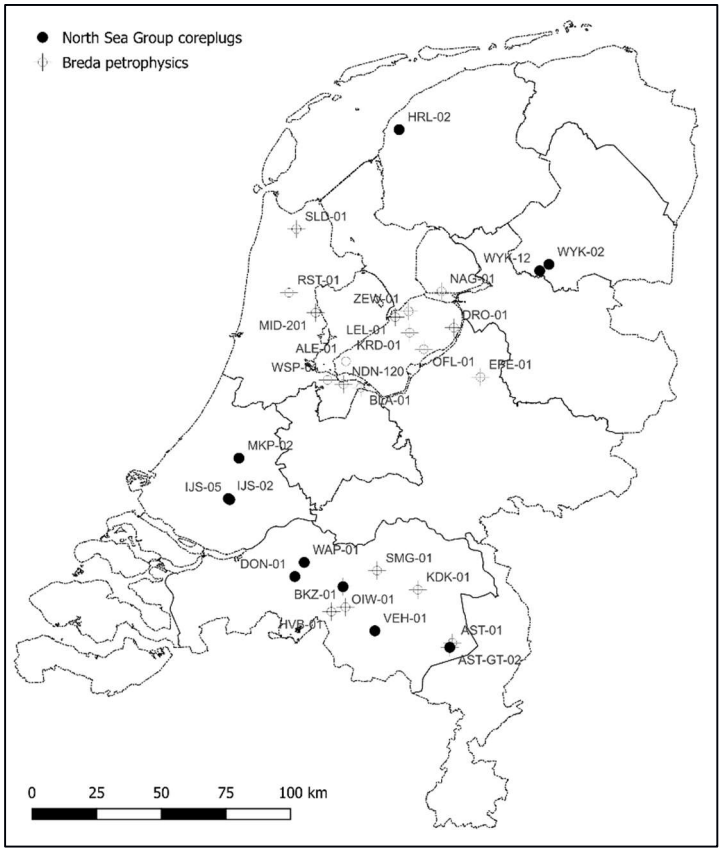

Figure 13 Wells with North Sea Group coreplugs and/or Breda petrophysical analysis.

Table 3 shows an overview of core plug data available from www.NLOG.nl for seven of the identified aquifers. No core plugs are known from the Orp Member. In the absence of core

data for the Breda, core plugs of other aquifer units may be used, but they may stem from units that originated in a different environment and/or underwent different compaction and/or diagenesis. Core plugs of the Brussels Sand, known from the wells DON-01, HRL-02, WAP-01, WYK-02 and WYK-12, are not shown here because the Brussels Sand exists outside the RVG area. By far the most sampled well is AST-GT-02. Further, the wells DON-01, OIW-01 and VEH-01 are located in the direct vicinity of the RVG and are therefore considered most relevant.

Table 3 Overview of wells having core plugs in North Sea Group units (RVG wells in grey, numbers are number of plugs)

Fm / Mbr u	Breda	Someren	Voort	Berg	Steensel	Oosteind	Reusel
Well q	NUBR	NMVESO	NMVEVO	NMRUBE	NMRUST	NLDOOO	NLLARE
AST-GT-02	4		40	24			46
DON-01					5		
F02-03	3						
IJS-02						2	
IJS-05						5	
MKP-02			2	5			
OIW-01			6				
VEH-01		6					
Count	7	6	48	29	5	7	46

Table 4 Overview average core plug porosities in North Sea Group units

Fm / Mbr u	Breda	Someren	Voort	Berg	Steensel	Oosteind	Reusel
Well q	NUBR	NMVESO	NMVEVO	NMRUBE	NMRUST	NLDOOO	NLLARE
AST-GT-02	39		32.0	35.2			27.2
DON-01					27.2		
IJS-02						34.5	
IJS-05						29.4	
MKP-02			30.5	30.6			
OIW-01			27.0				
VEH-01		31.2					
Average	39	31.2	31.3	34.4	27.2	30.9	27.2

Table 5 Overview average core plug permeabilities in North Sea Group units

Fm / Mbr u	Breda	Someren	Voort	Berg	Steensel	Oosteind	Reusel
Well q	NUBR	NMVESO	NMVEVO	NMRUBE	NMRUST	NLDOOO	NLLARE
AST-GT-02	560		17	1222			254
DON-01					432		
IJS-05						351	
MKP-02			116	309			
OIW-01			278				
VEH-01		90					
Average	560	90	53	1092	432	351	254

Table 3 shows that the available core plug data for the Breda Formation is limited which makes calibration of the petrophysical evaluations challenging. The aquifer property data shown in Table 9 that were used as input for the SRIMA calculations are therefore based on (Peters et al., 2022). The aquifer depths and thicknesses are based on seismic interpretation by (Siebels et al., 2024). The temperatures are based on (Veldkamp & Hegen, 2020) and (Peters et al., 2022)

3.6 Fluid properties

To derive reliable fluid properties to simulate the behaviour of the aquifers within the shallow formations of the RVG, well AST-GT-02 was utilised to determine the total dissolve solids (TDS) (Heederik et al., 1989). For the Berg Sand, at a depth of 1510 meter, it was 51475 mg/l, and for the deeper Houthem Formation at 1673m, 47100 mg/l. Figure 14, based on the AST-GT-02 data in combination with data from the Oost-Brabant Waterleidingmaatschappij and (van Doorn et al., 1985) shows that for the shallower Breda Formation (between ~450 and 700m) the chloride content is significantly lower. Note that in the Berg Sand and the Houthem Formation chloride makes up about 60% of the TDS, so the actual TDS in the Breda Formation is higher than just the chloride content. The low chloride content in the uppermost ~900m is explained by infiltration of fresh water. The higher chloride contents in the Berg and Houthem are explained as a result of the mixing of this fresh water and deeper more saline waters. The transition of fresh to salt water is established at ~320m. Figure 15 suggests that further north of Asten the salinity is higher at comparable depth.

We took empirical values for the fluid density, heat capacity and viscosity for the injection temperature and for the reservoir temperature for a default salinity of 2000 mg/l ((Batzle & Wang, 1992).

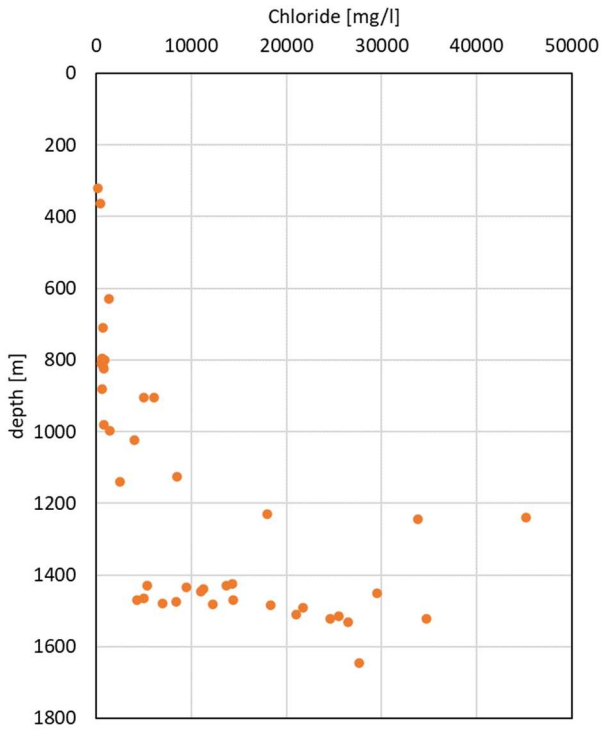

Figure 14 Chloride content of the formation water in the Asten-GT-02 well. Source: after (Heederik et al., 1989) table 3.1.

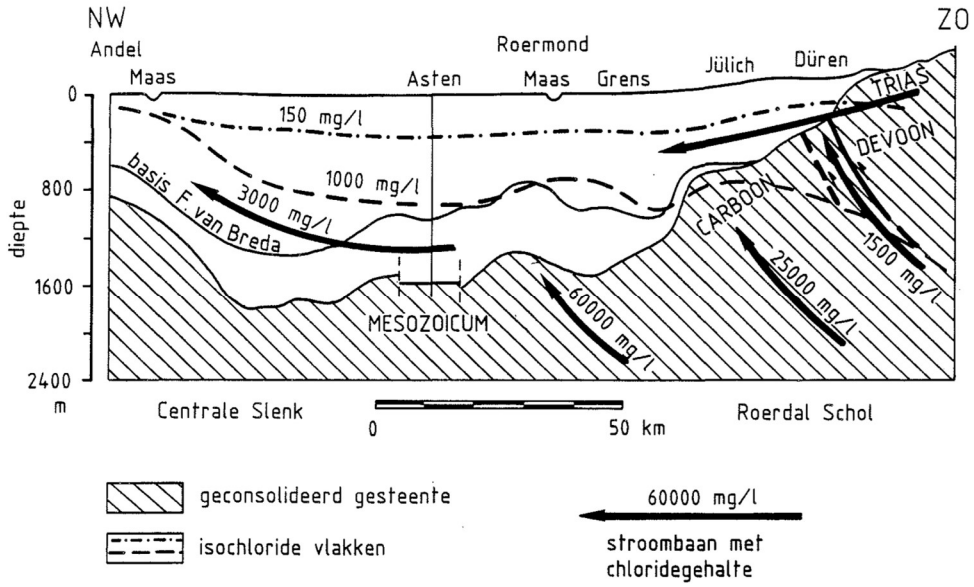

Figure 15 Hydro-geological profile over the Asten well. Source: (Heederik et al., 1989)

3.7 Poro- and thermo-elastic properties

SRIMA and many other model tools assume an isotropic homogeneous elastic medium, which can be described by any pair of static elastic moduli. These moduli may be derived from sonic and density measurements as part of wells logs, yielding *dynamic* elastic moduli. The dynamic moduli are typically an overprediction of their static equivalents and therefore have to be corrected.

Ideally, the sonic measurements consist of a Vp (compressional wave) and Vs (shear wave) measurement (or their reciprocal slownesses). Poisson's ratio and Young's modulus are then obtained as:

$$\nu = 0.5 \frac{\left(\left(\frac{V_p}{V_s}\right)^2 - 2\right)}{\left(\left(\frac{V_p}{V_s}\right)^2 - 1\right)}. \quad 1$$

and

$$E = 2\,\rho V_s^2(1 + \nu). \quad 2$$

Correction methods for dynamic to static moduli consist of empirical formulations, that are strictly only valid for the data set and experimental conditions from which they are derived. An overview of these empirical formulations is found in the textbook by Mavko et al. (2020), section 2.14. From these, we test the Young's modulus corrections by Wang & Nur(2000) for soft rocks, Mese & Dvorkin (2000) for shales and shaly sands, and Gorjainov & Ljachowikij (1979) for sandy, wet soil. In addition, we use the Mese & Dvorkin (2000) correction for the Poisson's ratio.

Note here that we are not sure what type of rock to expect in the North Sea Group formations in the RVG: Is it closer to an unconsolidated sediment, or closer to a soft sandstone? This impacts Young's modulus in particular, which may range over 3 orders of magnitude: Between

a few 10's of MPa's for typical sand to at most 10 GPa for a soft sandstone. The correction methods proposed above therefore include corrections for soft rocks and soils.
The well logs near the region of interest (Veldhoven (VEH), Keldonk (KDK), Asten (AST), Hilvarenbeek (HVB), and Broekzijde (BKZ)) either have a single sonic measurement or none. We therefore first obtain the elastic moduli for the Breda Fm from sonic logs from outside the RVG, from the Oranjeoord (ORO) well (Figure 16). Here, the Breda formation is located shallower (at 221 m depth) and is thinner (66 m thick) than in the RVG. Since elastic moduli typically increase with depth, these values may be considered a lower bound.

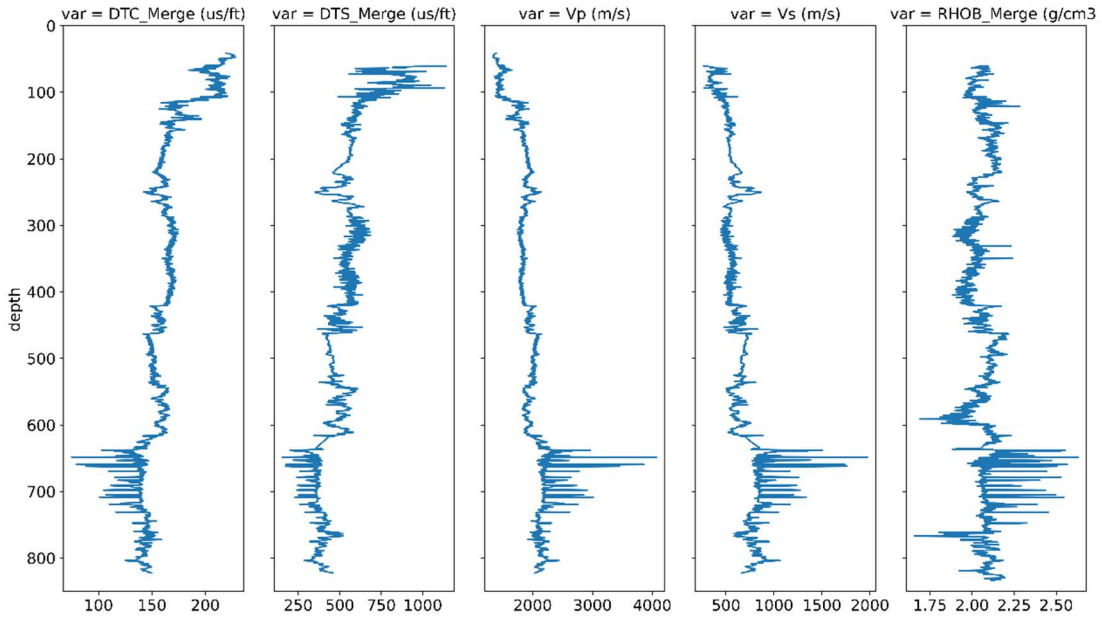

Figure 16: Sonic and density data from the ORO well. DTC = Compressional slowness, DTS = Shear slowness, RHOB = density.

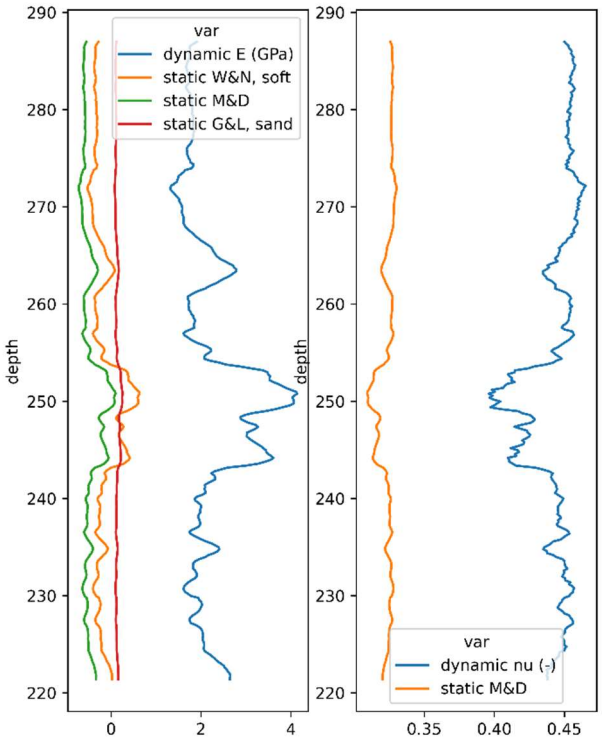

Figure 17: Dynamic (blue curves) and static Young's moduli (left) and Poisson's ratio (right) in the Breda formation at the ORO well. Note that the static corrections (green and orange curves) that yield negative Young's moduli are unphysical and thus incorrect (see main text). Static moduli are obtained from the empirical corrections proposed by W&N = Wang & Nur (2000); M&D = Mese & Dvorkin (2000), G&L = Gorjainov & Ljachowickij (1979).

The dynamic Young's modulus in the Breda Fm varies between 2 GPa and 4 GPa, the dynamic Poisson's modulus varies between 0.4 and 0.45 (Figure 17, blue curves). The static correction for Poisson's ratio yields a value of 0.31 to 0.32. However, the corrections for static Young's moduli using the W&N and M&D relations (Figure 17 left panel, green and orange curves) yield incorrect negative values – showcasing that indeed empirical relations must be applied carefully. The correction by G&L (Figure 17 left panel, red curve) assumes an unconsolidated sandy sediment, and yields low but realistic (for a loose sand) Young's moduli values between 83 and 255 MPa. From this, we can set a preliminary range for Young's moduli of, roughly, 0.1 GPa to 4 GPa, and for Poisson's ratio of 0.3 to 0.45.

The coefficient of thermal expansion has not been measured for the North Sea group sediments in the RVG itself or at other localities. We therefore shall propose a range of values based on literature. For several Dutch consolidated reservoir sandstones the *volumetric* coefficient of thermal expansion varies between $3 \times 10^{-5}\ K^{-1}$ and $10 \times 10^{-5}\ K^{-1}$ ((Soustelle et al., 2022)). Of these reservoir sandstones, the ones with the highest porosities (28% porosity) may be most representative for the North Sea Group formations. Their coefficient of thermal expansion at the target temperatures between 30 C and 45 C ranges between $6 \times 10^{-5}\ K^{-1}$ and $7 \times 10^{-5}\ K^{-1}$. The linear thermal expansion coefficient is 1/3 of that value, resulting in $2 \times 10^{-5}\ K^{-1}$.

Biot's coefficient is also not measured on North Sea group sediments. For reservoir sandstones, such as Slochteren sandstone, Biot's coefficient varies between 0.5 and 0.9 (Filippidou 2019), where a higher porosity of >22% yields a Biot's coefficient of 0.9. Biot's coefficient is one minus the ratio of the bulk moduli of the porous medium framework and the solid constituents. For less consolidated sandy materials, the porous medium framework bulk modulus would be lower than that of consolidated sandstone, and therefore would likely yield even higher Biot's coefficient values approaching 1. We therefore explore a range of Biot's coefficient values between 0.5 and 1.

3.8 Thermal properties

The specific heat capacity can be assessed as a weighted average of the constituents. The weighted average C is formulated in terms of the heat capacities of the grains constituting the matrix and the water in the pores, C_s and C_w, their densities ρ_s and ρ_w, and the porosity ϕ as

$$C = \frac{(1-\phi)\rho_s C_s + \phi\rho_w C_w}{(1-\phi)\rho_s + \phi\rho_w} \quad 3$$

Typical values for sandstones range between 800 and 1000 J/kg.K (Vivas et al., 2023). We have used a value of 800 J/kg.K.

The bulk thermal conductivity can be assessed as a weighted average of the constituents. The weighted average λ is formulated in terms of the thermal conductivities of the grains constituting the matrix and the water in the pores, λ_s and λ_w, and the porosity ϕ as follows (geometric mean model of (Somerton, 1992)):

$$\lambda = \lambda_s^{(1-\phi)}\lambda_w^{\phi} \quad 4$$

Typical bulk thermal conductivity values for sandstones at depths around 500 meter (29% porosity) range between 1.5 and 2.2 W/m.K (Hantschel & Kauerauf, 2009). Similar values are obtained for the 3D temperature model of the Netherlands (Békési et al., 2020; Bonté et al., 2012). We have used values of 1.9, 1.6 and 1.5 W/m.K for the Veldhoven, Eindhoven and Keldonk locations.

3.9 Fault geometry

Figure 19 and Figure 20 show the orientation (azimuth and dip) of those parts of the faults that cut through the Breda Formation. Most fault segments have azimuths around 45° (NE) and 225° (SW) (Figure 20). Most faults have dips smaller than 60°.

An important exception to the general fault directions is the Veldhoven Fault System (Figure 1). This system exists 3.5 km south of the Veldhoven location. It includes the Feldbiss fault, which has an average azimuth of 27-29° and a dip of 53°. Minor faults having the same azimuth and dip as the Feldbiss may be present at the Veldhoven location.

A second, smaller exception is a fault near Liessel in the eastern part of the RVG area (yellow in Figure 19), which is striking more N-S rather than NW-SE and has a dip exceeding 70°.

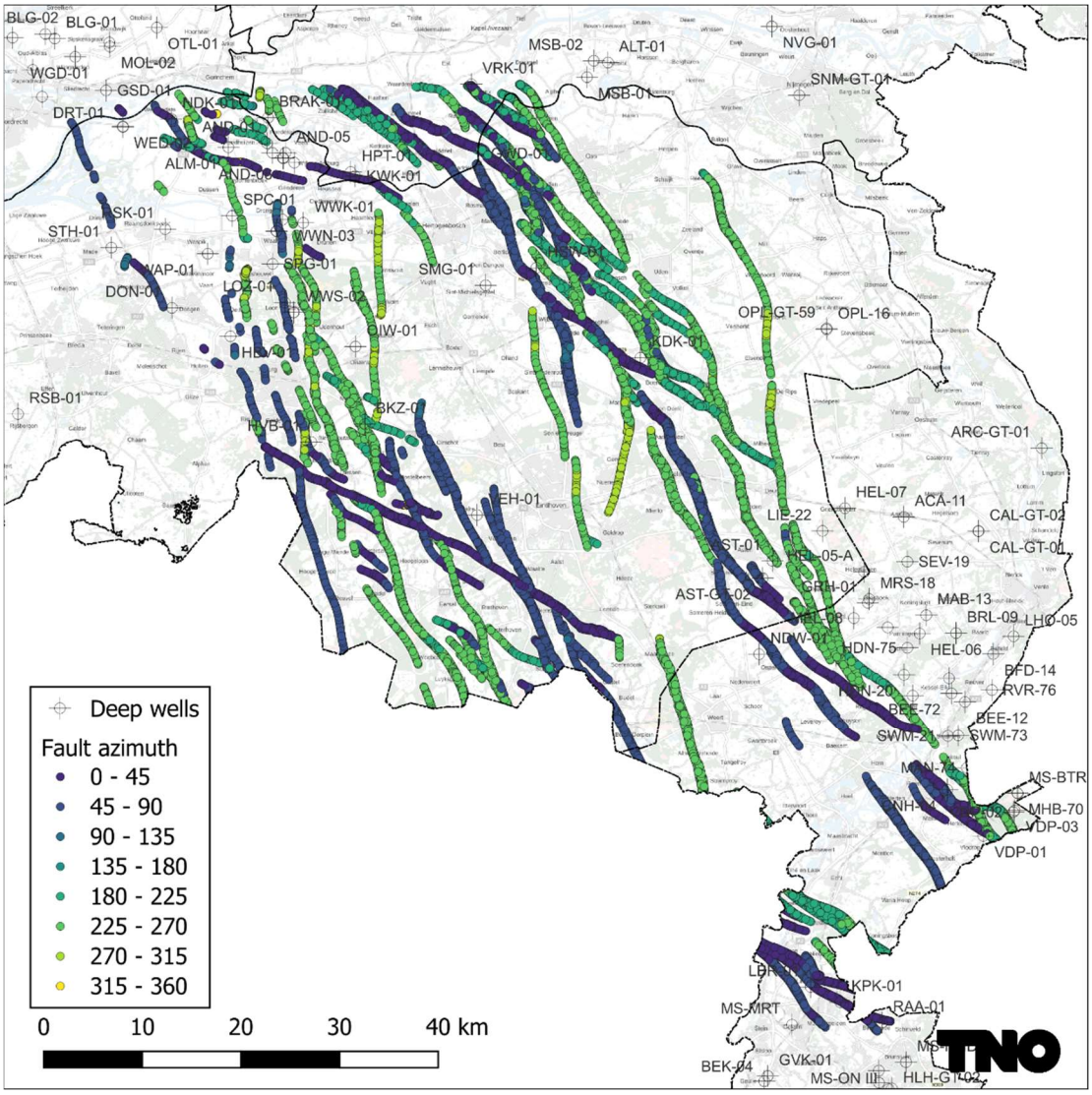

Figure 18 Azimuth of the Breda parts of faults mapped in the RVG (source: TNO H3O Diep).

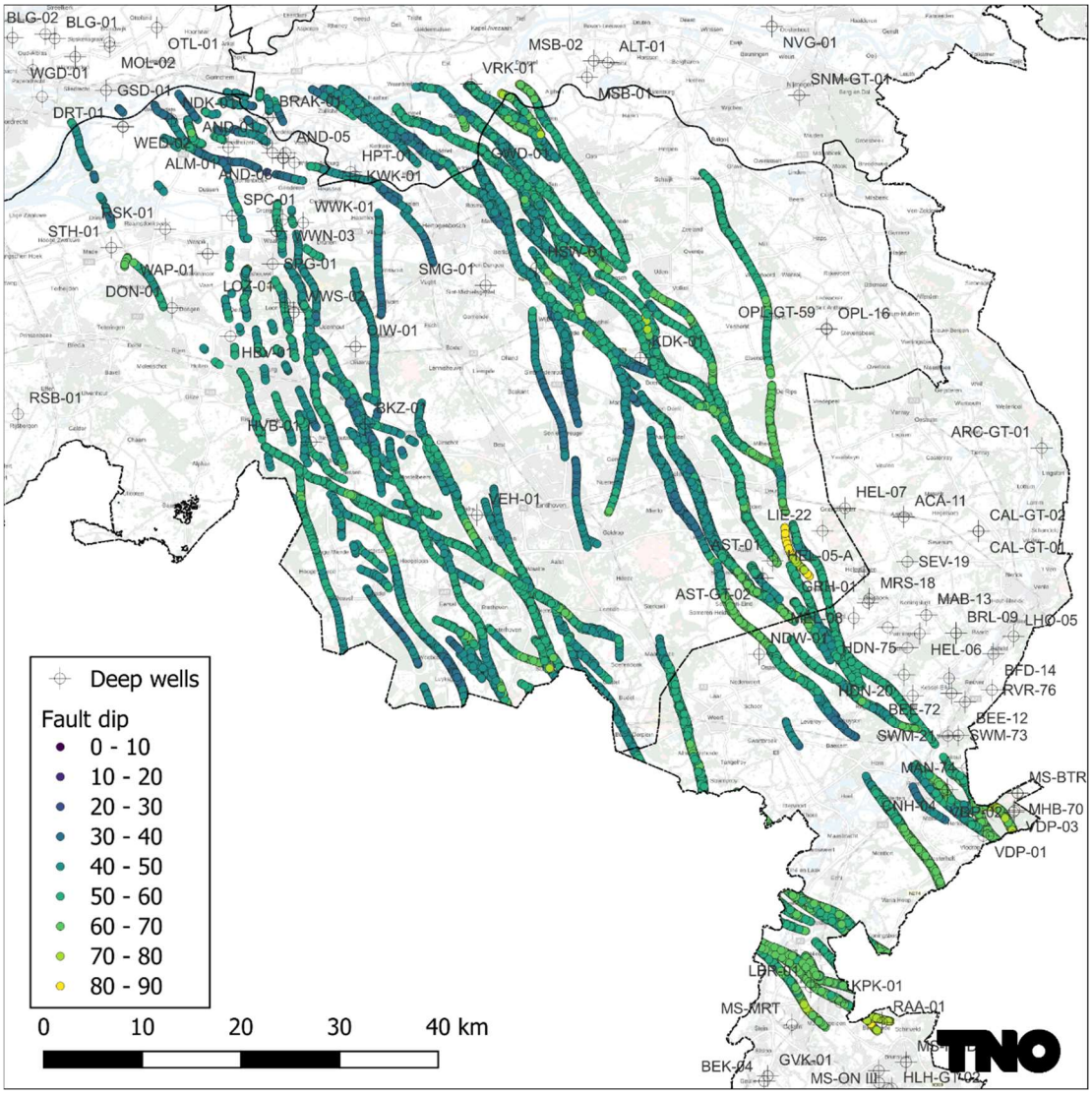

Figure 19 Dip of the Breda parts of faults mapped in the RVG (source: H3O Diep)

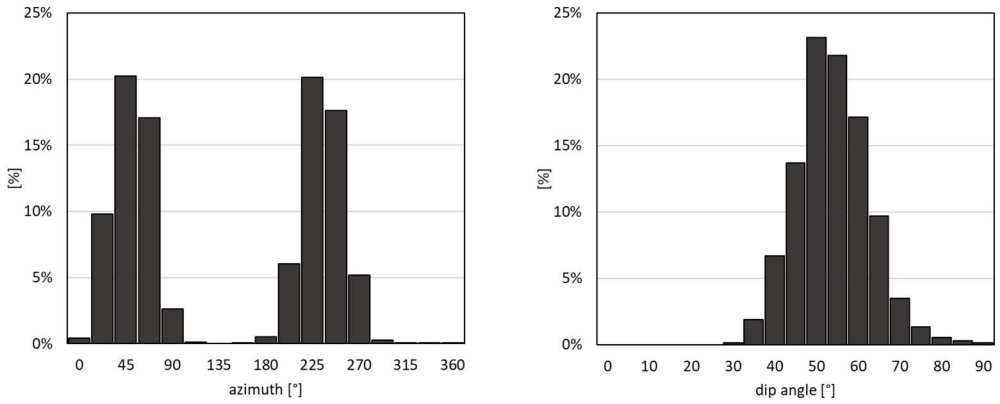

Figure 20 Azimuth and dip of the Breda parts of faults mapped in the RVG (source: H3O Diep).

Table 6 Average azimuth and dip of faults cutting the Breda Formation in a radius of 2.5km around the target location. Numbers in italic indicate that no faults were mapped at a distance <2.5km, and a 5km radius was used instead.

location	direction	azimuth	dip
Veldhoven	NE	52	44
	SW	*232*	*52*
Eindhoven	NE	*63*	*44*
	SW	*235*	*44*
Keldonk	NE	65	46
	SW	232	49

3.10 Fault friction coefficient

Fault gouge from faults cross-cutting the North Sea Supergroup formations has not been recovered from laboratory friction tests, nor from drilling through faults. We therefore have to use values from literature. We focus here on the static friction coefficient on the fault which, in the absence of cohesion, is equal to the shear- to normal stress ratio the fault will start to slide. In the discussion we further evaluate the use of the static friction coefficient in the geomechanical modelling tools, and how slip- or rate-dependent friction can impact fault stability and seismogenesis. The literature research focusses on frictional behaviour of (gouges derived from) partially consolidated sediments.

The static friction coefficient μ of unconsolidated sediments seems to vary with clay content: For high clay content, $\mu = 0.4$ and for low clay content in more sandy lithologies, $\mu = 0.65$ (Balsamo et al., 2014; Seyler et al., 2020). The experimentally applied effective pressure, a proxy for depth of the sediments, does not make a noticeable impact on the static coefficient of friction for the range of applied effective pressures.

3.11 Density, vertical stress, horizontal stress and pressure

The initial stress acting on a fault directly affects fault stability and the potential for fault reactivation. In order to assess the initial stability of faults and fractures, the full effective stress tensor is needed – i.e. the magnitudes of the principal stresses, as well as their orientations, and the pore pressure. In the earth, usually one of the three principal stresses is oriented vertically, except in e.g. the vicinity of salt domes or large topographical variations. Most measurements in the Netherlands indicated a normal faulting regime where the vertical stress is the largest ($\sigma_v > \sigma_H > \sigma_h$). In the following sections we focus on the stress available stress measurements in the North Sea Groups in the Netherlands.

3.11.1 Bulk density and vertical stress

The vertical stress can be computed from the formation bulk density ρ_b, which is the weighed density of the rock matrix and pore fluid

$$\rho_b = (1 - \phi)\rho_{ma} + \phi\rho_f \qquad 5$$

where ϕ is the porosity. The vertical stress can be computed by integrating the bulk density with depth,

$$\sigma_v(z) = \rho_{sw} g z_{sw} + \int_0^z \rho_b(z) g dz \qquad 6$$

where ρ_{sw} is the seawater density, z_{sw} is the seawater depth, and z is the depth from the seafloor or land surface. In the onshore region of RVG the seawater term can be ignored.

Bulk density is logged with a density logging tool along the wall of wellbores. Density logging is done in many, but not all wells in the Netherlands. Within the RVG there are several wells which contain a density log in the North Sea Groups (Figure 21). Note that the outlines of the RVG shown in Figure 21 are based on the Mesozoic structural elements defined in (Kombrink et al., 2012). Within this framework, the northwestern boundary of the RVG with the West Netherlands Basin was defined by the pinching out of the Chalk sediments. However, the Cenozoic sediments are deposited more continuously across this boundary. Hence, we consider also some of the wells on the western side of the West Netherlands Basin, such as the Barendrecht (BRT) wells. In addition, we consider the recent Oranjeoord well (ORO-01) drilled in the SCAN project, which is located on the Oosterhout Platform (OP). In total, 34 wells were taken to estimate the density distribution and the vertical stress gradient, 17 of which contained >200 m of bulk density log in the North Sea Groups.

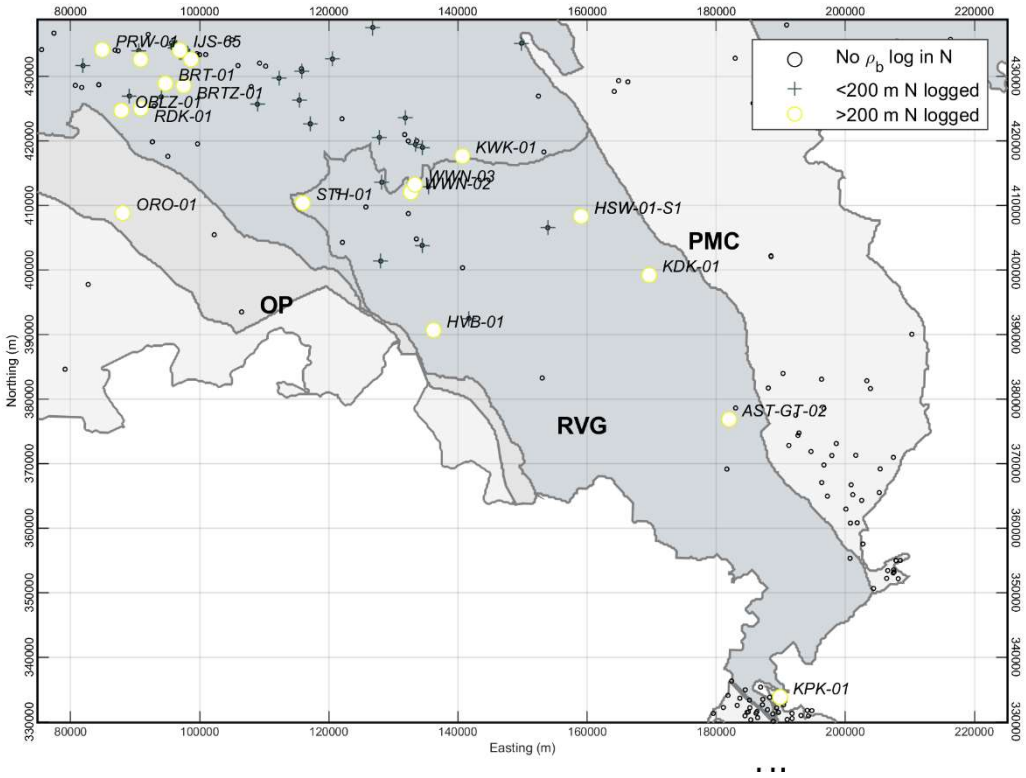

Figure 21 Map view of wells in and near the RVG. Yellow symbols indicate wells where >200 m of North Sea Group sediments were logged with the density logger, the plus symbol indicates wells where a density log was available in the North Sea Group sediments but over <200 m of well length. Small circles indicate other wells. RVG: Roer Valley Graben, PMC: Peel-Maasbommel Complex, OP: Oosterhout Platform.

The bulk density logs were manually QC-ed along the following steps:

- bad data sections due to recording errors were removed.
- sections with high (>0.1 gcm^{-3}) absolute density correction were removed.
- sections with large washouts identified on the caliper logs and corresponding suspiciously low-density measurements were removed. Washouts can be a major problem for logs in the unconsolidated North Sea Group sections. In case of significant

wellbore enlargement, the tool may mainly measure within the borehole mud, which gives an underestimate of the density. However, in some cases the hole may be enlarged somewhat but the rugosity may be low, and the tool can still measure the correct density. Hence, the caliper is considered jointly with the density log.

- in absence of a caliper log, sections with density <1.9 cm^{-3} were removed.

An example of a QC-ed log is shown in Figure 22. The caliper log shows how in particular in the shallowest parts of the well, but also between 580 – 605 m along hole depth, the hole is significantly enlarged. The resulting recorded bulk density is (too) low and has been removed from the bulk density dataset. Not excluding this data would have led to an underestimate of bulk density of the Upper North Sea Group.

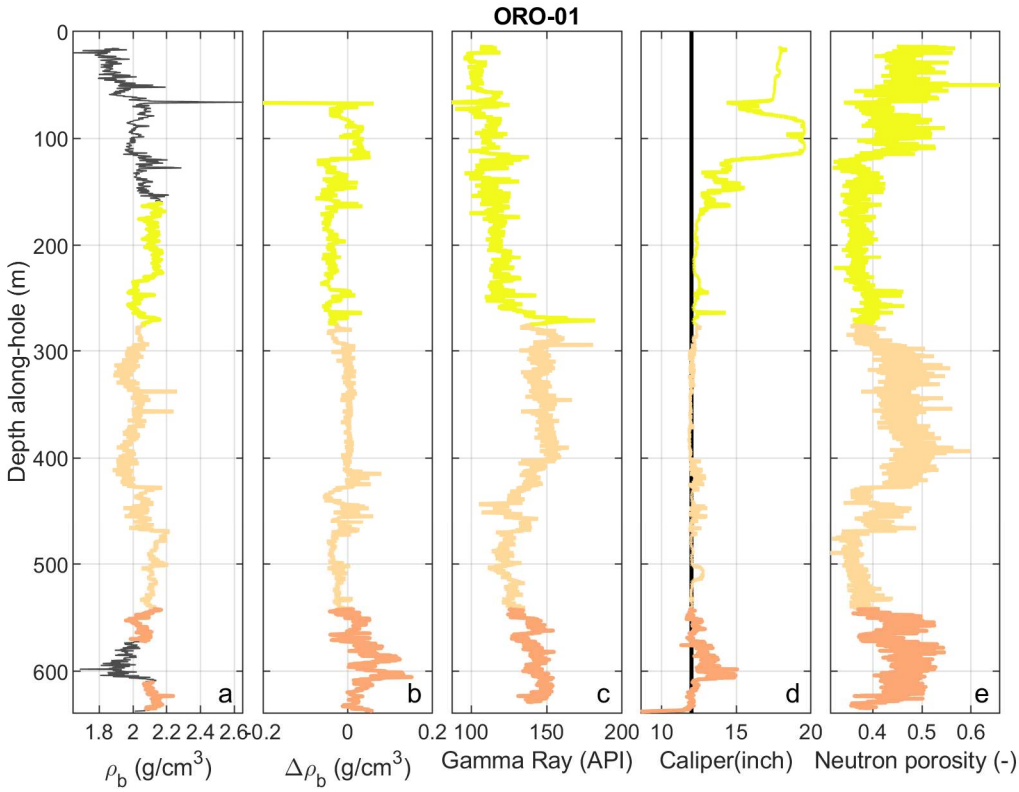

Figure 22 Example of well logs and quality control of the density log. Data of Oranjeoord 01 (ORO-01) is shown. Curves are color-coded according to litho-stratigraphic unit, with yellow: Upper North Sea Group, light orange: Middle North Sea Group, and dark orange: Lower North Sea Group. The black curve in a is the raw bulk density log and hence shows where the log has been rejected or corrected. The black curve in d) is the bit size used to drill the well.

Most density logs are not complete over the well length. Often, the shallowest section is missing, or only selected intervals were logged. In addition, the QC procedure removes bad quality sections. To compute the vertical stress, a certain density value must be assumed over these intervals. Alternatively, the average density trends with depth can be used to compute the vertical stresses at a certain location.

In Figure 23 the combined logged bulk densities of all the selected wells in the RVG study area are plotted against depth, distinguishing between the three North Sea Groups. The bulk densities of the Upper North Sea Group are nearly constant with depth, with an average value of ~2.0 gcm^{-3} (Figure 23a). The Middle North Sea Group (Figure 23b) shows some increase of bulk density with depth, and the Lower North Sea Group (Figure 23c) exhibits and even large depth dependency. Given the thickness of each of the three North Sea Groups at a certain

location, a profile of the density with depth and the corresponding vertical stress profile can be constructed using the linear fits shown in Figure 23.

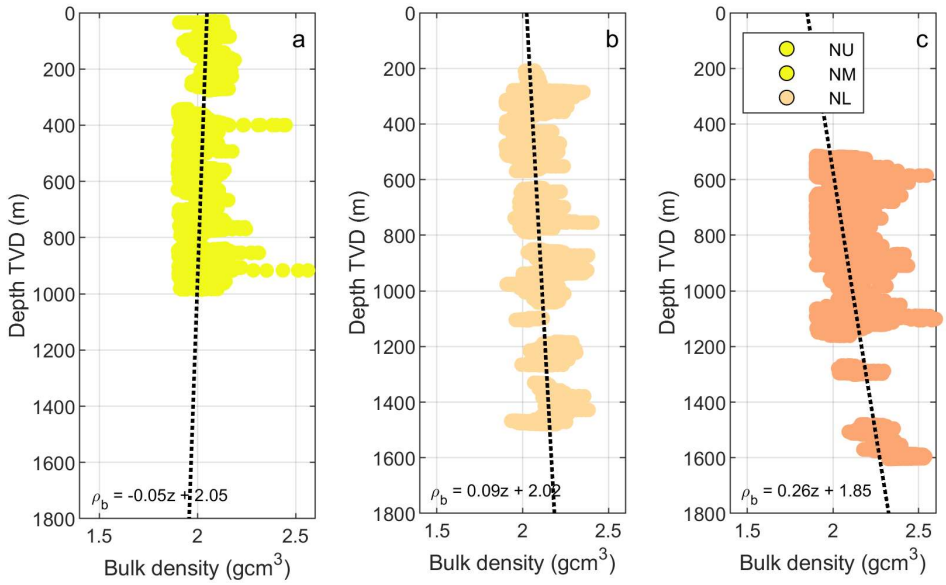

Figure 23 Bulk density (QC-ed) for the three different North Sea Groups

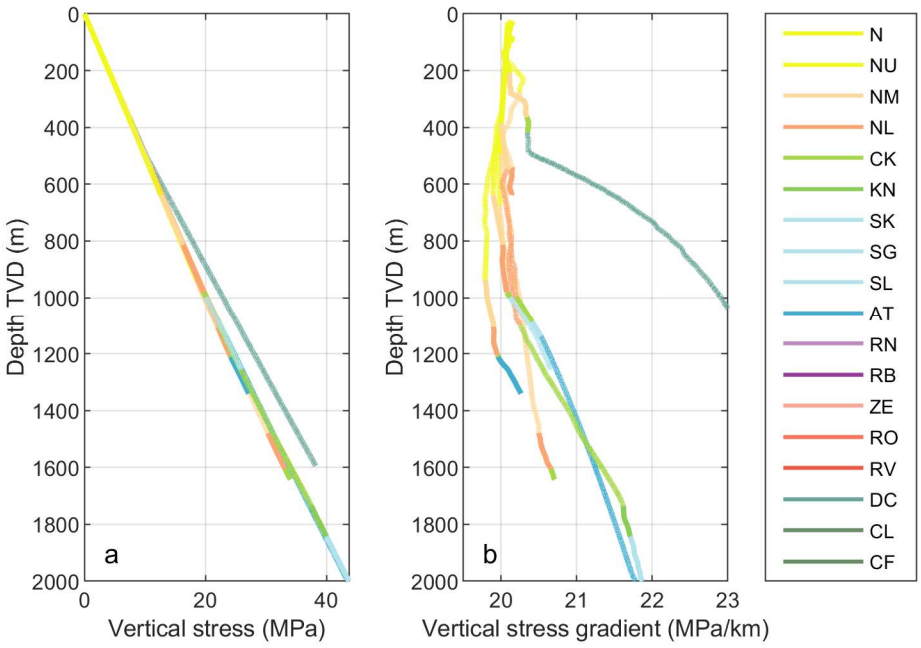

Figure 24 Vertical stresses and stress gradients for selected wells in the RVG. Wells with at least a 50% density log coverage in the North Sea Groups are shown. Missing sections have been filled with average densities (see Figure 23) for the litho-stratigraphic group and depth in question. a) vertical stress with depth. b) 'apparent' vertical stress gradients with depth – i.e. the vertical stress divided by the depth, in MPa/km.

The resulting vertical stress gradients in the North Sea Groups are approximately 20 MPa/km up to a depth of 1000 m (Figure 24). One exception is the KPK-01 well, which is located in the southeasternmost part of the RVG, on the border with the Limburg High (Figure 21). Here, only 380 m of North Sea Group are present, directly overlying carbonates of the Limburg Group (DC). These carbonates have a high densities (2.7 gcm^{-3}) which results in high vertical stress

gradients of 23 MPa/km at 1000 m depth. The higher density of other litho-stratigraphic groups of e.g. the Cretaceous and Jurassic (KN, SL, AT) also results in a clear increase in stress gradients at the base of the North Sea Groups.

3.11.2 Horizontal stresses

There are two horizontal stresses, the maximum and the minimum horizontal stress. Measuring the minimum horizontal stress is easier than measuring the maximum horizontal stress. Here, we first summarize the data inventory on the minimum horizontal stress.
Information about the minimum horizontal stress σ_h was derived from various well measurements. Most of these are formation integrity tests (FIT) or leak-off tests (LOT). These tests are done routinely during drilling. When a certain well section has been drilled, cased and cemented, a small hole (rathole) of a few m long is drilled into the formation below the casing shoe. The entire wellbore and the rathole is pressurized, to measure the formation strength (~horizontal stress) in the rathole, as a means to set the mudweight for drilling the next section. The following tests are distinguished:

- Formation Integrity Test (FIT), also called Formation Strength Test, or Limit Test. During this test pressure is increased to a certain level (e.g. 1.5 specific gravity) to test whether the formation holds this pressure. If so, the pressure is reduced again and drilling proceeds. During the FIT, no fracture is created, and it can only be used as a lower bound to the minimum horizontal stress.

- Leak-off Test. During the leak-off test (LOT) pressure is increased stepwise with a waiting period after each step (Figure 25). This is done until the pressure-volume curve starts to become non-linear and or the amount of leak-off over the waiting period starts to increase. The deflection point, also called the leak-off pressure (LOP), is seen as indicative for small fractures opening in the wellbore wall. Fractures will likely open against the minimum horizontal stress, and hence the LOP is often equated with the σ_h. However, the LOP is affected by the formation tensile strength and the orientation of the wellbore. Hence, LOP tends to overestimate σ_h.

It is important to note that the casing shoe is often set in a strong formation - i.e. a formation with a high strength and/or σ_h. These are usually shales, clays, chalk and evaporites. Taking LOP's may thus bias the estimate of horizontal stress towards that in strong formations.

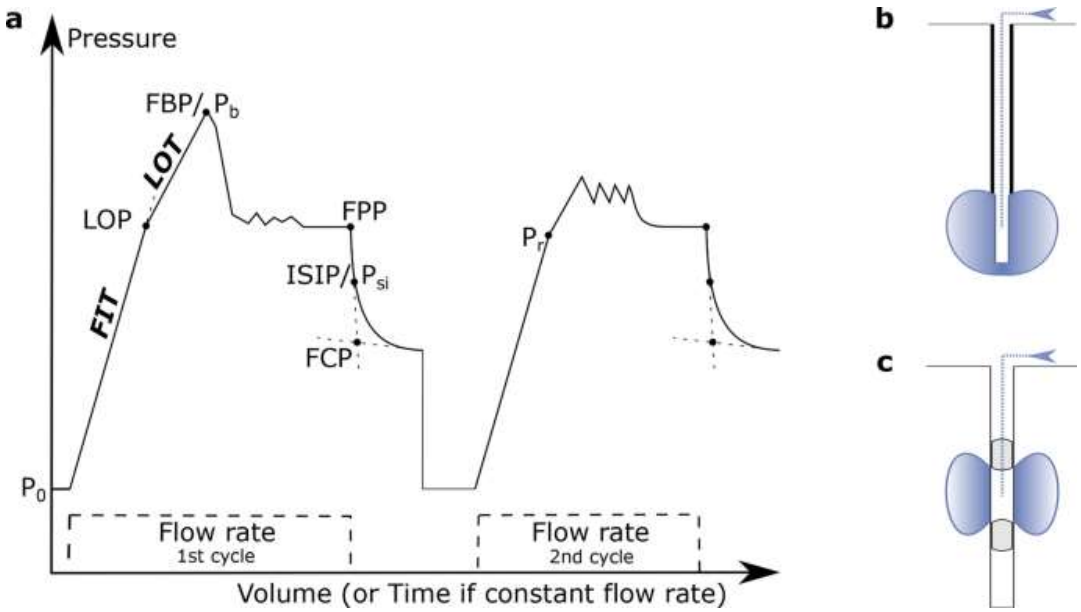

Figure 25 a) Schematic illustration of pressure measured during different wellbore tests. FIT: Formation Integrity Test, LOT: leak-off test. Evolution of the pressure volume curve beyond the LOT is typical for an extended leak-off test (XLOT) or mini-frac. From: Morawietz et al. (2020). B) Schematic illustration of typical execution of FIT and LOT the at the casing shoe. C) example packers isolating a specific section of the wellbore for a mini-frac test.

Estimates of the minimum horizontal stress can be improved by performing and extended leak-off test (XLOT) instead of a normal leak-off test. Here, pressure on the rathole or a certain isolated section of formation is increased beyond the LOP, until formation breakdown occurs (breakdown pressure FBP), indicating that a fracture has indeed formed. Pumping is continued and the fracture is propagated further from the wellbore. When pumping is stopped, closure of the fracture will result in a characteristic fall-off curve. From this curve, the fracture closure pressure (FCP) can be derived. This is seen as the most reliable indicator for σ_h. Oftentimes, multiple pressurization cycles are done to get a stable σ_h. The procedure for a mini-frac test is very similar, with the difference that a mini-frac is often performed in the reservoir as a preparation for a hydraulic fracture.

Figure 26 shows the location of FIT, LOT and XLOT measurements in the North Sea Groups in and close to the RVG. Most of the LOT were performed in wells within the West Netherlands Basin near Pernis, Barendrecht and Waalwijk. Only one XLOT measurement within the North Sea Groups was taken close to the RVG; the XLOTs in the recently drilled SCAN well Oranjeoord (ORO-01).

The reported leak-off pressures were mostly in the range 14 – 16 MPa/km (Figure 27). There is substantial scatter in the data, and limit pressures, which should in theory be a lower bound to σ_h are in the same range as the leak-off pressures.

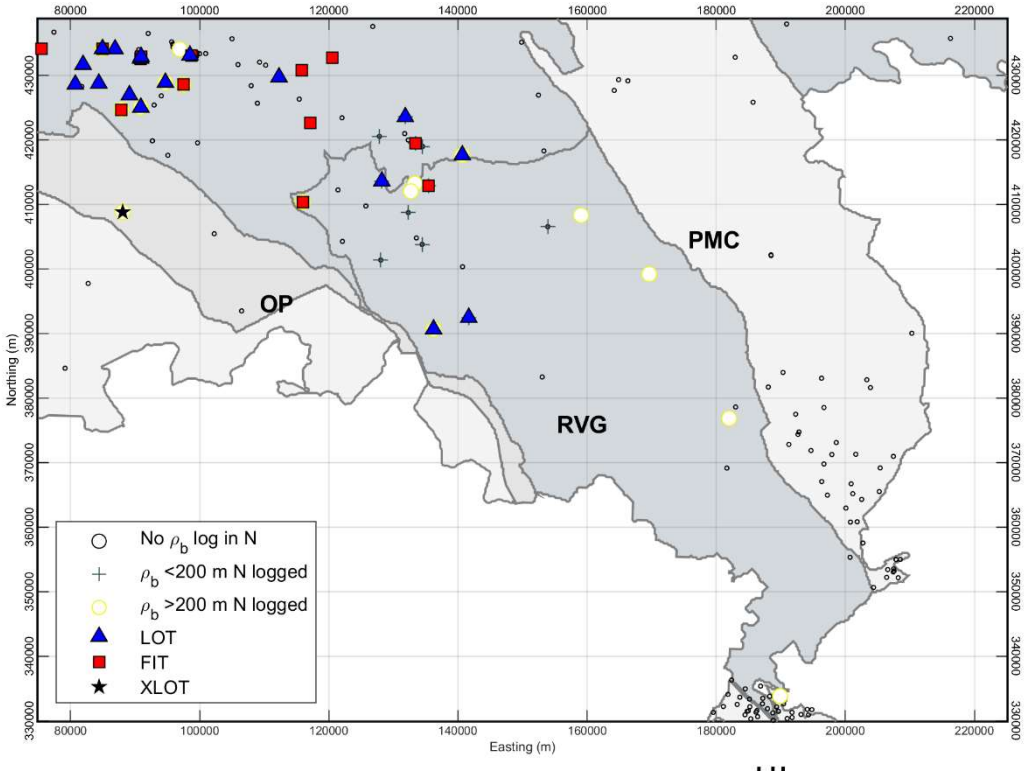

Figure 26 Location of FIT, LOT, and XLOT measurements in the North Sea Groups, superimposed on the bulk density locations of Figure 21. Mesozoic structural elements (e.g. Kombrink et al., 2012) are plotted in the grey background. Coordinates in Rijksdriehoek New (RD New).

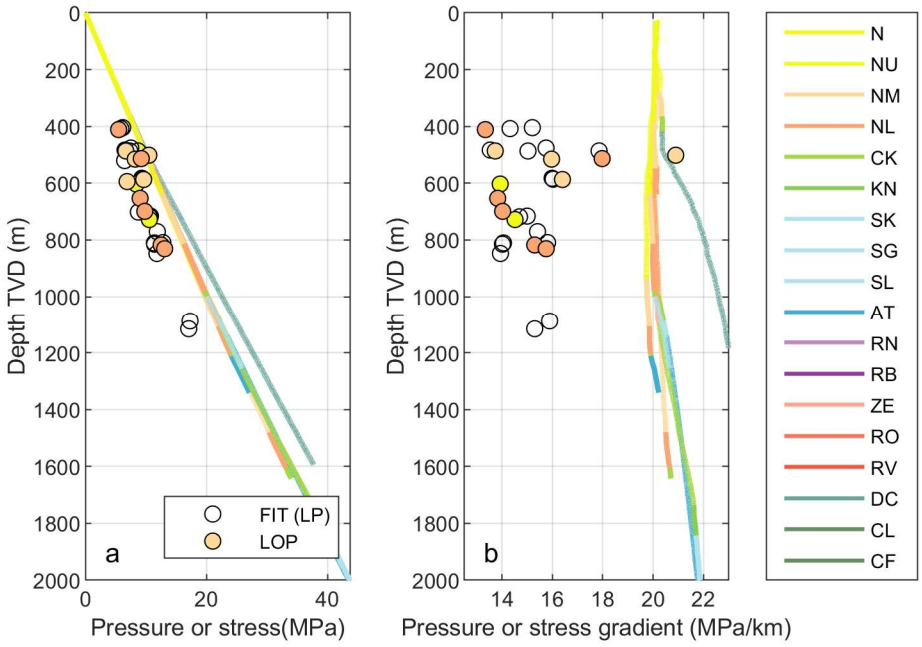

Figure 27 Leak-off pressures (LOP) and limit pressures (LP) obtained during FITs and LOTs in the North Sea Groups, in the RVG. See Figure 26 for location of measurements. Pressures and stresses are shown as absolute values (a), and as pressure gradients (b). For reference, the vertical stresses of Figure 24 are also plotted.

Two extended leak-off tests (XLOTs) were performed in the SCAN exploration well Oranjeoord (ORO-01); in the Boom Member (Rupel Formation, Middle North Sea Group) at 343 m depth (True Vertical Depth), and in the Asse Member (Dongen Formation, Lower North Sea Group) at 580 m depth (data at www.nlog.nl). Both tests were done through perforations in the casing. The XLOT in the Boom consisted of 5 cycles (Figure 28). Instantaneous shut-in pressures (ISIP, see also Figure 25) in the range of 5.9 – 6.2 MPa were recorded by the downhole pressure gauge. The leak-off curves were not yet fitted to obtain the Fracture Closure Pressures, which is a better estimate of the minimum horizontal stress; it is recommended to do so in a follow-up study. Based on the ISIP, the minimum horizontal stress gradient in the Boom is 17.4 – 18.0 MPa/km. Combined with a vertical stress gradient of 20 MPa, this gives a high K_0 (= σ_h/σ_v) ratio of 0.87 – 0.9. These values are in similar to values measured XLOTS performed in the Boom Member at greater depth in the Amstelland well (AMS-01, in North Holland) at greater depth, which were ~18.7 MPa/km.

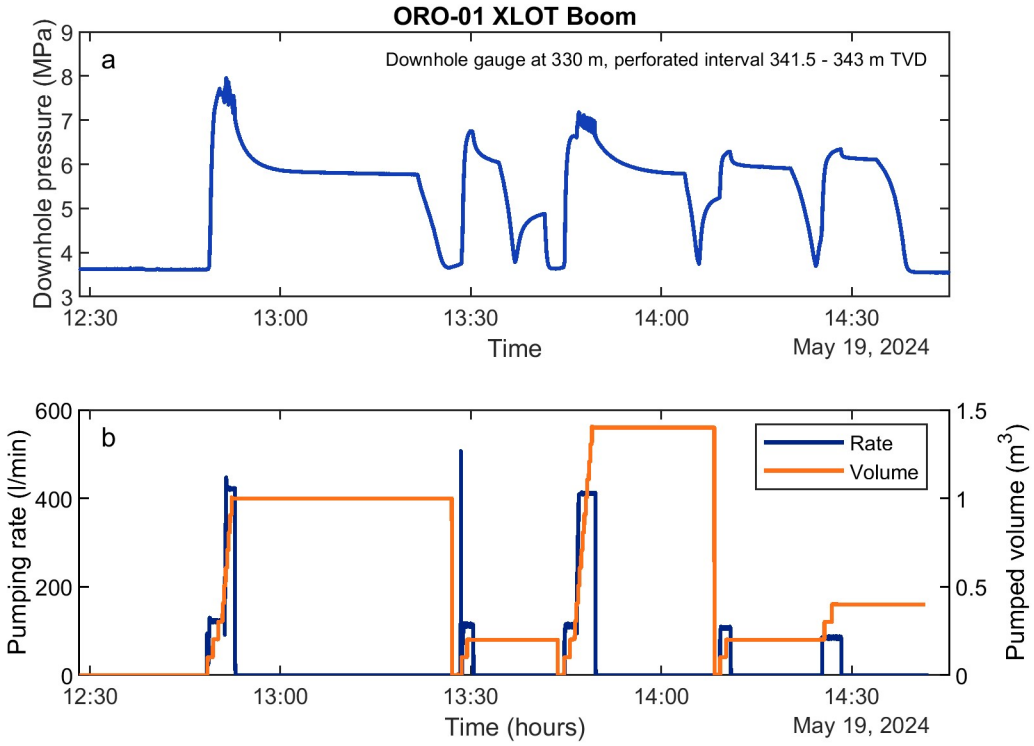

Figure 28 Extended leak-off test in the Boom Member in ORO-01. Data from www.nlog.nl. a) Pressure recorded by the down-hole pressure gauge, b) Pumping rate and pumping volume recorded at the surface in the cement pump.

The XLOT in the Asse Member consisted of 3 cycles (Figure 29). Instantaneous shut-in pressures were in the range 10.7 – 10.9 MPa, which translates to a minimum horizontal stress gradient of 18.4 – 18.7 MPa/km. Again, for a vertical stress gradient of 20 MPa/km this translates to a K_0 larger than 0.9.

Note that both measurements were performed in 'strong' (high horizontal stress), low permeable formations. In other wells, significant stress contrasts are observed across different lithologies; e.g. in the Blija-Ferwerderadeel gas field (www.nlog.nl) stress contrasts of several MPa were observed between claystone and sandstone layers at 3 km depth. It may thus be that the sandy layers in the North Sea Groups carry a lower minimum horizontal stress. A Formation Integrity Test was performed in the Brussels Sand Member up to an equivalent mud weight EMW, of 1.38, which translates to 13.5 MPa/km (End of Well Report, www.nlog.nl).

However, this does not provide any information on the minimum horizontal stress in the sandstone.

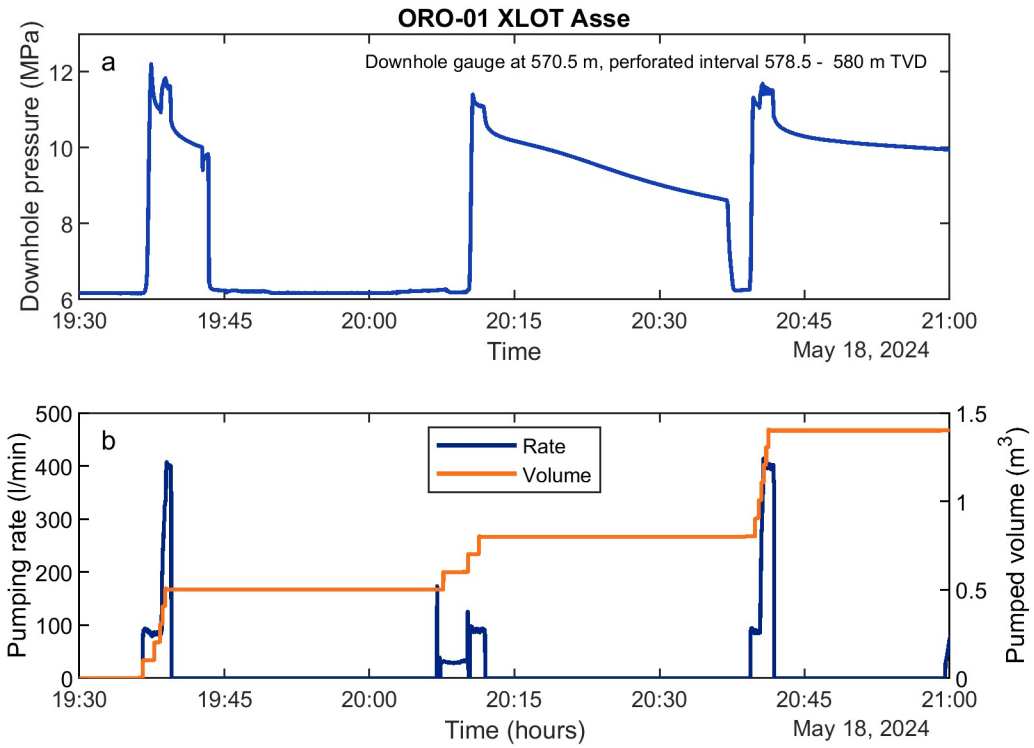

Figure 29 Extended leak-off test in the Asse Member in ORO-01. Data from www.nlog.nl. a) Pressure recorded by the down-hole pressure gauge, b) Pumping rate and pumping volume recorded at the surface in the cement pump.

The maximum horizontal stress is one of the most difficult properties to measure. An estimate of the maximum horizontal stress σ_H may be obtained from the Formation Breakdown Pressure (FBP) through (Kirsch, 1898)

$$\sigma_H = 3\sigma_h + T - P_p - FBP \qquad 7$$

Where P_p is the pore pressure and T is the tensile strength. The pore pressure was also measured in ORO-01, 5.96 MPa at 581.9 m TVD (ORO-01 EOWR, 2024), which gives a pore pressure gradient of 10.2 MPa/km. The breakdown pressure recorded in the Asse Member was 12.2 MPa, and in the Boom Member 7.7 MPa. Assuming 0 tensile strength, which is a conservative estimate, and equating the ISIPs mentioned above to the minimum horizontal stresses, a maximum horizontal stress of 19.4 – 24 MPa/km was computed. This would imply a horizontal stress anisotropy (σ_H/σ_h) of at least 1.1 up to values where σ_H is larger than σ_v (strike-slip faulting regime). However, we do note the Kirsch equations on which Equation 7 is based may not hold for cased and cemented boreholes as in the case for ORO-01. Tentatively, we propose to use 1.1 for the ratio between σ_H/σ_h and we recommend to perform further XLOTs or other stress tests in open hole settings in the North Sea Groups to constrain σ_h as well as σ_H. In addition, other means for σ_H determination could be done as follow-up such as considering wellbore breakouts and drilling-induced fractures.

Image logs can be used to determine the direction of σ_H by looking at breakouts and drilling induced fractures. Breakouts in CAL-GT, in the Peel Maasbommel Complex (PMC) just north of

the RVG, indicate a direction of 130° (Osinga & Buik, 2019). The focal mechanisms of the Roermond earthquake indicated a σ_H direction of 139 °C (Camelbeeck & Van Eck, 1994). The study of Mechelse (2017) investigated the σ_H direction in the Netherlands based on image logs, but no such logs were available in the RVG, or in the North Sea Groups. For follow-up study it is recommended to investigate newly acquired image logs in the North Sea Groups, e.g. those acquired within the SCAN program. Based on the literature, we recommend a σ_H direction of 135°.

3.11.3 Pore pressure

There are only a few pressure measurements in the North Sea Groups, most of which were taken in the northern offshore (Verweij & Hegen, 2015). These measurements suggest there are no overpressures in the Upper North Sea Group, but overpressures may exist below 1000 m depth. Pressures measured in ORO-01 were 5.96 MPa at 581 m TVD, translating to a pressure gradient of 10.2 MPa/km. This is consistent with a normal hydrostatic gradient of waters of low salinity and a density of ~ 1020 kgm^{-3} (Figure 14). Hence, a pressure gradient of 10.2 MPa/km is recommended for the geomechanical models in Chapter 4.

3.12 Plastic bulk properties

In the DIANA FEA analysis the Modified Cam Clay (MCC) material model (Munda et al., 2014; Roscoe & Burland, 1968) is used to model elastoplastic reservoir deformation (see Section 4.2.1 for this material choice). The Modified Cam Clay model is a specific formulation of the Egg Cam Clay material model (van Eekelen & van den Berg, 1994) and is implemented as a standard material model in DIANA FEA. The Modified Cam Clay model is a so-called critical state soil mechanics model. Such a model contains the following ingredients: A yield surface describing the effective stresses at which plastic deformation occurs (below this surface, the material behaves elastically), a hardening rule that defines how the yield surface expands with ongoing elasto-plastic deformation, and a flow law describing the magnitude and direction (in principle strain space) of plastic deformation (see Equations in Section 4.2.1). Although there is a variety of flavours for the above set of ingredients, the most used critical state framework is the (modified) Cam-Clay model and its plethora of variations (Wood, 1990) (Figure 30).

The required model parameters for the (Egg) Cam Clay model are, aside from elastic parameters and porosity already discussed earlier, the slope of the critical state line M and the hardening parameters κ and λ. These describe elastic and plastic hardening, respectively. These values have not been determined for North Sea Supergroup sediments. Therefore, a small literature study was conducted to find published values for these parameters, for both soils (loose sand and clay) and (weakly) consolidated sedimentary rocks.

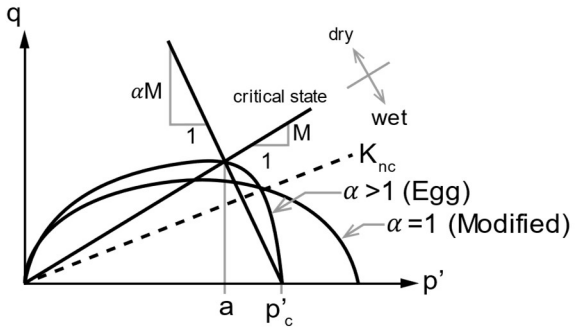

Figure 30: Sketch of the Cam-Clay model (DIANA manual, https://manuals.dianafea.com) showing the critical state line with slope M and the elliptical and egg-shaped yield surfaces in p' versus q space, where p' and q are the effective mean stress and deviatoric stress.

Not every Cam-Clay formulation utilizes the same parameterization for the hardening parameters, and thus the pool of literature with calibrated values for parameters κ and λ on consolidated materials is fairly small. Representative values for these three values have been obtained by Cassiani et al. (2017) from fitting a variant of the Cam-Clay model to the experimental data on poorly consolidated sediments from a number of other studies (Table 7). Here, the top row shows parameters for a Slochteren Sandstone sample. The other samples are poorly consolidated sandstone with large shaley fractions from the Adriatic basin. They may be somewhat similar to the RVG sediments, although they were recovered from greater depth (around 3000 m). Hence, these model parameters should be considered as a first estimate. Parameter M is used in every variation of the Cam-Clay model. Nguyen et al. (2014) found M = 1.2 for poorly consolidated Otter Sherwood sandstone.

List of model parameters calibrated for the datasets considered in this work.

	Sample ID	λ	κ	$\delta = b$	M	e_0
Pruiksma et al.[49]		0.011	0.0035	0.022	2.2	0.4
Papamichos et al.[74]	SANDST03	0.025	0.0051	0.03	1.33	0.07
Papamichos et al.[74]	SANDST04	0.032	0.0055	0.03	1.33	0.1
Hueckel et al.[34]	Tea 1—No Aging	0.07	0.02	0.041	1.6	0.3
Hueckel et al.[34]	Tea 1—Aging	0.07	0.02	0.041	1.8	0.3
Hueckel et al.[34]	Dalia 1—A1	0.11	0.015	0.04	1.8	0.85
Hueckel et al.[34]	Dalia 1—A2	0.098	0.015	0.04	1.8	0.85
Hueckel et al.[32]	Amelia 15	0.075	0.01	0.021	2.5	0.48

Table 7: Calibrated Cam-Clay hardening parameters and critical state line slope (from Cassiani et al., 2017).

We note that there are plenty of studies that have looked at plasticity in sandstones (Baud et al., 2006; Grueschow & Rudnicki, 2005; Pijnenburg, 2019; Pijnenburg et al., 2019; Wong et al., 1997). These studies find phenomenologically similar behaviour to the Cam Clay critical state model, with a brittle failure envelope similar to the critical state line and a curved plasticity cap equivalent to the yield surface. However, these studies all present their own parametrizations for these model features. Converting these parameters to the parameters expected by the (Egg) Cam-clay model is beyond the scope of this study, but converting these to 'standard' MCC model can be considered for follow-up studies.

For loose sediments (clays and sands), we utilize the values used as standard for geotechnical design (NEN, 2012). The listed parameters that represent plastic and elastic hardening for a variety of clay and sands are $C_c \frac{1}{1+e_0}$ and $C_{sw} \frac{1}{1+e_0}$, these can be converted to the necessary hardening parameters hardening parameters κ and λ by the following conversion (Den Haan et al., 2004):

$$\kappa = (1+e)(1+2k_0)\,\frac{1-\nu}{1+\nu}\,\frac{C_{sw}}{1+e_0}\,\frac{1}{\ln(10)} \qquad 8$$

$$\lambda = (1+e)\left(\frac{C_c}{1+e_0}\frac{1}{\ln(10)} + \left[(1+2k_0)\,\frac{1-\nu}{1+\nu} - 1\right]\frac{C_{sw}}{1+e_0}\,\frac{1}{\ln(10)}\right) \qquad 9$$

Here, the desired parameters depend on void ratio e, Poisson's ratio ν and horizontal to vertical stress ratio k_0. Utilizing the representative values for these parameters also used in the SRIMA analysis, the NEN-based hardening parameters κ and λ are listed in Table 8. We note that the NEN values have been obtained experimentally at a maximum vertical stress of 100 kPa, which is less than the vertical stress in the RVG North Sea Supergroup sediments. These hardening parameters are therefore probably overpredicting plasticity somewhat.

Table 8: First two columns: Elastic and plastic hardening parameter values for soils from the NEN norm (NEN, 2012). Last two columns: The NEN parameter values converted to the desired form required in the Modified Cam Clay model.

Soil type	*Level of consolidation*	$C_c / (1+e_0)$	$C_{sw} / (1+e_0)$	κ [1]	λ [1]
Sand, clean	Loose	0.0115	0.0038	0.0028	0.0075
	Intermediate	0.0038	0.0013	0.0010	0.0025
	Compact	0.0023 - 0.0015	0.0008 - 0.0005	0.0006 - 0.0004	0.0015 - 0.0010
Sand, weakly clayey		0.0051 - 0.0035	0.0017 - 0.0012	0.0013 - 0.0009	0.0033 - 0.0023
Sand, strong clayey		0.0115 - 0.0058	0.0038 - 0.0019	0.0028 - 0.0014	0.0075 - 0.0038
Clay, clean	Loose	0.3286	0.1095	0.0806	0.2146
	Intermediate	0.1533	0.0511	0.0376	0.1001
	Compact	0.0920 - 0.0767	0.0307 - 0.0256	0.0226-0.0188	0.0601 - 0.0501
Clay, weakly sandy	Loose	0.2300	0.0767	0.0565	0.1502
	Intermediate	0.1150	0.0383	0.0282	0.0751
	Compact	0.0767 - 0.0460	0.0256 - 0.0153	0.0188 - 0.0113	0.0501 - 0.0300
Clay, strongly sandy		0.0920 - 0.0164	0.0307 - 0.0055	0.0226 - 0.0040	0.0601 - 0.0107

[1]: Values conditional on $\nu = 0.35$, $\varphi = 0.29$, and $k_0 = 0.75$

4 First-order assessment of stress changes & fault reactivation

In this chapter, model results of stress changes and fault reactivation resulting from geothermal production from the North Sea Groups are summarized. The North Sea Group parameters summarized in the previous chapter were used as a basis for the model input. Two model approaches are presented in this chapter. First, the SRIMA tool (Buijze et al., 2022; Fokker et al., 2023) is applied to the case study locations in the RVG (Figure 6). SRIMA is a publicly available tool that can be used for fault reactivation calculation and related assumptions on seismic hazard, and which has so far mainly been used for deeper geothermal projects in e.g. the Cretaceous/Jurassic formations or the Permian formations. In this report, only the pressure, temperature, stress change formulations of SRIMA are used to compute fault reactivation.

One of SRIMA's assumptions is linear elastic behaviour of the geothermal reservoir rocks. This may be adequate for the competent formations at depth, but for the poorly consolidated North Sea Group sediments plastic deformation may play a non-negligible role. To evaluate these effects, a second model study was performed where the pressure and temperature changes computed in SRIMA were translated to a Finite Element model in which elasto-plastic reservoir behaviour is modeled and compared to the linear elastic case (Section 4.2).

4.1 Stress changes and fault reactivation – Linear elastic reservoir

4.1.1 SRIMA tool for computation of stress changes, fault reactivation, and seismicity

SRIMA (Seal and Reservoir Integrity Mechanical Analysis) is a geomechanical modelling tool that can model fault reactivation and the reactivated fault area around an injection well. Radial symmetry is assumed around the injection well, and the model space consists of three horizontal layers; a reservoir formation and a seal and a base formation (Figure 31). A virtual fault without offset is present at an arbitrary location in the model space, at distance r_{fault} from the injection well. A constant flow rate is prescribed along the injection well, over the interval in the reservoir. To compute the pressure and temperature changes, advection of heat and a steady-state pressure solution is modelled in the reservoir. In the overlying and underlying layers, heat and pressure are modelled according to diffusivity laws in drained rock. The induced stresses are then calculated for these geometries based on linear poro-thermo-elasticity (see for details Buijze et al., 2022; Fokker et al., 2023).

The induced stresses are transformed to a shear stress τ (fault parallel component) a normal stress σ_n (fault perpendicular component) along the virtual fault. When the shear stress reaches the fault shear strength fault reactivation can occur, i.e. as shown in the Mohr-Coulomb failure criterion

$$\tau_f = C + \mu\sigma_n' = C + \mu(\sigma_n - p) \qquad 10$$

where C is the fault's cohesive strength, μ is the coefficient of friction, and p is the pore pressure. It is useful to quantify changes in shear and normal stress in relation to proximity to failure. A measure for this is the Coulomb Stress Change

$$\Delta CFF = \Delta\tau - \mu\Delta\sigma_n' \quad (11)$$

where $\Delta\tau$ is the change in shear stress along the fault, and $\Delta\sigma_n'$ is the effective normal stress. A positive shear stress change or decreasing effective normal stress promote fault reactivation ($\Delta CFF > 0$), whereas a negative shear stress change or positive effective normal stress change lead to a more stable state of stress on the fault.
The stress changes are combined with the in-situ (pre-injection) stresses in order to arrive at total and effective stress fields. From those, the Shear Capacity Utilization (*SCU*) is calculated on a pre-defined fault plane,

$$SCU = \frac{\tau}{\tau_f} = \frac{\tau}{C + \mu\Delta\sigma_n'} \quad (12)$$

The *SCU* is a measure that indicates criticality of the stress at the point where it is calculated, a value of 1 signifies that the stresses are critical and fault reactivation can occur. *SCU* can be used to determine the area that can be reactivated during shear failure. For a more extensive description we refer to (Fokker et al., 2023). Both the ΔCFF and the *SCU* are used as metrics for fault reactivation in the results sections.

Other metrics are used to illustrate the effect of the distance of the virtual fault to the injection well. To this end stresses were computed along a horizontal line at a certain depth within the reservoir interval, starting at the wellbore. At each point along the line, these stresses are transformed to shear and normal stresses on the assumed geometry of the virtual fault and the associated ΔCFF and *SCU.* Along this line, the distance at which the ΔCFF exceeds 1 MPa is defined as

$$r_{CFF-1MPa} = r \text{ where } \Delta CFF(r) > 1\ MPa \quad (13)$$

Which is useful to depict the spatial extent of the stress perturbation with distance from the injection well r. This metric has also been compared with the radius of the cooled part of the reservoir r_{cooled} which is the distance from the well to the location for with the temperature change is 50% of the maximum temperature change.

The advantage of SRIMA is that it is a fast tool that can explore the uncertainty in input parameters. Therefore, the tool includes a stochastic approach where the input parameters are independently and randomly varied, assuming a uniform distribution over the uncertainty range. The stochastic analysis allows, amongst others, to calculate the probability of exceeding a ΔCFF of 1 MPa at a certain distance from the fault, and the probability of fault reactivation as a function of distance from the well – i.e. the fraction of simulations during which reactivation was observed at a particular distance from the well, out of the total number of simulations. Finally, it facilitates the identification of the driving parameters by investigating the influence of the parameter values on the distribution of these measures.

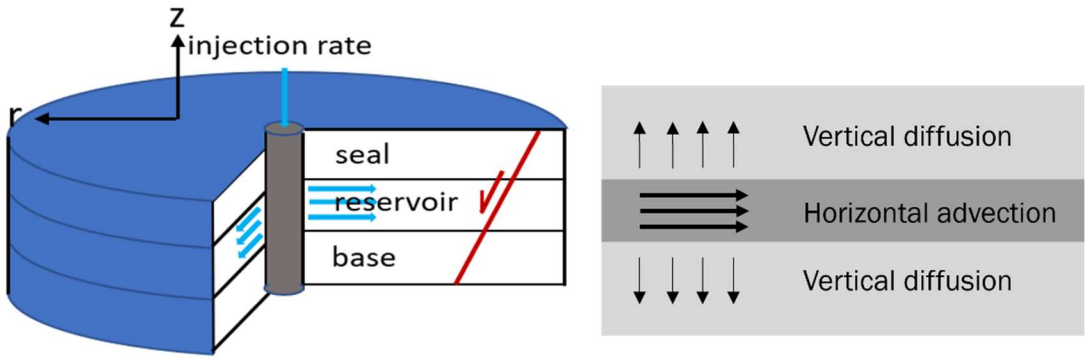

Figure 31 Radially symmetric geometry used in SRIMA for the analysis of thermo-elastic and poro-elastic stresses due to injection of cold fluids. Red line: virtual fault.

4.1.2 SRIMA model scenarios

Four cases have been chosen as representative cases for the RVG (Section 3.3). Case 1 has been chosen as representative for the centre of the graben (Figure 7). The Breda Member here is relatively thick, making this and attractive target due to a large transmissivity. However, the exact depth extent and lithology of the aquifer is poorly known. Therefore, we explore Case 2 which is similar to Case 1, but with a smaller aquifer thickness. Case 2 is also the case for which a comparison with the poro-elastic-plastic simulations in the following Section 4.2 is made. Case 3 and case 4 were selected based on their proximity to either the south-west or north-east side of the graben. The input parameters for these cases were based the parameters from the nearby Veldhoven 01 well (VEH-01) and Keldonk 01 well (KDK-01) and from the fault models of the RVG in the respective locations.

The input for these cases has been taken from the description in the previous chapter and is summarized in Table 9. Fault parameters are taken from Section 3.9. In the default simulations for each case, we place the faults at a position that intersect the injection well. This is a conservative assumption, as faults are typically avoided during the drilling of a geothermal well, and geothermal doublets are typically placed at some distance from known faults. However, in the sensitivity analyses the distance of the fault to the well is included as a variable. Thermal and flow properties come from Section 3.4 and 3.6; values in the seal and base were chosen to be low to minimize pressure effects there (permeability of 0.001 md; porosity of 0.05). Elastic and thermoelastic properties come from Section 3.7; fault friction properties from Section 3.10. Stresses come from Section 3.11. The range for the minimum in-situ stresses at the reservoir top is based on an average gradient of 14 – 17 MPa / km, and a default gradient of 15 MPa / km. The vertical stress gradient is taken 20 MPa/km. The minimum horizontal stresses in shale layers are typically larger than in the reservoir (and thus the shales are more stable). Therefore, we have included the possibility of a stress contrast between the seal and the reservoir of 2.0 MPa to account for the seal being more shaley than the sandy reservoir in Cases 1 (1.0 MPa for Case 2, 3 and 4). For the maximum horizontal stress we take values of 1.1 times the minimum stress and a direction with some uncertainty in the NW-SE direction.

Table 9 SRIMA default input parameters, and the lower and upper values for the stochastic simulations, for the four test cases. The parameters are based on the inventory presented in 3 and represent the best current estimates.

Input parameter	Case 1	Case 2	Case 3	Case 4
Top depth	470 m	675 m	340 m	330 m
Thickness	510 (509 – 760) m	100 (50 – 150) m	330 (329 – 390) m	260 (259 – 420 m)
N/G	90 (80 – 91)%	90 (80 – 91)%	90 (75 – 92)%	90 (75 – 95)%
Fault Dip	60 (50 – 70)°	60 (50 – 70)°	55 (50-60)°	60 (50 – 70)%
Fault Strike	NNW – SSE (160°)	NNW – SSE (160°)	NNW – SSE (160°) and NW – SE (135°)	NW – SE (135°)
Reservoir temperature	30°C	30°C	23°C	24°C
Reservoir pressure at top	4.8 MPa	6.75 MPa	3.5 MPa	3.4 MPa
Salinity	2000 (1000 – 10000) ppm	2000 (1000 – 10000) ppm	2000 (1000 – 10000) ppm	2000 (1000 – 10000) ppm
Reservoir Permeability Seal permeability	330 (100 – 600) mD 0.001 mD	330 (100 – 600) mD 0.001 mD	400 (300 – 450) mD 0.001 mD	550 (400 – 700) mD 0.001 mD
Reservoir Porosity Seal porosity	29% 5%	29% 5%	29% 5%	29% 5%
Heat capacity	800 J/kg.K	800 J/kg.K	800 J/kg.K	800 J/kg.K
Thermal conductivity	1.6 W/m.K	1.6 W/m.K	1.9 W/m.K	1.5 W/m.K
Minimum horizontal stress at top reservoir	7.05 (6.58 – 7.99) MPa	10.13 (9.45 – 11.48 MPa)	5.10 (4.76 – 5.78) MPa	4.95 (4.62 – 5.61) MPa
Stress contrast Seal to Reservoir	-2.0 (-2.1 – 0.0) MPa	-2.0 MPa	-1.0 (-1.6 – 0.0) MPa	-1.0 (-1.6 – 0.0) MPa
Vertical stress at top reservoir	9.40 MPa	13.5 MPa	6.80 MPa	6.60 MPa
Maximum / minimum horizontal stress ratio	1.1	1.1	1.1	1.1
Max hor. stress azimuth	135 (110 – 160)°	135	135 (110 – 160)°	135 (110 – 160)°
Young's modulus	2.0 (0.2 – 4.0) GPa	3.2 GPa	2.0 (0.2 – 4.0) GPa	2.0 (0.2 – 4.0) GPa
Poisson ratio	0.35 (0.3 – 0.45)	0.35 (0.3 – 0.45)	0.35 (0.3 – 0.45)	0.35 (0.3 – 0.45)
Biot constant (all layers)	0.9 (0.5 – 1.0)	0.9 (0.5 – 1.0)	0.9 (0.5 – 1.0)	0.9 (0.5 – 1.0)
Linear thermal expansion coefficient	2.0 (1.9 – 3.0) 10^{-5} K^{-1}	1.2 10^{-5} K^{-1}	2.0 (1.9 – 3.0) 10^{-5} K^{-1}	2.0 (1.9 – 3.0) 10^{-5} K^{-1}

MC friction coefficient	0.55 (0.4 – 0.65)	0.55 (0.4 – 0.65)	0.55 (0.4 – 0.65)	0.55 (0.4 – 0.65)
Residual friction	0.35	0.35	0.35	0.35
Injection rate	300 m^3/hr	100 m^3/hr	300 m^3/hr	300 m^3/hr
Injection temperature	9°C	9°C	9°C	9°C
Injection duration	30 yr	30 yr	30 yr	30 yr

A realistic geothermal cold-water injection scenario was chosen for the model simulations in a linear elastic and a plastic reservoir, based on the Zevenbergen doublet in western Noord Brabant (Geel et al., 2022). The Brussels Sand, although from the Lower North Sea Group, and therefore older than the Breda Formation, consists also of mostly poorly consolidated sand. The Zevenbergen doublet produced at a temperature of 31.7 °C, which is comparable to the formation temperatures in the Breda Formation in the RVG. The injection temperature was 9 °C. The injection volume rate was around 130 m^3/hr, over a 165 m thick interval. We scaled the injection rate to the larger thicknesses found in our test cases, so that the volume rate per meter depth remains constant.

Model calculations were run for the four cases, using the default analyses as well as the stochastic analyses using the ranges depicted in Table 9. For the stochastic analysis, 1000 simulations were run.

4.1.3 SRIMA results for linear elastic reservoir

4.1.3.1 Cases 1 and 2 – default values and sensitivity analysis

The default values for the Case 1 resulted in fault reactivation after 10 and 30 years. No reactivation was calculated after the initial injection period of 2 years – not even while the well is penetrating the fault and immediately cools the area around the point of penetration. The propagation of the thermal front with respect to the distance from the injection well for this scenario is shown in top view in (Figure 32). After 30 years of injection, the cold front has reached a distance of ~300 m from the injection well.

The vertical profiles of temperatures, pressures and stresses are represented in Figure 33. The cooling of the reservoir rock leads to a decrease in the horizontal stresses (a decrease in σ_3), whilst the pressures increase. The temperature, pressures, stresses and the resulting change in Coulomb Stress Function (ΔCFF) and SCU on the predefined fault are presented in Figure 34, Figure 35 and Figure 36. The cooling and the resulting decrease in the horizontal stress result in a decrease in effective normal stress and an increase in shear stress (Figure 35). The net effect is a less stable state of stress on the fault, as indicated by the positive ΔCFF (Figure 36). The stress changes are such that fault reactivation occurs for this scenario. Fault reactivation occurs predominantly at the top of the fault section that is in the reservoir layer as can be observed from the $SCU > 1$ values in Figure 36. The bottom of the reservoir does not reactivate. At the top of the reservoir, the relative contribution of the temperature-induced stress change to the background stress is the largest because of the stress gradient and the considerable thickness of the injection layer with respect to the depth.

Fault reactivation will not take place in the seal even though part of the seal experiences cooling due to vertical diffusion of temperature, since in this simulation the in-situ horizontal

stress in the seal is much larger than in the reservoir and hence the stress is much more stable than in the injection layer.

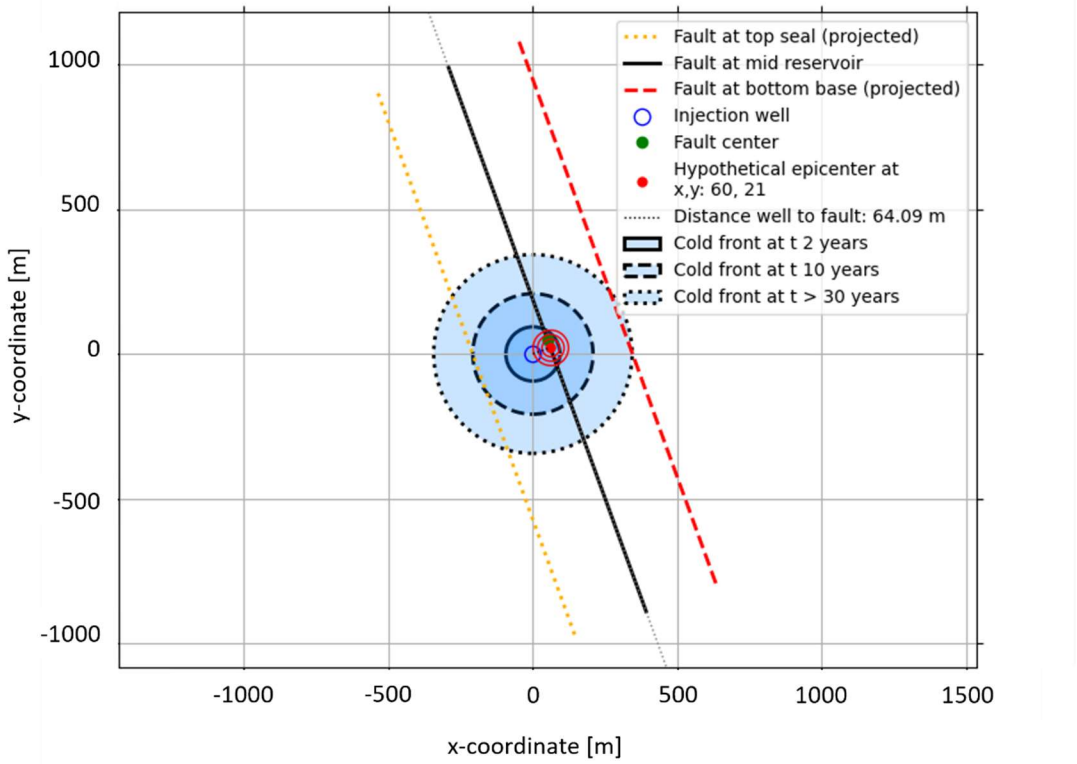

Figure 32 Base Case 1: Propagation of the thermal front with time, and indication of the hypothetical fault geometry assumed in the default scenario. Note this is a conservative estimate; normally the injection well will be placed at a distance to faults visible on seismics.

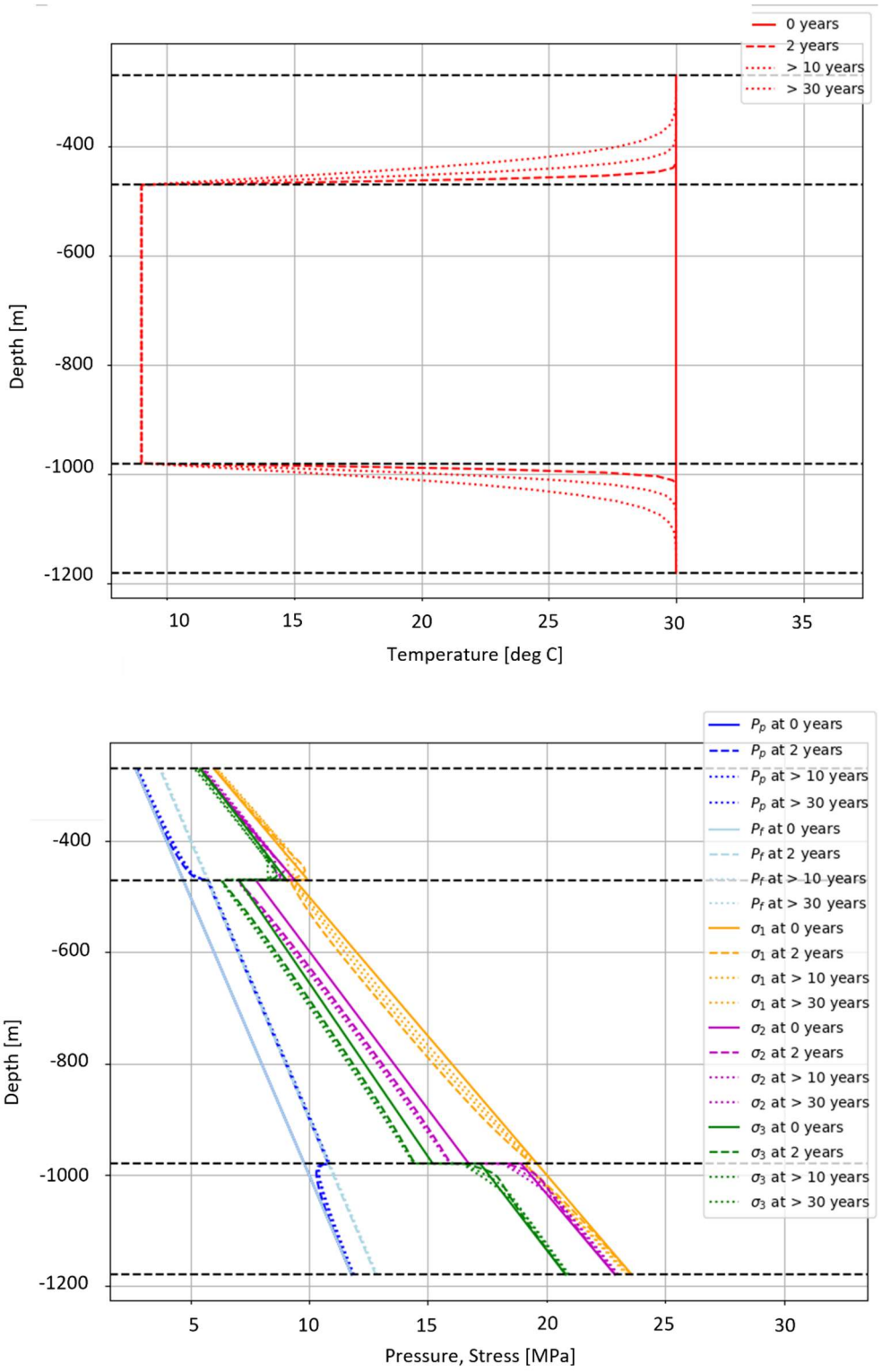

Figure 33 Base case for the default parameters of Case 1: temperature (top panel) and pressure and stress output (bottom panel) along a vertical line near the wellbore.

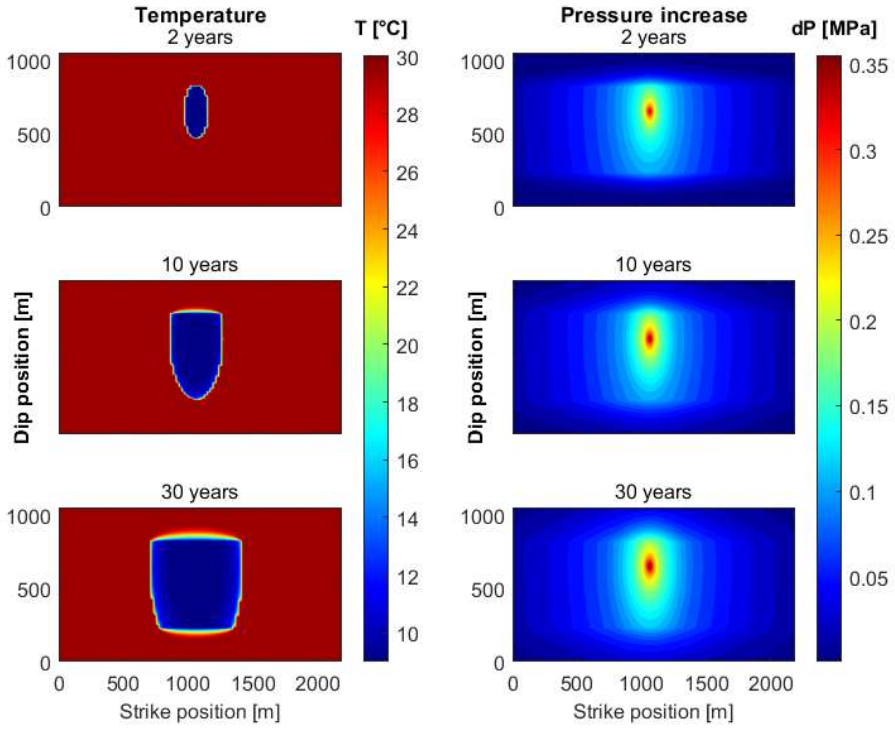

Figure 34 Temperatures and pressure increase on the predefined fault at the location of the injection well for the default parameters of Case 1.

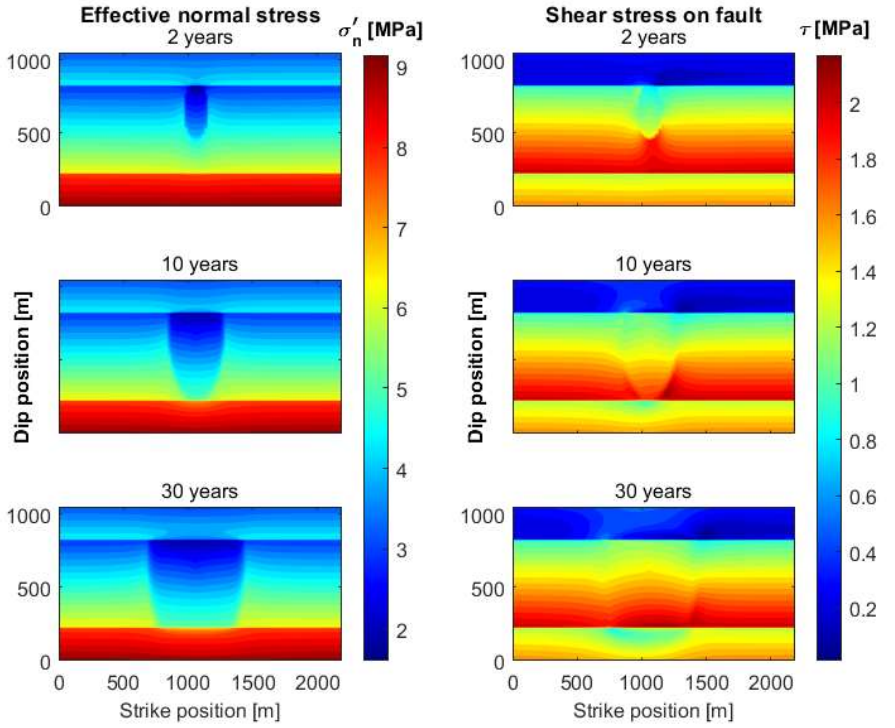

Figure 35 Effect of the temperature and pressure changes on the effective normal stress and the total shear stress working on the predefined fault for the default parameters of Case 1. A slight asymmetry in shear stress results from the misalignment between the fault strike orientation and the direction of the maximum horizontal stress.

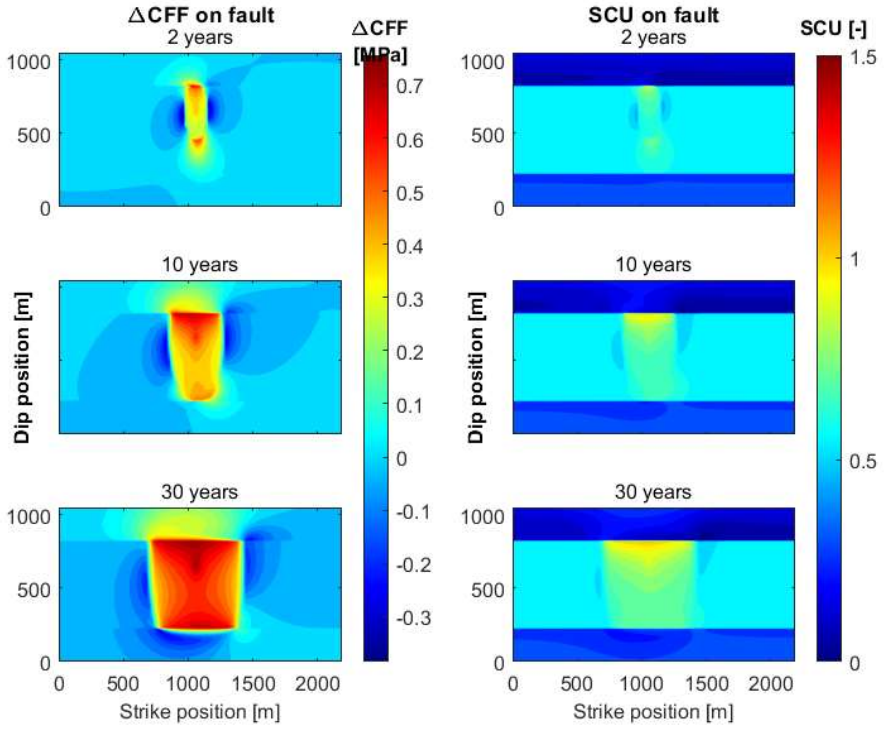

Figure 36 Stress changes on the fault at the location of the injection well, for the default parameters of Case 1. Effect of injection on the predefined fault at the location of the injection well after 2, 10, and 30 years in terms of change in Coulomb Failure Function (*ΔCFF*) and Shear Capacity Utilization (*SCU*).

In the example shown in Figure 35 and Figure 36 the fault is located at the injection well – which is a conservative estimate. The potential for fault reactivation, and the reactivated area, will decrease with distance from the fault. This is illustrated by considering the *ΔCFF* and *SCU* as a function of distance from the well, along a horizontal line in the reservoir. Figure 36 shows that the largest activation stresses occur near the top of the aquifer, therefore we have chosen a depth closely below the seal, at 90% of the thickness as the most negative scenario. Figure 37 shows the temperature and pressure increase resulting for the default parameters of Case 1. As was also visible in Figure 32, the cold front expands with time, reaches a final radius of ~300 m from the injection well. The temperature decrease is largest near the injection well, reaching 8°C. Near the cold front the temperature decrease rather abruptly decreases to zero. The pressure change follows a logarithmic function, decrease sharply with distance from the injection well. The maximum pressure change at the well (i.e. the injection pressure) is 0.65 MPa. Figure 38 and Figure 39 show the resulting effective normal stresses and total shear stresses, *ΔCFF,* and *SCU* on a fault with orientation as given in Table 9. Both these criticality metrics follow closely the temperature distribution, illustrating how predominantly the temperature change drives the (fault) stress changes. The temperature discontinuity at the cold front results in stress concentrations (Figure 38). As a result, the change in Coulomb Friction Function and the Shear Capacity Utilization (Figure 39) also show concentrations at the thermal front.

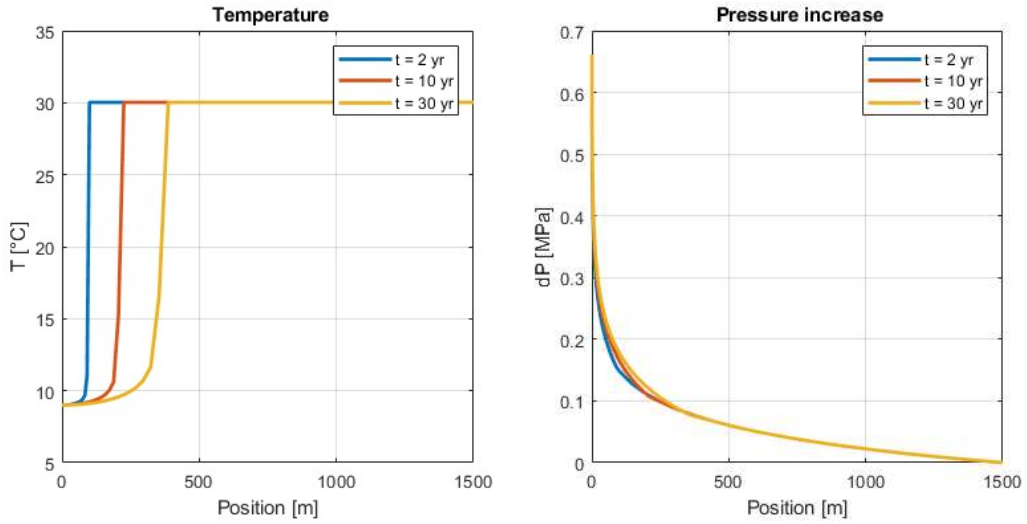

Figure 37 Temperature and pressure for the base case of Case 1 computed at 90% of the height in the reservoir in the direction of the fault, as a function of distance from the well. With time progressing, the temperature front propagates into the reservoir; the pressure disturbance is changing only marginally. The radius of the cold front r_{cooled} is ~380 m after 30 years.

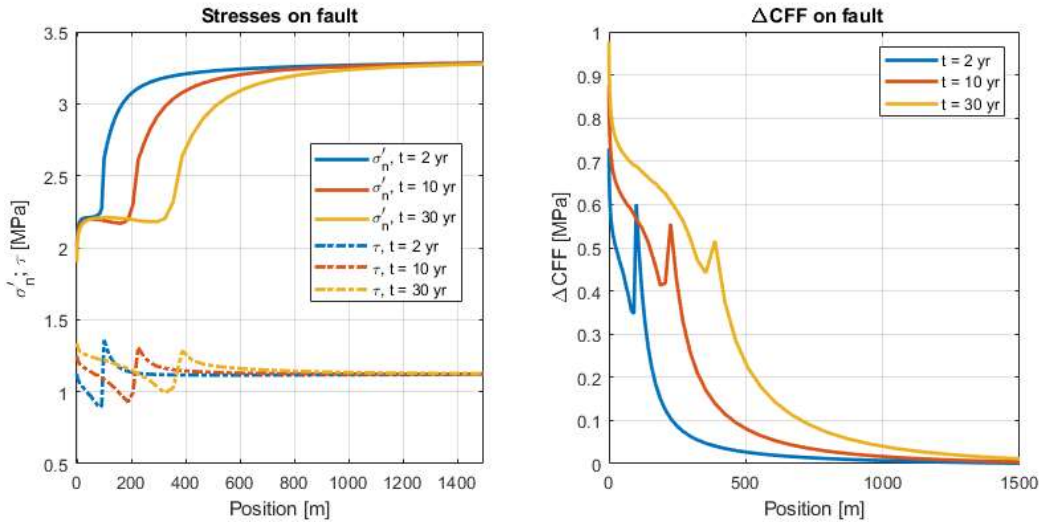

Figure 38 Effective normal stresses and total shear stresses and associated changes in the Coulomb Friction Function, computed at 90% of the height in the reservoir, as a function of distance from the well, for the default scenario of Case 1. Stresses are calculated on a fault with the default orientation in Table 9. Colous indicate the injection time. A stress concentration develops at the thermal front.

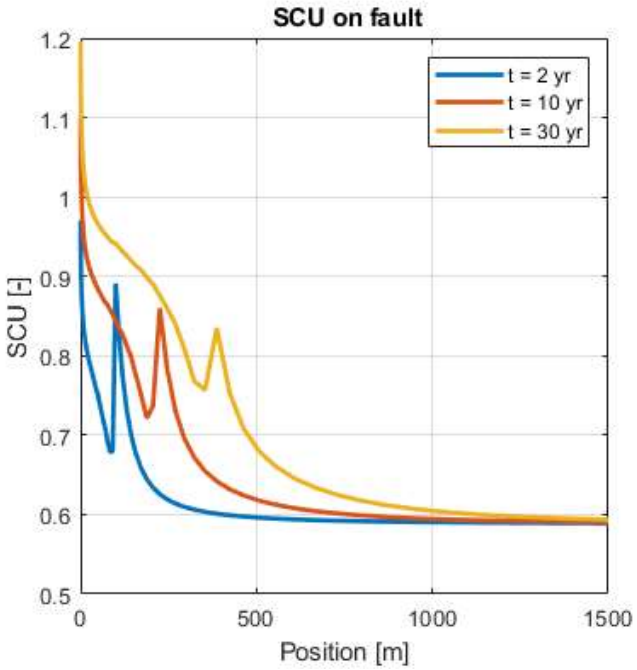

Figure 39 Shear capacity utilization (*SCU*) on a fault of given orientation, along a horizontal line at 90% of the height in the reservoir for the default orientation and parameters in Case 1.

It is instructive to show the distribution of *SCU* on the fault for a selection of the parameter variations – including the variation of Case 2 (a thinner reservoir) and the position of the well with respect to the fault. This is done in Figure 40, showing *SCU* on the fault plane for 8 sensitivity runs. Decreasing the Young's modulus in seal and base from the default value of 2 GPa to 0.5 GPa causes concentration of activation in the reservoir layer. The same decrease in Young's modulus over all three formations results in reduced thermoelastic stress changes and prevents fault reactivation from happening in the current scenario, illustrating how important a correct assessment of Young's modulus is for fault reactivation. A reduced Young's modulus in the injection layer causes fault reactivation to happen in the seal only, resulting in a smaller reactivated fault area. Further, a reduced friction coefficient or a reduced virgin minimum in-situ stress increase initial criticality and increase the reactivated fault area. Stress contrasts (i.e. higher virgin minimum horizontal stresses in the seal compared to these in the reservoir) cause localization of fault reactivation in the reservoir formation. The thinner reservoir formation assumed in Case 2 (sensitivity G) alleviates the effect of the layer thickness and makes fault reactivation happening more evenly over the layer thickness, but the width of the area does not change much. Placing the well further from the fault delays the start of cooling the fault, but once the cold front arrives at the fault, fault reactivation also occurs. The question about the relationship of distance to the fault and reactivation potential will be addressed in the context of the stochastic analysis (section 4.1.3.2).
The wide range of fault reactivation behaviour (reactivation vs no reactivation, reactivation time, reactivated area) observed in the sensitivity analysis underpins the need for good site-specific data.

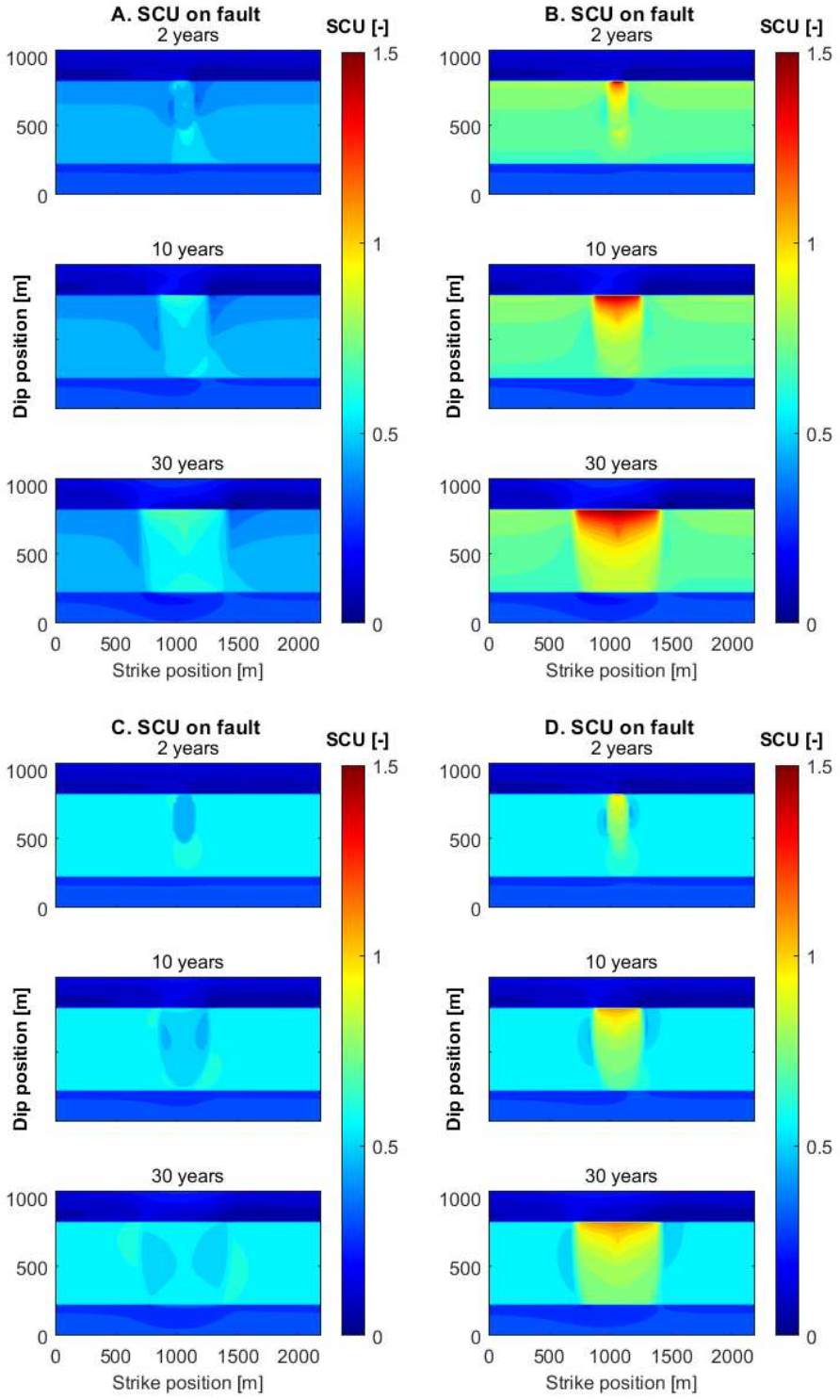
A. SCU on fault
2 years
10 years
30 years
SCU [-]
1.5
1
0.5
0
1000
500
0
Dip position [m]
0
500
1000
1500
2000
Strike position [m]
B. SCU on fault
C. SCU on fault
D. SCU on fault

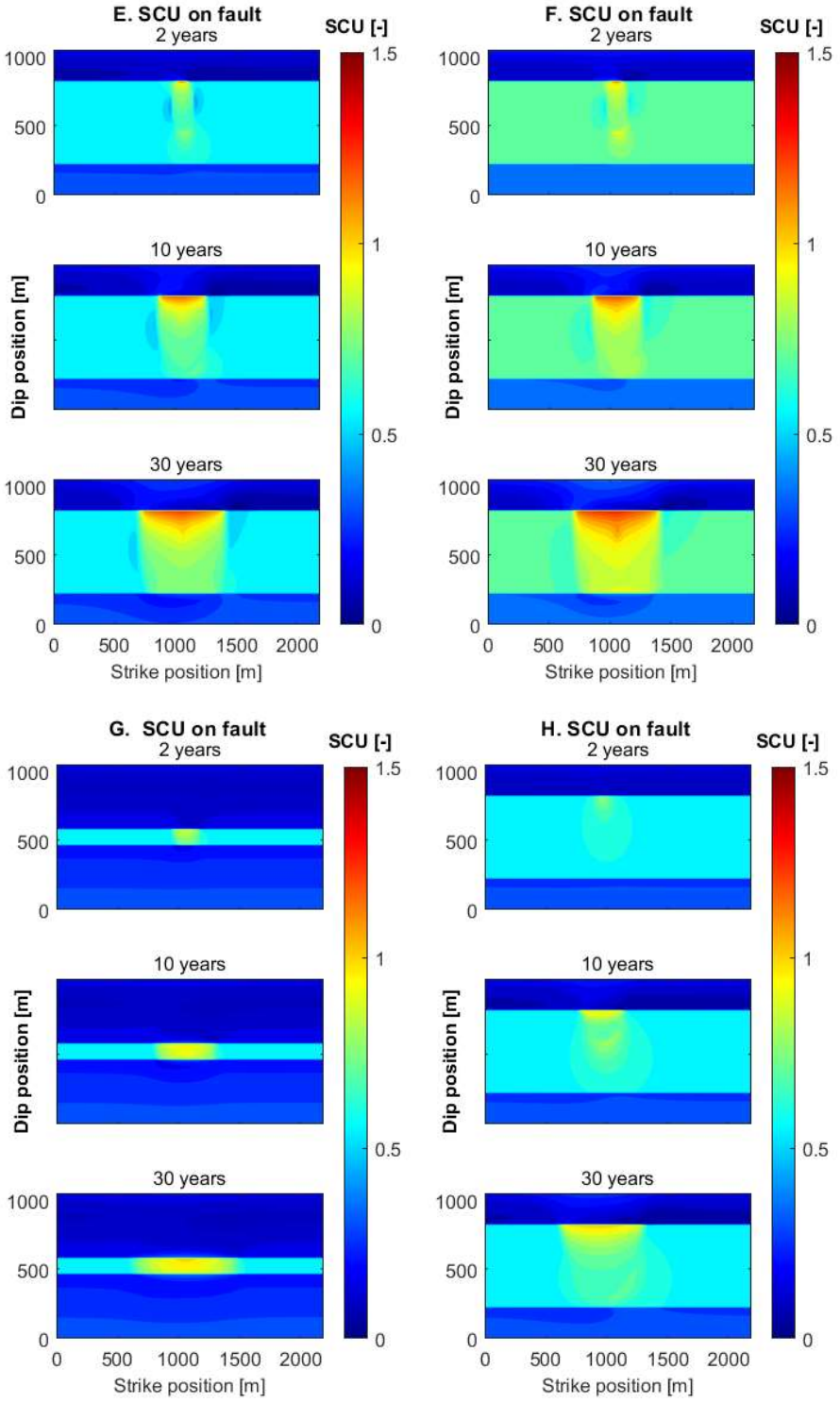

Figure 40 Shear Capacity Utilization (*SCU*) on the fault plane for 8 sensitivity runs. A: Increased horizontal stress in the reservoir (7.55 MPa). B. Decreased horizontal stress in the reservoir (6.55 MPa). C. Decreased elastic modulus in injection layer (0.5 GPa, vs. the default value of 2 GPa). D. Decreased elastic modulus in seal and base (0.5 MPa). E. Increased Poisson ratio in injection layer (0.45). F. Decreased friction coefficient (0.45). G. Thinner injection layer (Case 2). H. Fault at 300 m distance from the well.

4.1.3.2 Cases 1 and 2 – stochastic analysis

The stochastic analysis was performed along the same horizontal line just below the seal (at 90% of the thickness) in the direction of the fault with the orientation from Table 9. The results are presented in Figure 41. The first observation that can be made is that 60% of the cases show fault reactivation when the fault is intersected by the well (i.e. at a distance of 0 m). However, the probability for fault reactivation decreases with distance from the fault. After a relatively small reduction in fault reactivation probability with distance from the well, a fast reduction of reactivation probability is observed when the fault is well outside the cooled zone. This becomes more insightful when normalizing the distance to the well with the radius of the cold front (defined as the distance where the temperature is the average of injection and virgin reservoir temperature). Beyond a normalized distance of 1 (i.e. at a location outside the cooled rock volume), the reactivation probability drops rapidly. At normalized distance of 1.5, less than 10% of the model simulations resulted in fault reactivation; at a normalized distance of 2.0, this value has further dropped to about 2%. Hence, when the injection well is placed further from the fault, the reactivation potential reduces dramatically.

We see that the probability of reactivation is strongly connected with the distance to the thermal front. When a fault is cooled, the probability of fault reactivation is largest, but it is relatively insensitive to the precise position within the cooled region. The explanation for this observation is the stress concentration at the position of the thermal front and the decrease of thermal stresses beyond it. For the position of the well with respect to the fault, an important issue thus is whether the thermal front that is induced by the injection of cold water approaches and crosses the fault. Another important issue is whether the well actually penetrates the fault: the probability of fault reactivation at, or very close to the wellbore is 5-10% larger than in the remainder of the cooled zone.

We have ranked the results against the uncertain parameters in Figure 42. First, the maximum distance for a fault from the wellbore (r_{fault}) where reactivation can take place has been determined, for each ensemble member. Then, for each input parameter that was varied in the stochastic analysis (e.g. H_{res}, k_{res}) the results were binned in 9 bins, spanning the full range between the minimum and maximum value of the parameter that was explored in the stochastic analysis. Per bin, the normalized fraction of model results for a certain value of r_{fault} are indicated with the different colors (the first bin represents the cases without activation, then we have bins of r_{fault} < 120 m, between 120 m and 200 m; between 200 m and 340 m, etc). For instance, within the first E_{res} bin between 0.2 and 0.622 GPa, we see no reactivation for most cases; and only a few reactivation cases with r_{fault} values smaller than 120 m: there are no cases with such a low reservoir modulus that result in large distances where activation can occur. For the last E_{res} bin between 3.578 and 4.0 GPa, for more than 50% of the model runs fault reactivation can occur at distances beyond at 340 m from the well. This indicates that with increasing E_{res} the probability that fault reactivation will occur at a certain distance from the injection well increases.

We see that here as well the main influences are from the mechanical parameters (the horizontal / vertical stress ratio K_o, the elastic moduli in the reservoir and the friction parameters). These are the parameters to target when trying to reduce the uncertainty.

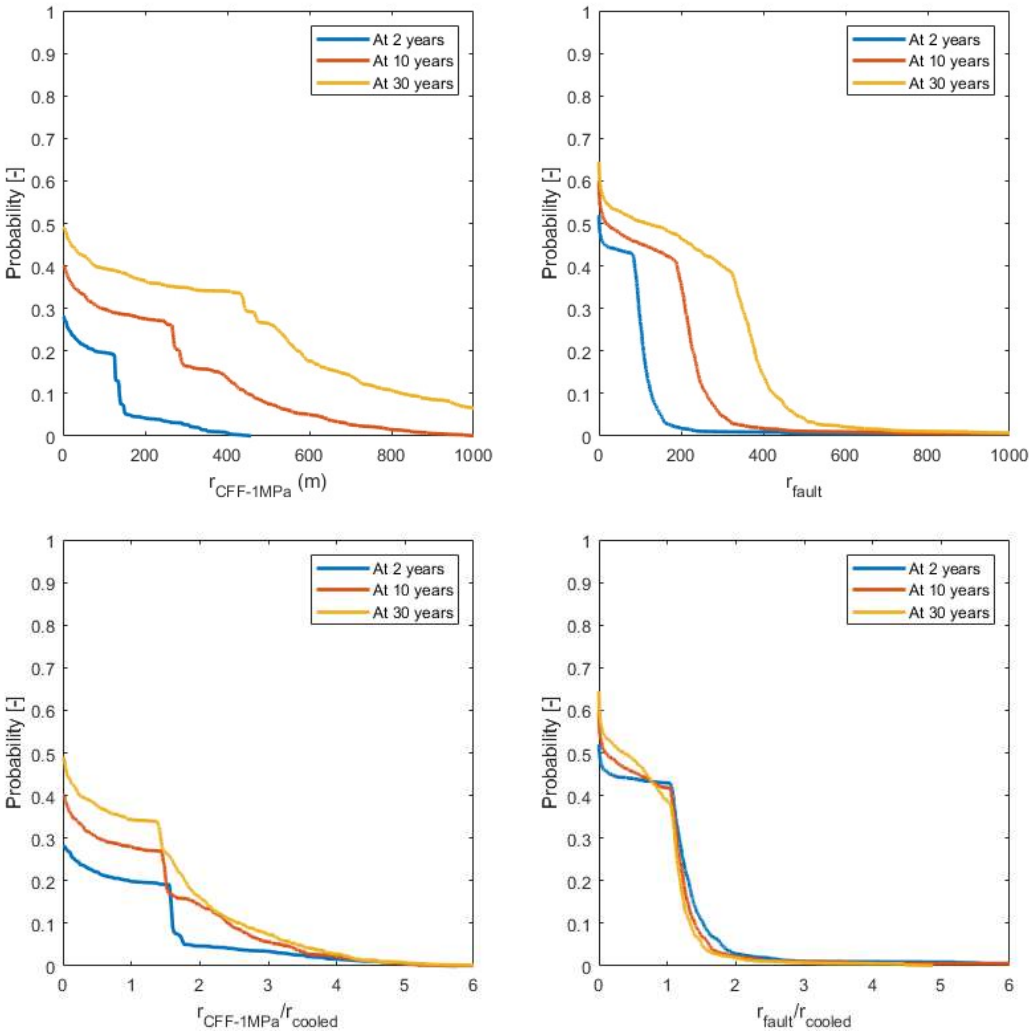

Figure 41 Results of the stochastic analysis of Case 1: The plots show (on the vertical axis) the probability for the fault reactivation metric on the x-axis. Top row left: Probability that a “significant stress change” is found on a fault located further than the value on the x-axis. Top row right: probability that reactivation occurs at a fault located further than the value on the x-axis. Bottom row: Same numbers but with the horizontal position scaled to the radius of the cooled area. 40% of the cases do not exhibit critical behaviour; a small percentage of the cases start with critical behaviour from the start, as indicated by the probability of finding a critical radius equal to the reservoir size not being zero. Significant stress changes and criticality are for 90% of the cases constrained within 1.5 times the radius of cooling

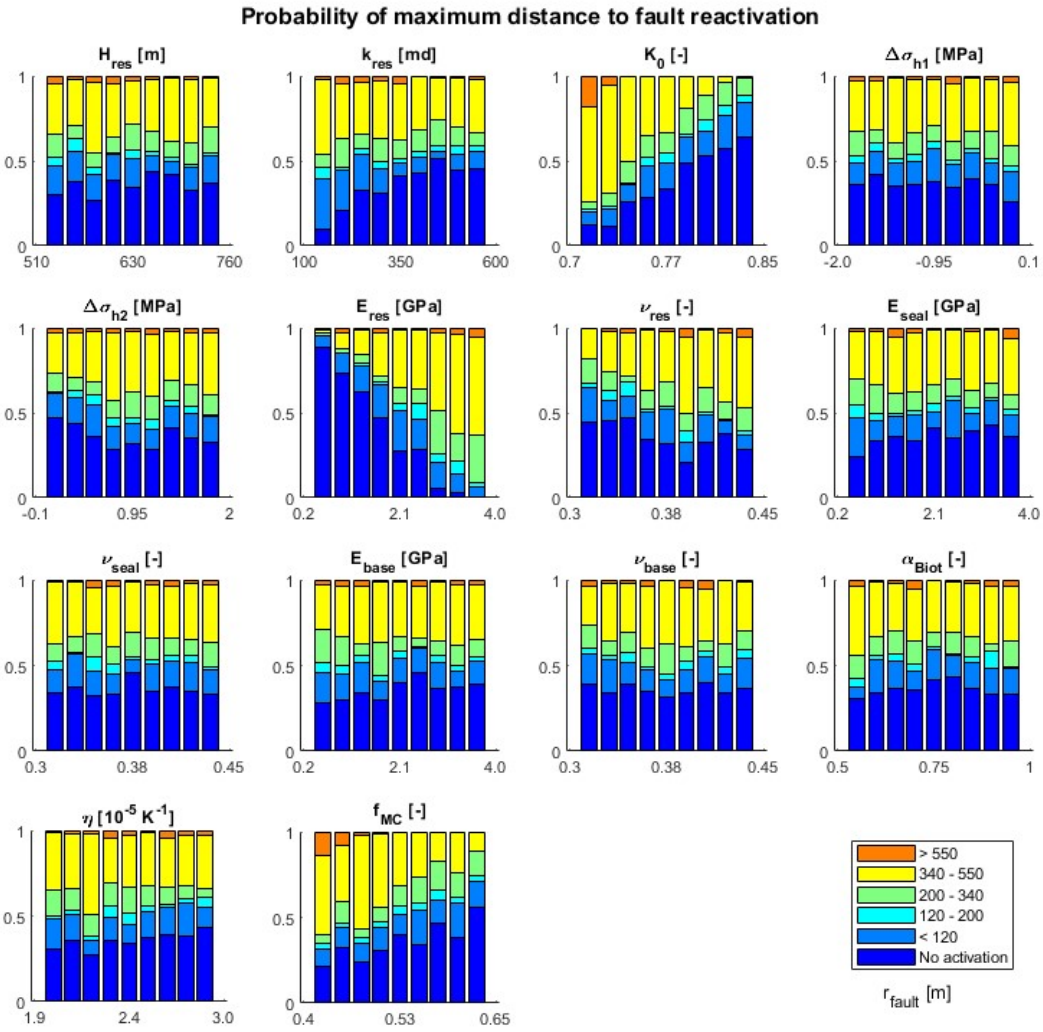

Figure 42 Results of the stochastic analysis of the results on a horizontal line just below the reservoir top for Case 1. The 14 subplots show the results according to a specific parameter: reservoir thickness (H_{res}), reservoir permeability (k_{res}), horizontal / vertical stress ratio (K_0), stress contrast at the seal-reservoir interface ($\Delta\sigma_{h1}$), stress contrast at the reservoir-base interface ($\Delta\sigma_{h1}$), reservoir Young's modulus (E_{res}), reservoir Poisson ratio (ν_{res}), seal Young's modulus (E_{seal}), seal Poisson's ratio (ν_{seal}), base Young's modulus (E_{base}), base Poisson ratio (ν_{base}), Biot coefficient (α_{Biot}), linear thermal expansion coefficient (η) and Coulomb friction parameter (f_{MC}). For each input parameter shown in the subplots, the model runs have been grouped into 9 equally sized bins. Within each bin, the coloured bars indicate the fraction of model results within a certain range of maximum distance between well and fault for which reactivation can take place (r_{fault}). For example, for each bin, the size of the darkest blue pillar corresponds to the fraction of model runs for which no fault reactivations was observed, whereas the orange bar indicates the fraction of model results for thich r_{fault} was >550 m.

The stochastic analysis with Case 2 gave qualitatively similar results as Case 1 (Figure 43). The effect near the well is larger: instead of an increase of 5-10% when the well penetrates the fault, we see here an increase of 20-30%. This is because the aquifer thickness has been reduced more than the injection rate, which results in larger injection pressures. Again, the two important issues are the position of a potential fault with regard to the cooling front, and the increased probability of critical behaviour in the vicinity of the well, due to the locally increased pressure. Beyond the thermal front, stress levels reduce quicker than in the thick-reservoir case.

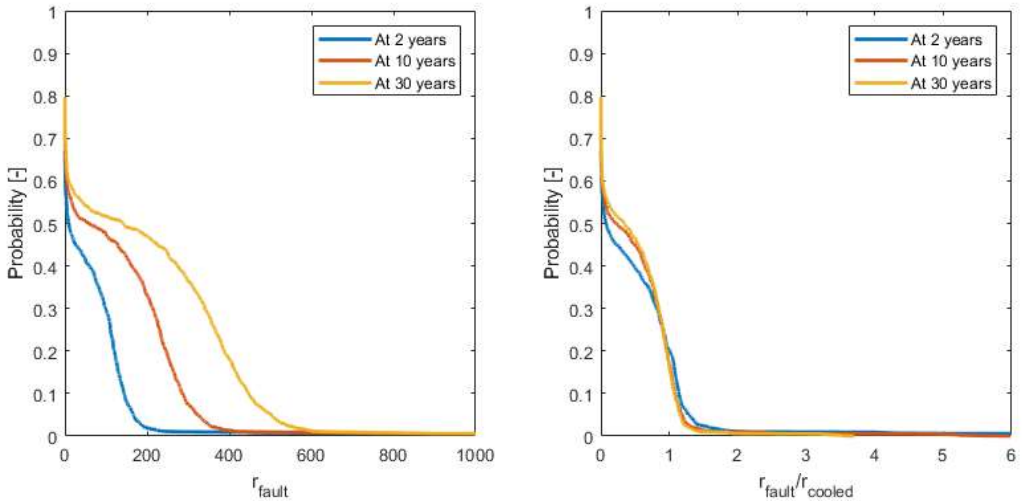

Figure 43 Results of the stochastic analysis of Case 2, for description see Figure 41: Probability that a fault at that distance is reactivated. 80% of the cases at 30 years do not exhibit critical behavior; this reduces to less than 60% for short distances to the well. Criticality is for 90% of the cases constrained within 1.2 times the radius of cooling.

4.1.3.3 Cases 3 and 4 – default values

We present the default, base case result on the predefined fracture in Figure 44. Again, the well is assumed to penetrate the fault in the base case. The main differences between Case 1 on one side and Cases 3 and 4 on the other, from a simulation point of view, are that the latter cases are shallower, thinner, and cooler. The shallower depths result in smaller initial stresses, which increases the relative thermoelastic contribution of the thermal stress with respect to the initial stresses. Conversely, the smaller reservoir temperatures decrease the temperature difference between injected fluid and the reservoir, which decreases the thermoelastic contributions. The poroelastic contribution to the stress is rather limited for all cases, thanks to the large permeability and the thickness of the target injection layers. Besides, the poroelastic stresses are concentrated in a small area around the injection well.

The potential for fault reactivation for the base cases for both Case 3 and 4 are slightly more critical than for Case 1. The *SCU* at the location of the injection well is larger, and higher values for *SCU* are obtained further away from the well. Case 4 is slightly more critical than Case 3, presumable due to the smaller reservoir thickness. This is also clear from the *SCU* on a line in the direction of the fault, as presented in Figure 45. This figure also helps to judge the importance drilling at a distance from the faults. In the first place, when the fault is located at the location of the injection well, the effect of the pressure disturbance can be recognized. A peak in the *SCU* is observed immediately around the injection well. Here we must note that drilling into a fault may invoke problems that are not modelled in SRIMA, like preferential flow into the fault if it has a large permeability. In the second place, the main effect on the in-situ stresses and the shear capacity is associated with the cooling. For coordinates well beyond the cooled area, the induced stresses are negligible.

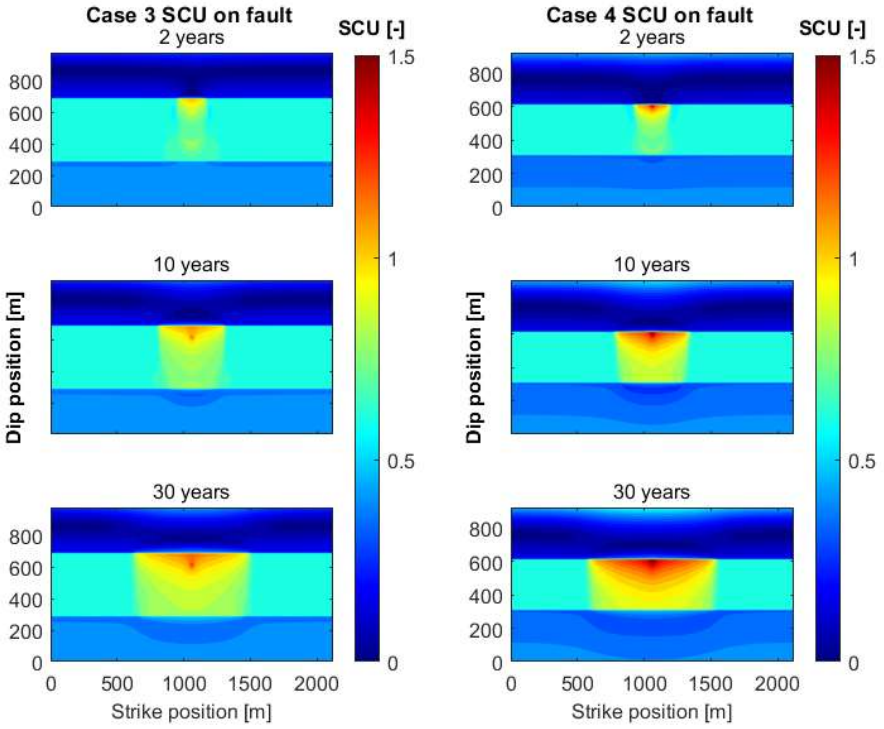

Figure 44 Shear Capacity on the predefined fault for the bases cases of Case 3 and Case 4

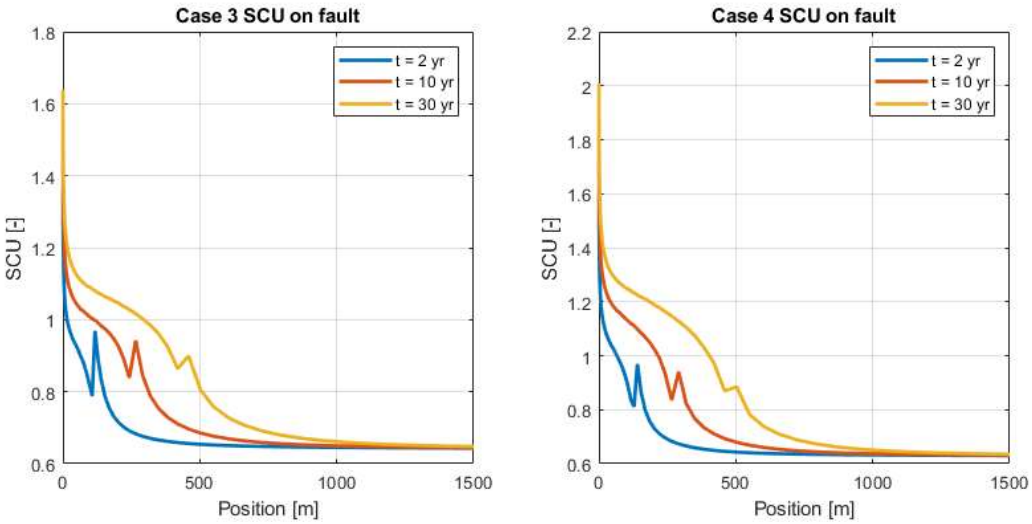

Figure 45 Shear capacity on horizontal line at 90% o the aquifer thickness in the direction of the fault, for Case 3 and Case 4

4.1.3.4 Cases 3 and 4 – stochastic analysis

The results of a stochastic analysis for Case 3 and 4 are presented in Figure 46, showing the probability of fault reactivation with distance from the injection well. The probability for fault reactivation is higher than for Case 1; again, with Case 4 having slightly higher probability for fault reactivation than Case 3. Specific field cases require specific modelling; however, we see the two issues identified earlier: the effect of position of a fault with regard to the cooled volume, and the effect of having a fault very close to the injection well or even intersecting it.

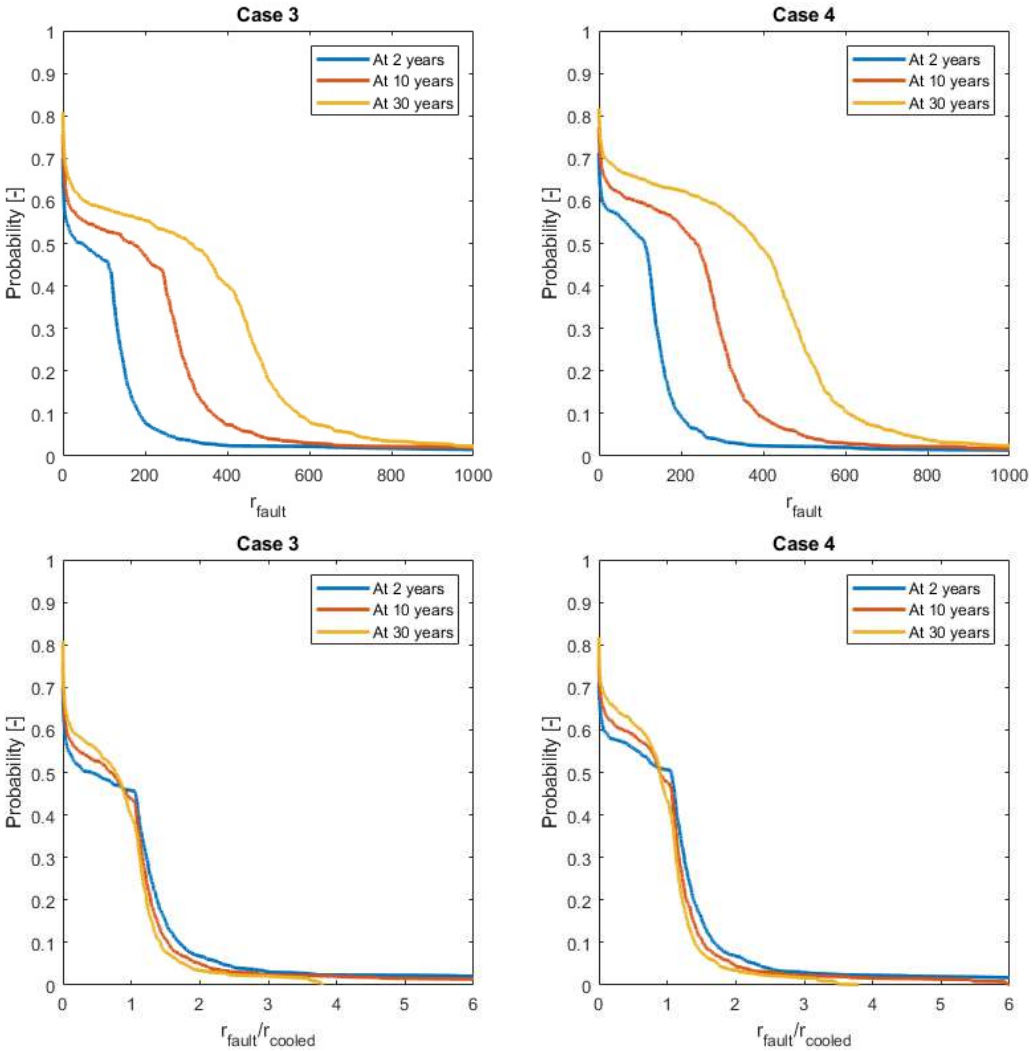

Figure 46 Results of the stochastic analysis for the seismicity measures along a horizontal line in the aquifer at 90% of the thickness, of Cases 3 and 4: Probability that a fault at that distance is reactivated

4.2 Stress changes and fault reactivation – Elastoplastic reservoir

In the SRIMA approach, as well as in many other geomechanical modelling studies, linear elastic behaviour is assumed for the reservoir and the caprock. However, from experiments it is known that rocks experience permanent deformation upon loading. This inelastic deformation is expected to play a bigger role for the poorly consolidated, porous sandstones of the Breda Formation and other targets in the North Sea Group (Section 3.12). The question is how this affects the stress build-up in the reservoir and caprock, and what this means for fault reactivation and seismicity. In this section explorative models are run to evaluate the effect of elastoplasticity on stress changes.

4.2.1 Elastoplasticity and the Modified Cam Clay model

Plastic (i.e., irrecoverable or inelastic) deformation will play an important role in addition to elastic deformation, given the weakly consolidated nature of the North Sea Supergroup. This

may impact the stress changes in the reservoir and on faults. Elastic-plastic behaviour in soils and weakly consolidated sediments is a well-studied field in geo-engineering through the concept of critical state soil mechanics(Atkinson, 2017; Wood, 1990). In short, critical state mechanics provides a framework unifying changes in effective stresses and plastic volumetric strain. Critical state mechanics comes into effect once a material is yielding, i.e., is not deforming purely elastically anymore. The 'critical state' refers to a particular combination of effective stresses (the critical state line) where the plastic volumetric strain is zero, and only plastic shear strain exists. A micromechanical process responsible for the plastic volumetric strain is not explicitly adopted but given the origin of the theory from loose soil behaviour, it is implicitly assumed that grain rearrangement leading to pore space reduction is the driving process. This process is assumed to act at all stress states below the critical state line (i.e., at combinations of higher mean effective stress and lower shear stress w.r.t. the critical state line). Better consolidated sediments may have other micromechanical processes responsible for plastic volumetric strain. Nonetheless, critical state mechanics seems to capture the empirical elastic-plastic behaviour of porous consolidated rock quite well (Cassiani et al., 2017; Nguyen et al., 2014).

The Modified Cam-Clay model is such a critical state model (Figure 47). It is a standard material model in DIANA FEA, described under the Egg Cam Clay model (DIANA Manual v10.8).

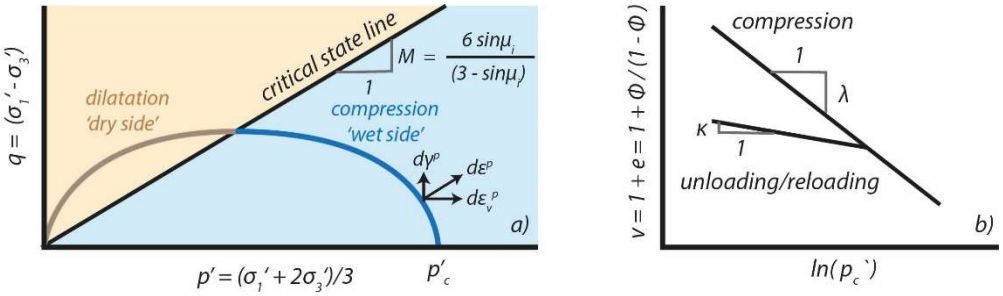

Figure 47 Schematic of the Modified Cam Clay model. A) plastic yield surface plotted in a p' – q plot (mean stress versus equivalent deviatoric stress) . B) elastic and plastic hardening components as a function of the preconsolidation stress p_c' – i.e. the largest mean stress a sample or element has experienced so far.

The Modified Cam Clay model depends on the effective mean stress p'

$$p' = \frac{1}{3}(\sigma_1' + \sigma_2' + \sigma_3') \quad 14$$

and the equivalent deviatoric stress q

$$q = \sqrt{3J_2} = \sqrt{\frac{1}{3}((\sigma_1 - \sigma_2)^2 + (\sigma_2 - \sigma_3)^2 + (\sigma_3 - \sigma_1)^2} \quad 15$$

The equation for the critical state line (CSL) is given by

$$q = Mp' \quad 16$$

Where the slope M can be defined in terms of the internal friction μ_i

$$M = \frac{6\sin\mu_i}{(3-\sin\mu_i)} \quad 17$$

The Modified Cam Clay model contains both an elastic and a plastic component. The total volumetric strain is partitioned in an elastic part and a plastic part. Both elasticity and plasticity depend non-linearly on the mean stress. Elastic hardening is formulated as

$$K_t = \frac{dp'}{d\Delta\epsilon_v} = \frac{1+e}{\kappa}(p' + \Delta p) \quad 18$$

where K is the bulk modulus, and e is the void ratio (= pore volume / solid volume). The bulk modulus is thus primarily a function of volumetric strain (changes in void rate e) and mean effective stress. In DIANA another parameters Δp have been added which can shift the yield surface so that at p'= 0 the material has some residual strength. This is amongst others useful for numerical convergence, or to scale the bulk modulus.

Plastic deformation is described by the plastic yield surface or yield cap, which is an elliptical surface given by

$$q^2 + M^2\, p'(p' - p_c') = 0 \qquad 19$$

where p_c' is the preconsolidation stress – i.e. the maximum effective mean stress the sample or element has experienced so far. Within the yield surface, only elastic behaviour (along the non-linear elastic hardening path as described in Eq. 18 occurs). When the stress state is at the yield surface, plastic hardening occurs. The preconsolidation stress changes for a change in plastic volumetric strain $\Delta\varepsilon_v^p$ as

$$p_c' = p_{c0}' \exp\left(-\frac{1+e_0}{\lambda-\kappa}\Delta\varepsilon_v^p\right) \qquad 20$$

In DIANA the initial preconsolidation stress can be determined automatically from the initialization stresses, or a fixed initial value can be prescribed explicitly.

4.2.2 Modeling elastoplasticity in DIANA Finite Element Analysis

DIANA Finite Element Analysis v10.8 was used to compute stress changes resulting from injection into an elastoplastic reservoir. An axisymmetric model space centered around an injection well was assumed, with the same reservoir geometry as that used for the linear elastic scenarios. The model width was 2500 m and the total model height was 2800 m. The SRIMA Case 2 was taken as an example, where the reservoir has a thickness of 100 m (Table 9, Figure 48).

The pressure and temperature changes were computed in SRIMA and exported to DIANA (i.e. establishing a one-way coupling from the pressures and temperatures to the stress changes and deformation).

The stress changes due to cooling were then evaluated in a phased analysis:

- 1) Initialization of stresses. The initialization of vertical stress was based on the weight of the formations and gravity, and the horizontal stress was applied according to the K_0 ratio.
- 2) Time steps with prescribed PT profile from SRIMA.

Both linear elastic (analogous to SRIMA) and elastoplastic MCC reservoir behaviour was explored. In both cases, the model was initialized with the MCC model, to establish the same state of stress at the start of cooling. For the elastic scenario, the material model was switched to linear elastic in the second phase.

Table 10 Additional input for the simulations with an elastoplastic reservoir. Input not specified in this table was the same as in Table 9, Case 2.

Parameter	Unit	Symbol	Value
Elastic hardening parameter	-	κ	0.003
Plastic hardening parameter	-	Λ	0.0055
Preconsolidation stress	MPa	P_c'	Automatic
Pressure shift	MPa	p_{tel}	0.1

Slope of the critical state line	-	M	1.2

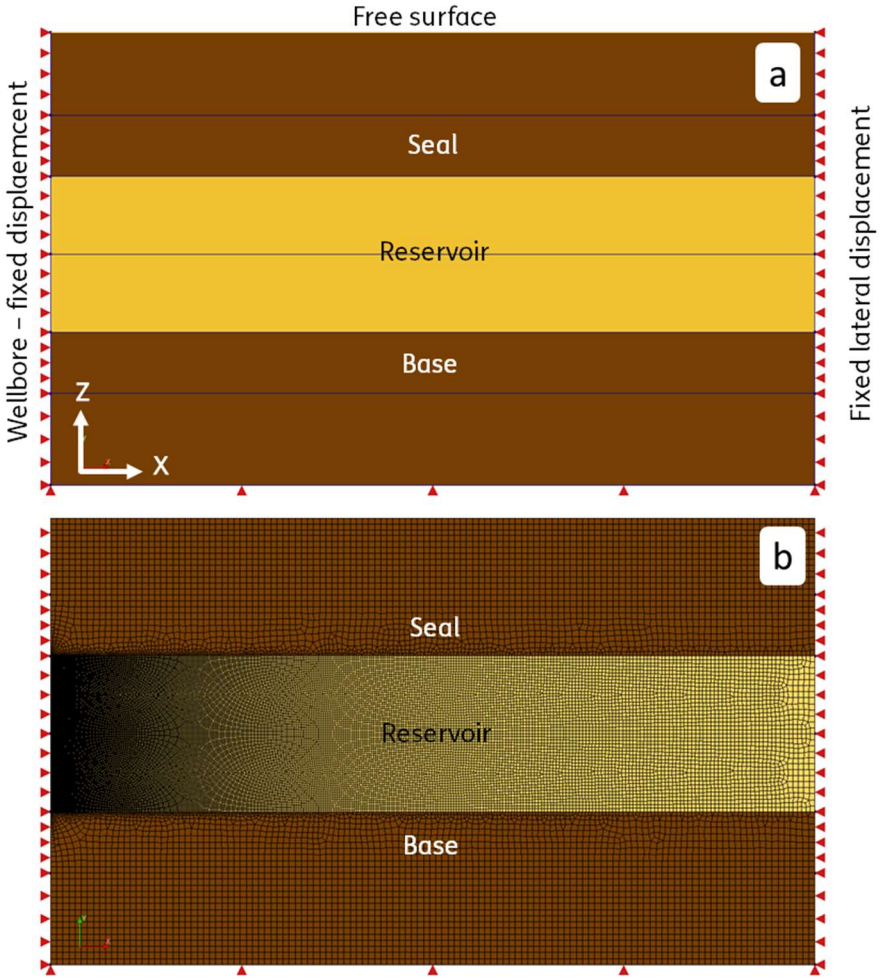

Figure 48 Model geometry used in the DIANA Finite Element Analysis, cropped around the reservoir formation. A) model geometry, including boundary conditions, b) mesh, showing refinement in the reservoir near the injection well. The central line in the reservoir is used for the observation points. The total model width is 2500 and the total model height 2800 m.

4.2.3 Setting the elastic hardening parameter

The elastic component of the Modified Cam Clay model is described by non-linear elastic hardening (Equation 18). The elastic volumetric strain evolves non-linearly with the mean stress, with rates of change depending on the elastic hardening parameter κ (Figure 49). The tangential bulk modulus (i.e. the slope of the ε_v^e evolution with mean stress p') evolves linearly with mean stress p'. The parameter κ can be used to tune the elastic behaviour such that the bulk modulus has the expected value at the depth of interest. E.g. at the mean reservoir depth of 725 meter, the mean effective stress p' is 4.3 MPa. For a κ of 0.001 and a p_{tel} of 0.1 MPa, this translates to a tangential bulk modulus of 6.8 GPa, and for a κ of 0.002, a K_t of 3.4 GPa, and for a κ of 0.003, a K_t of 2.2 GPa. For a Poisson ratio of 0.35, this translates to Young's moduli of 6.1 and 3.1 GPa, and 2.1 GPa. The range of Youngs moduli chosen in SRIMA (Table) varies between 0.2 and 4 GPa, with a default of 2 GPa.. A κ in the order of 0.003 would thus be expected to yield such a modulus. Here we choose 0.003, which is within the range proposed in the literature review for sands (Table 7, Table 8).

Note from Figure 49 that the adopted κ will have a very large impact on the bulk modulus and hence on Young's modulus, and hence on the thermo-elastic response of the medium.

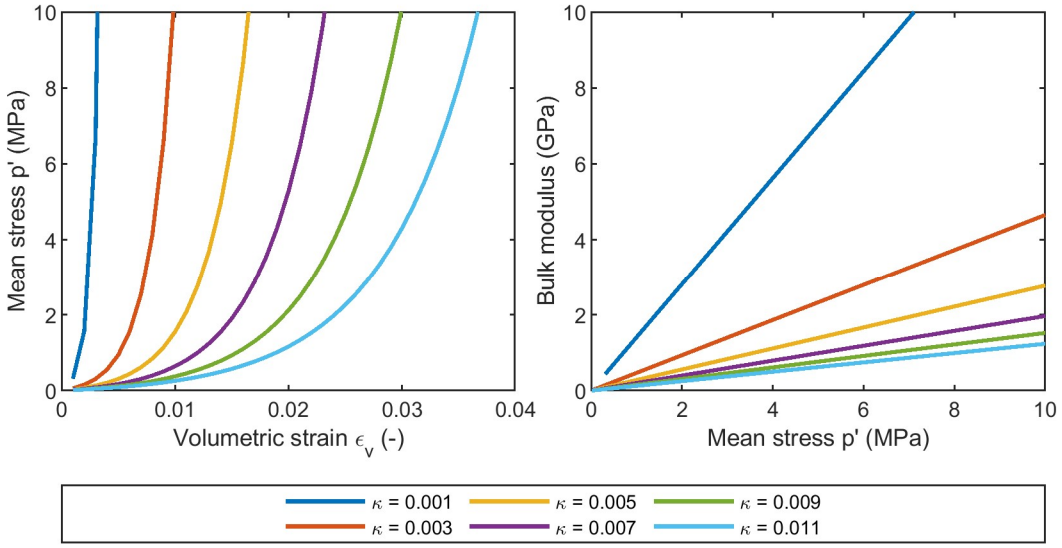

Figure 49 Elastic hardening in the Modified Cam Clay model. Left) elastic volumetric strain against effective mean stress p' for different elastic hardening parameters κ. Right) bulk modulus against mean effective stress for different elastic hardening parameters κ.

4.2.4 Stress and strain for linear elastic model

Before comparing the results with an elastoplastic model, first the stress-strain evolution as a function of position in the reservoir and time is presented in more detail for a linear elastic reservoir. In essence, this is the same as in the SRIMA simulations, but here we zoom in to local points in the reservoir instead of considering only the fault stresses or stresses along the reservoir center, to better understand the effect of elastoplastic reservoir behaviour on the reservoir stressing and deformation.

Over time the radius of the cooled rock volume increases i.e. for the current scenario, the cold front has reached 430 m after 30 years of cooling. Hence, dependent on the position of a point in the reservoir, that point may experience cooling or not. For points within the reservoir various phases in time are identified:

- Phase 1: Point of interest lies outside the cold front. Near the well, the point of interest may already experience a pressure increase.
- Phase 2: Cold front reaches the point of interest.
- Phase 3: Cold front has passed the point of interest.

These three phases are related to differences in stress-strain evolution. In Figure 50 the stresses and strains during the first year of injection are plotted at 50 m from the injection well. During the initial phase (0 - 0.2 years), before the cold front reached the observation point, pressure and temperature changes are very limited or zero (Figure 50a). However, the stress changes at the observation point are not zero, as poro- and thermo-elastic stress changes occur outside the cooled volume (sometimes called stress arching). This is reflected in a decrease in total horizontal stress and an increase in the total vertical stress (Figure 50b), a negative horizontal strain (more tensile), and an increase in both p' and q. This is due to the contraction of the cooled rock adjacent to the observation point. As the cold front reaches the observation point at 0.2 years (Figure 50a), the vertical stress decreases further but the

total horizontal stress only decreases a bit. After the cold front has passed at ~ 0.5 years the vertical stress gradually starts to increase again and the horizontal stress levels off. This is better visible at longer operation times (Figure 51), where it is observed that the vertical stress increases gradually close to the initial value. The horizontal strain also reduces throughout Phase 3, approaching uniaxial strain conditions at the end of injection. Over time a vertical strain of 5 x 10^{-4} develops, which would translate to a reservoir compaction of 0.05 m. Similarly, in P-Q space the mean effective stress p' levels off, but q increases after the cold front has passed (Figure 51c).

Note that these observations hold within the reservoir; in the caprock and base seal different stress and strain responses are expected.

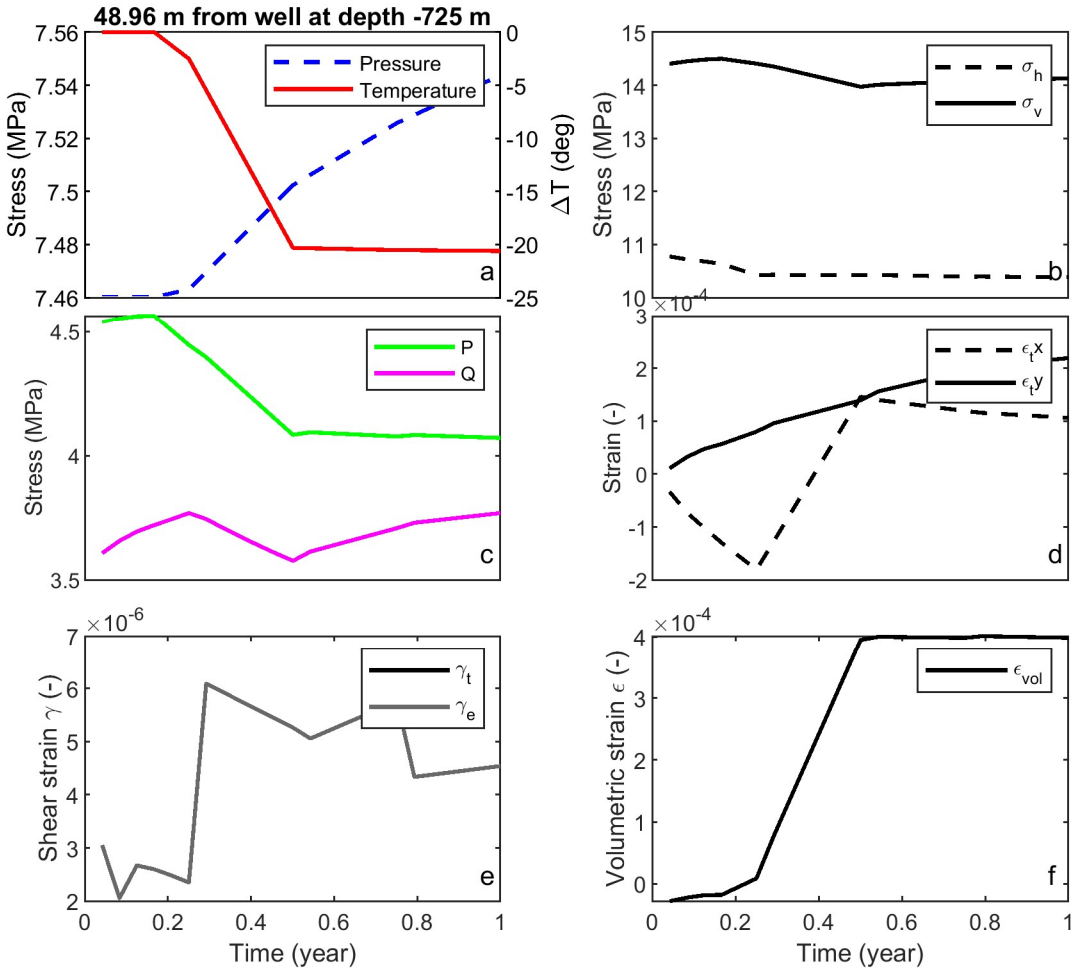

Figure 50 Stresses and strains for an elastic reservoir. Results are shown at 50 m from the well in the middle of the reservoir at 725 m depth, for the 1st year of injection. The cold front passes at 0.2 years of injection. A) pressure and temperature. B) total horizontal (dashed) and vertical stress, c) mean effective stress p' (green) and equivalent deviatoric stress q, d) horizontal (dashed) and vertical (solid) strain, e) shear strain, f) volumetric strain. NB the jagged features in e are due to the numerical output resolution and small strains.

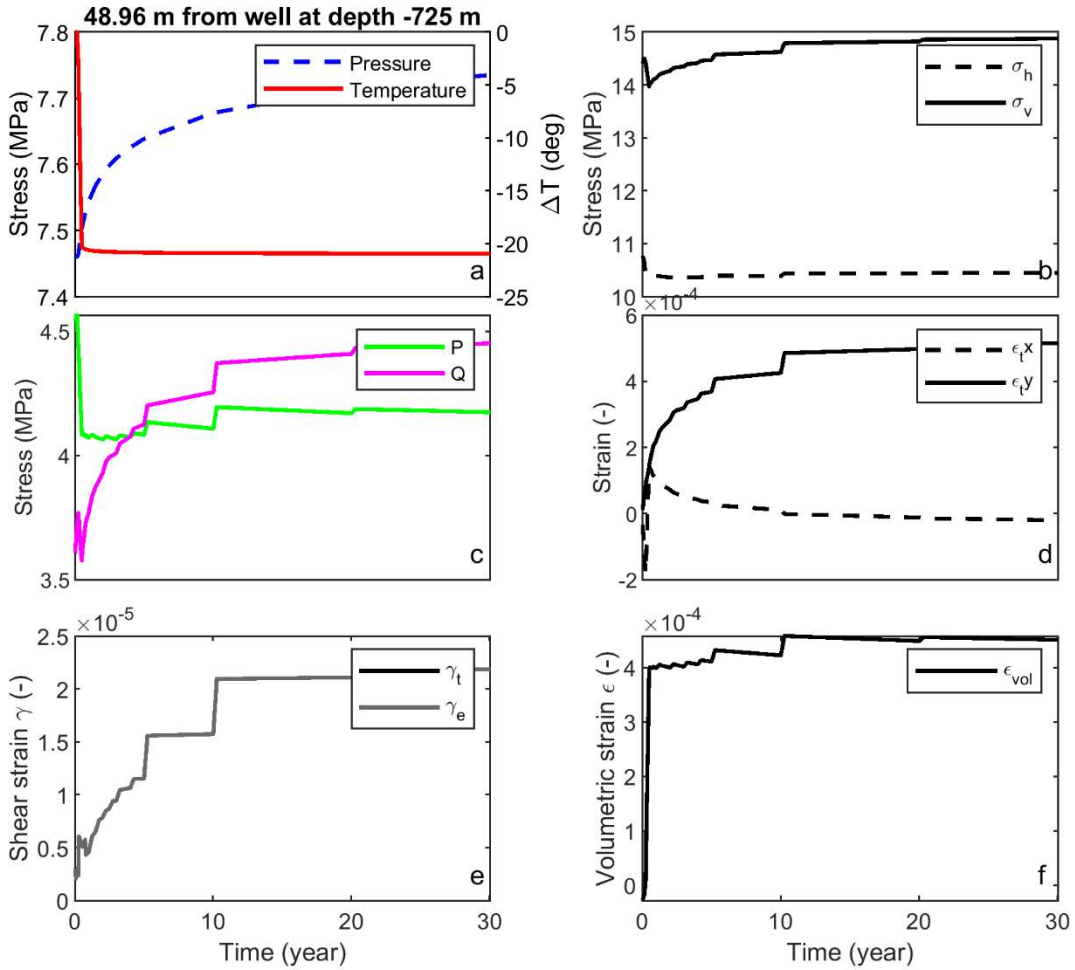

Figure 51 Stresses and strains for an elastic reservoir. Results are shown at 50 m from the well in the middle of the reservoir at 725 m depth (Obs50), for the 30 years of injection A) pressure and temperature. B) total horizontal (dashed) and vertical stress, c) mean effective stress p' (green) and equivalent deviatoric stress q, d) horizontal (dashed) and vertical (solid) strain, e) shear strain, f) volumetric strain. NB the jagged steps in the figures are due to the stepwise PT profile imposed from SRIMA.

To better illustrate the evolution of the stress invariants and how these vary in the reservoir, the stress paths for a number of observation points at the reservoir center depth are plotted in p'-q space (Figure 52). For reference, the critical state line as for the elastoplastic model is plotted, but it has no bearing on the elastic response. The points close to the injection well (25, 50 m) show a small increase in q, corresponding to Phase 1 in (see also Figure 51b, 0 – 0.2 years). Then, during the passage of the cold front (Phase 2) a decrease in p' of ~ 0.5 MPa is observed. Further away from the injection well the Phase 1 response (mainly an increase in q') is stronger, and the Phase 2 response (the decrease in p') becomes larger. Phase 3 is reflected by the further increase of q. For the points close to the edge of the cold front (400 m), the Phase 3 response becomes less, or disappears (450 m) leaving only a Phase 1 and 2 responses. For points at a larger distance from the cold front (e.g. 700 m, versus the cold f), only a Phase 1 response is observed (increase in q).

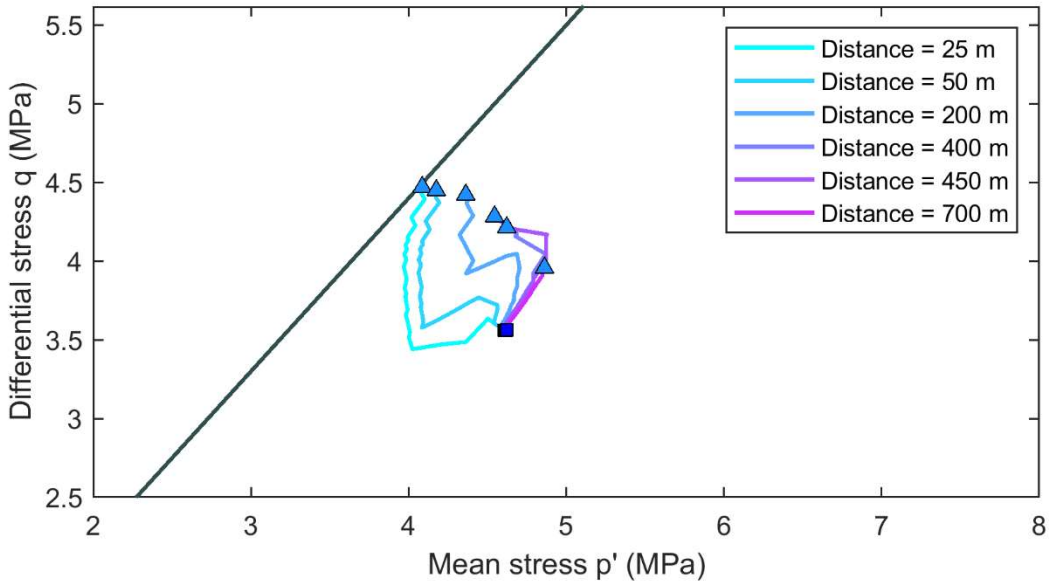

Figure 52 Stress path in p'-q space for an elastic reservoir, at multiple distances from the injection well, at the reservoir center depth (725 m). The square indicates the initial stress of stress, the triangles the final state of stress after 30 years. For reference and comparison with the elastoplastic stresses in Figure 55, the critical state line with M = 1.2 is plotted. At the end of cooling, the cold front lies at 430 m from the injection well.

4.2.5 Stress and strain evolution for an elastoplastic reservoir

For the same scenario the elastoplastic response was computed. The 1st year response at 50 m showed some similarities with that of the elastic reservoir but also some minor differences (Figure 53). In Phase 1 (0 – 0.2 years) there are for example some differences in the stresses which may be due to the initialization. The differences become however more pronounced with injection time (Figure 54). The equivalent deviatoric stress increase for the elastoplastic case is much less than for the elastic case (Figure 54c). This is mainly the result of the horizontal stress evolution, which, after an initial reduction in Phase 1 and 2, increases again as the cold front expands (Figure 54c). A substantial part of the deformation is plastic, e.g. >60% of the vertical strain is plastic strain.

In p'-q space the initial Phase 1 and 2 responses close to the injection well (25, 50 m) are similar to the elastic case, although the Phase 1 response (the initial increase in q as the cold front approaches) is less than for the elastic reservoir. Further away from the well, for the elastoplastic case the mean stress *p'* increases, stabilizing the state of stress, whilst for the elastic case *q* increased. The biggest difference in the stress paths was observed during Phase 3, where for the elastic case *q* keeps increasing but for the elastoplastic case *q* initially increases (but less so than for the elastic case) but then *p'* increases, bringing the state of stress further away from the critical state line. So initially the stress path for the elastoplastic reservoir is destabilizing, but in the later phases, as the cold front expands, it stabilizes. Compared to a linear elastic reservoir, an elastoplastic reservoir results in a more stable stress state at the end of cooling. This also holds for the reactivation of faults. When plotted in Mohr space for a fault dipping 60 degrees, the stress path for the elastic scenario is more unstable then for the elastoplastic reservoir (Figure 56).

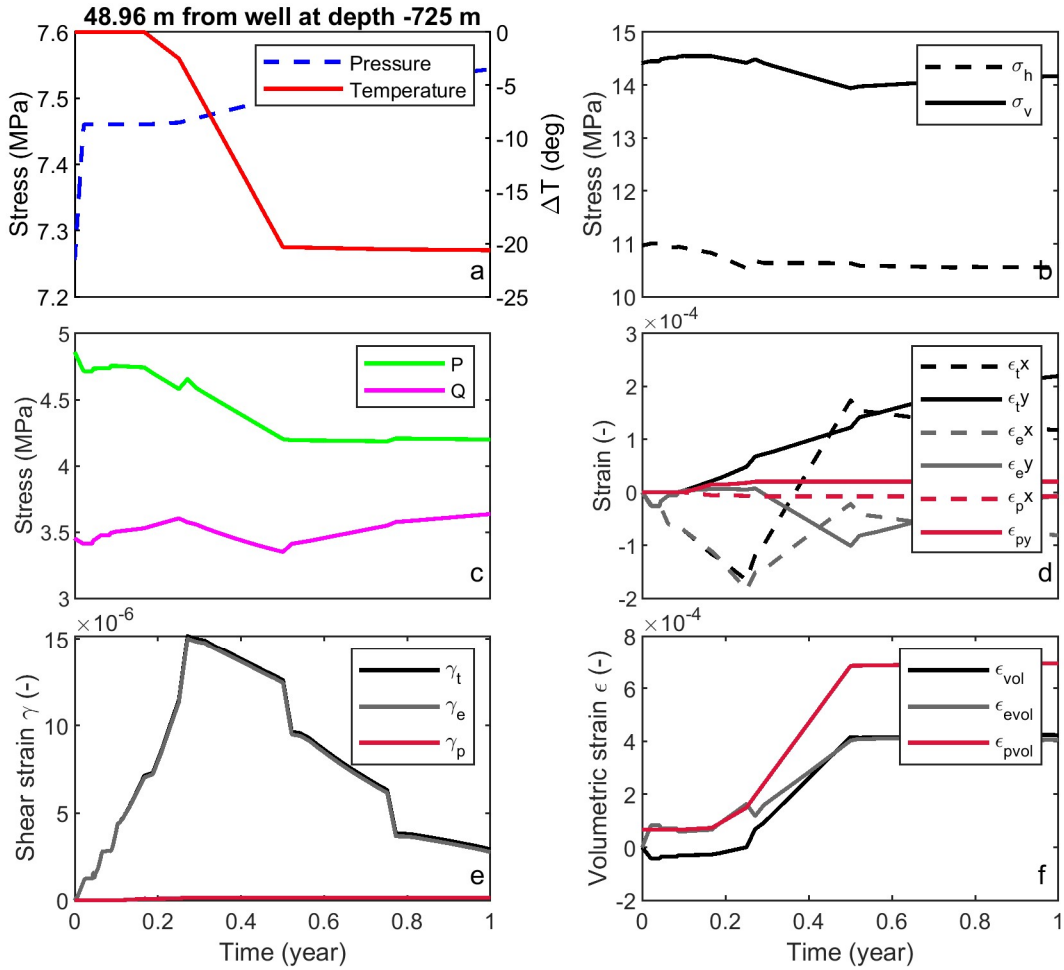

Figure 53 Stresses and strains for an elastoplastic reservoir. Results are shown at 50 m from the well in the middle of the reservoir at 725 m depth (Obs50), for the 1st year of injection. A) pressure and temperature. B) total horizontal (dashed) and vertical stress, c) mean effective stress p' (green) and equivalent deviatoric stress q, d) horizontal (dashed) and vertical (solid) strain, e) shear strain, f) volumetric strain. NB the step changes in the figures are due to the discrete application of the PT field from SRIMA.

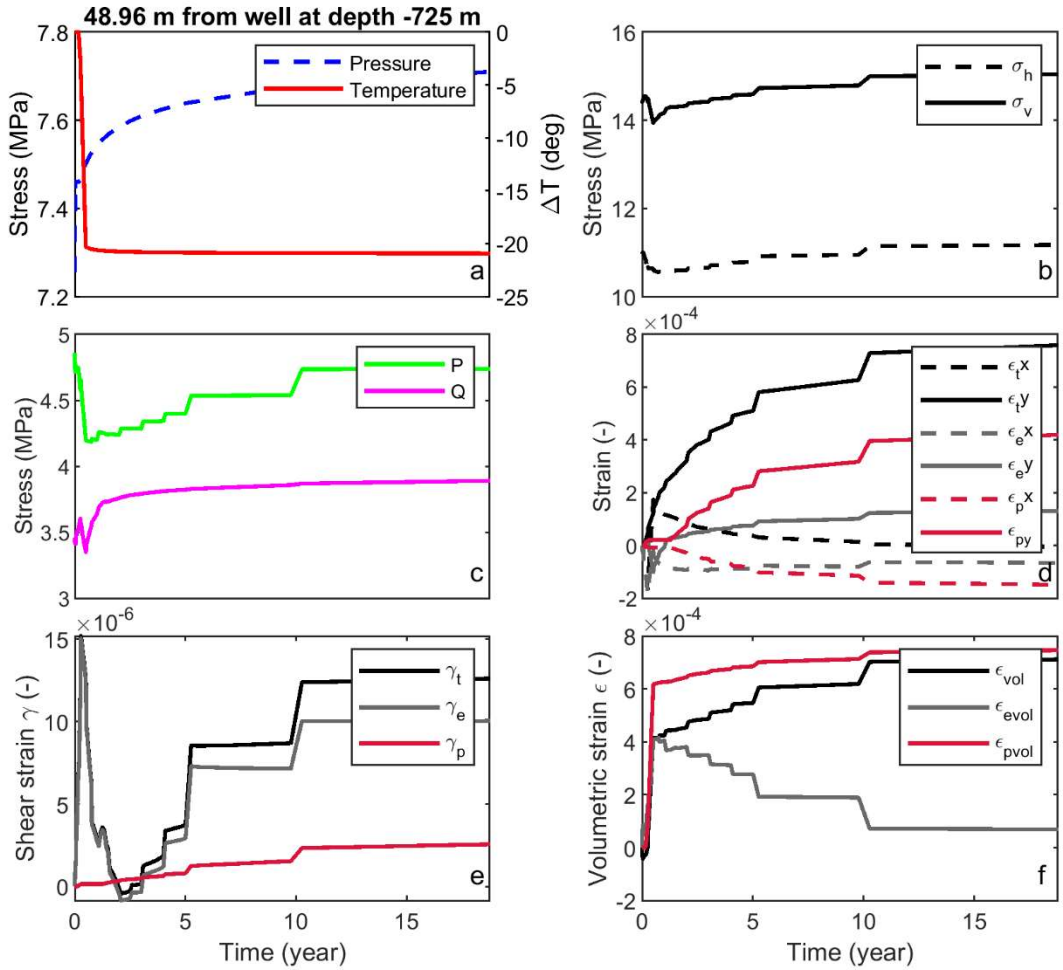

Figure 54 Stresses and strains for an elastoplastic reservoir. Results are shown at 50 m from the well in the middle of the reservoir at 725 m depth (Obs50), for the 30 years of injection A) pressure and temperature. B) total horizontal (dashed) and vertical stress, c) mean effective stress p' (green) and equivalent deviatoric stress q, d) horizontal (dashed) and vertical (solid) strain, e) shear strain, f) volumetric strain. NB the jagged steps in the figures are due to the stepwise PT profile imposed from SRIMA at discrete timesteps.

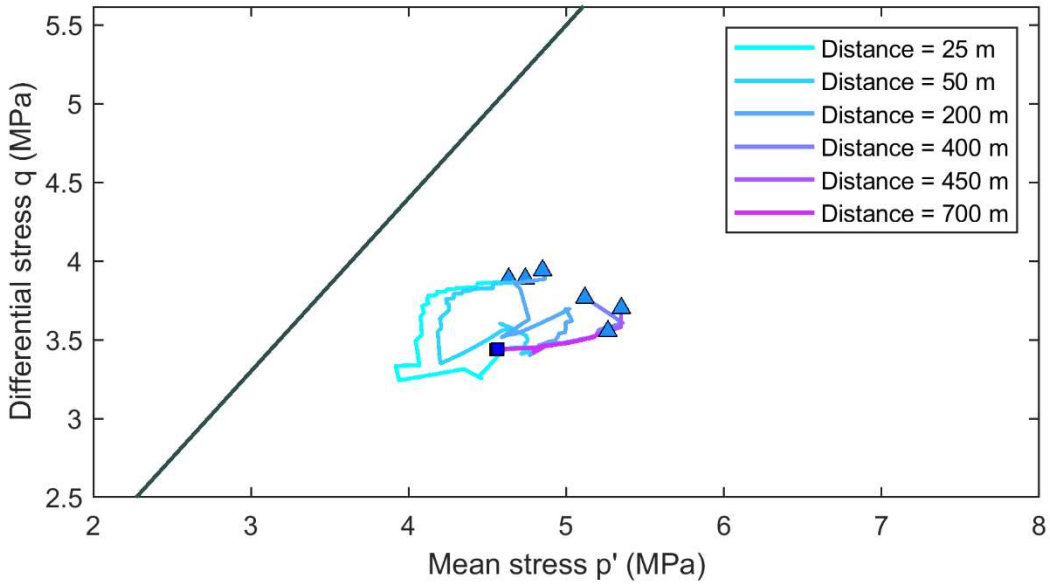

Figure 55 Stress path in p'-q space at multiple distances from the injection well for an elastoplastic reservoir, at the reservoir centre depth (725 m). The square indicates the initial stress of stress, the triangles the final state of stress. For reference, the critical state line with M = 1.2 is plotted. At the end of cooling, the cold front lies at 430 m from the injection well.

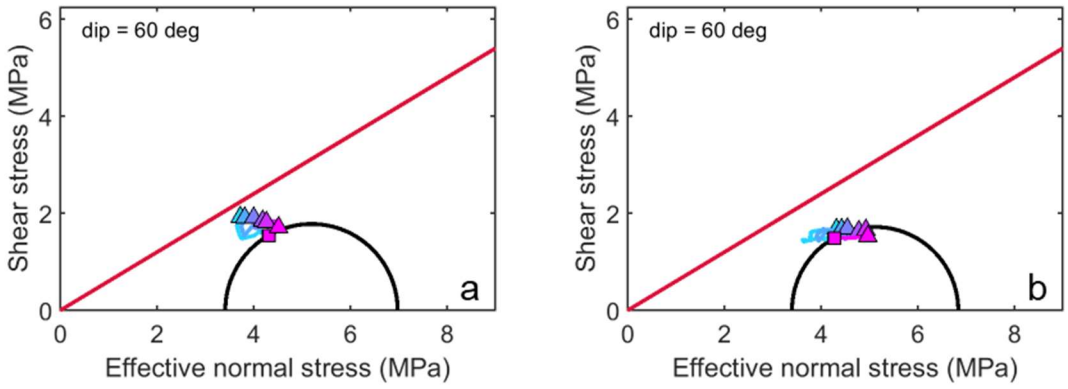

Figure 56 Stress paths in Mohr space for an elastic (a) and elastoplastic (b) reservoir. Different colors indicate different positions in the reservoir, see Figure 55 for legend.

4.2.6 Sensitivity to elastic hardening parameter

Given the expected sensitivity to the elastic hardening parameter κ, simulations were ran with a κ of 0.001. This results in a bulk modulus more than twice that in the case of κ = 0.003. An equivalent Young's modulus of 6.7 GPa was used for the elastic simulation, which is equal to the Young's modulus of the elastic component of the MCC model. For the elastic case (i.e. the equivalent to SRIMA), the equivalent deviatoric stress increase was larger than for the simulations with a lower elastic modulus, as is expected. Stresses were above the shear failure line (Figure 56), and fault reactivation could be expected (Figure 58). Note that shear failure in itself is not modelled for the linear elastic medium, which is why the modelled stresses can exceed the failure line (e.g. as in Figure 57a). When the expected shear failure occurs, shear stresses would be locally reduced.

The difference of the elastoplastic scenario with the elastic one was larger than for the scenario with κ = 0.003. The stress paths were more unstable than those in Figure 55, but did not reach failure in most cases. An exception was points close to the well where shear failure was reached. Note that in the case of MCC, shear failure is actually modelled, so here the stress state cannot exceed the shear strength of the reservoir rock. In terms of fault reactivation, the MCC model stress paths were stabilizing (Figure 56).

These simulations give a first order insight into the differences between elastic reservoir behaviour and elastoplastic reservoir behaviour. The results show that an elastoplastic reservoir leads to more stable stress during cooling. The results also show that the direction and evolution of the stress paths is markedly different between both scenarios.

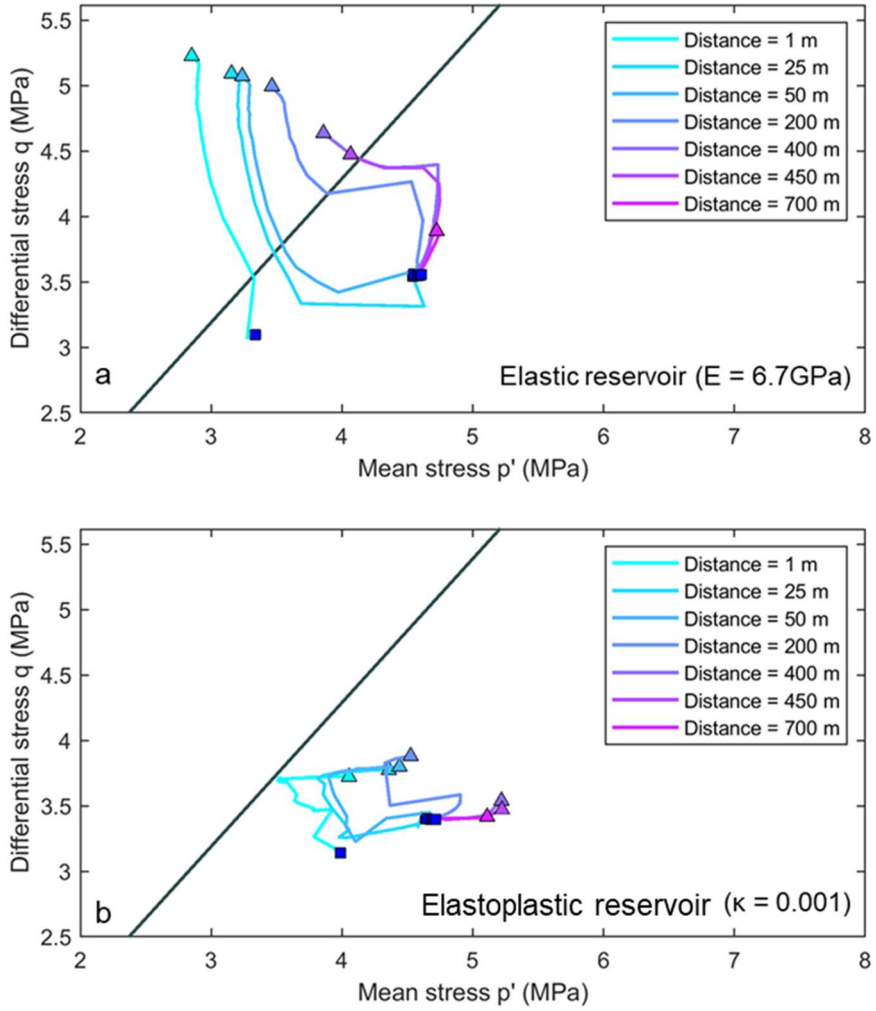

Figure 57 Stress path in p'-q space at multiple distances from the injection well for an elastoplastic reservoir, at the reservoir centre depth (725 m), for a κ of 0.001. Note that figure (a) represents an elastic reservoir, while (b) represents the elastoplastic scenario. The square indicates the initial stress of stress, the triangles the final state of stress. For reference, the critical state line with M = 1.2 is plotted. At the end of cooling, the cold front lies at 430 m from the injection well.

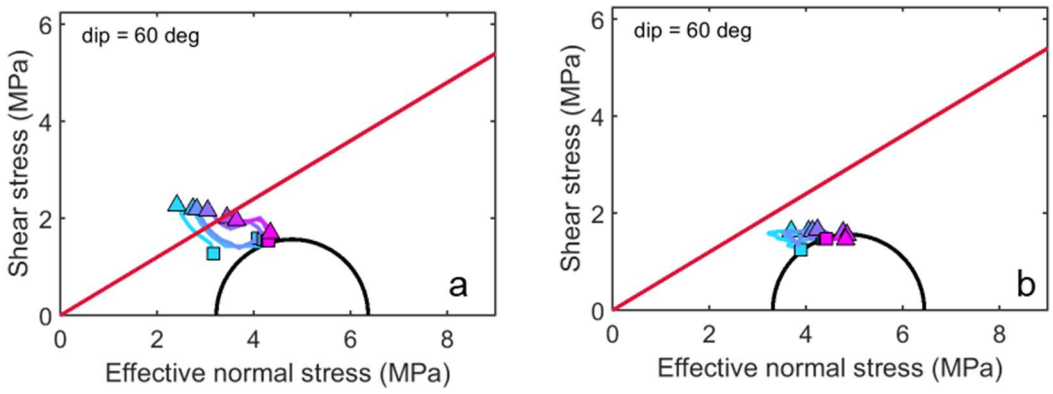

Figure 58 Stress paths in Mohr space for a κ of 0.001, for an elastic (a) and elastoplastic (b) reservoir. Different colors indicate different positions in the reservoir, see Figure 55 for legend.

5 Discussion

In the following, we discuss the main findings of the study. First, we discuss the applicability of SRIMA to geothermal operations in poorly consolidated reservoirs such as the North Sea Supergroup formations. Then, we discuss how fault reactivation potential changes when considering plasticity in addition to elastic behaviour. Since fault reactivation is not equal to seismicity, the expected seismogenic potential is discussed on the basis of a literature screening of friction parameters and observed seismicity. We then consider the implications for seismic hazard assessment in the RVG. Finally, we look at other considerations and discuss the gaps in data identified during this study, followed by recommendations to reduce these gaps.

5.1 Applicability of SRIMA to model geothermal projects in the North Sea Group

SRIMA has been developed for the quick evaluation of the potential of fault reactivation and induced seismicity due to the injection of cold water in a geothermal well. So far, it has been used mainly to model deeper, consolidated porous reservoirs. In this study it was applied to the shallow North Sea Group reservoirs, but clearly, the semi-analytic nature of the tool comes with limitations, and it is important to assess the effect of those on the outcome of the study.

The major simplifications of SRIMA are the geometry of the cooled and pressurized zones and the material behaviour. Cooling and pressurization are taken radially symmetric and are independent from the vertical position for the values in the injection zone, and subject to the properties of three distinct zones only: reservoir (or aquifer), seal, and base. The North Sea Supergroup reservoirs are however thick (300 – 500 m), contain a mix of sandy and clayey layers, and do not always have a clearly defined seal-reservoir-base geometry (Section 3.3). In addition, taking into account density differences between the reservoir fluids and the injected fluids may lead to different shapes of the cold front. Therefore, the pressures and temperature changes computed in SRIMA may not be accurate. A comparison with numerical calculations, for instance with a reservoir simulator, is recommended.

The large thickness of the modelled reservoir in the North Sea Groups poses another complication. SRIMA imposes a constant temperature field as a function of depth. For thin, deep reservoirs this may be a justifiable assumption, but for the thick North Sea Group reservoir this cannot be ignored. The temperature increase over the reservoir interval with depth may be significant, and the amount of cooling will thus vary over the thickness of the cooled zone. Specifically, fault reactivation may start at the bottom of the cooled zone, where the cooling is most severe – rather than from the top of the cooled zone as in, e.g. Figure 36. On the other hand, the stresses, and hence the absolute amount of allowable stress change before reactivation occurs increase too. An assessment of the combined effect of incorporating stress gradients and a temperature gradient on fault reactivation is currently not possible in SRIMA, and an implementation of new functionality to facilitate such calculations was beyond the scope of the current project. It is however recommended to extend SRIMA to incorporate this effect or use more advanced reservoir simulators to model cooling. The conclusions on sensitivity of reactivation to the input parameters, and to the position of the fault with regard to the cold front, however, remain valid.

The radial geometry precludes the application of SRIMA to reservoirs with anisotropic permeability or to isolated high-permeability streaks or fracture zones. This is, however, not the case in the present investigation. In reality the cooling may be more heterogeneous.

The SRIMA modeling, which assumed linear elastic behavior, showed that with certain material parameter values, the stress on the fault could surpass the strength of the fault. However, the inclusion of elastoplastic reservoir behaviour (Section 4.2) led to a different, more stable stress path with respect to an elastic reservoir. Hence, the SRIMA tool, which assumes linear elasticity, has only limited use for the poorly consolidated formations of the North Sea Supergroup. The elastoplastic response is highly non-linear, so adopting for example a correction factor in the SRIMA calculations may not be easy. We note that this study provided only a first order insight into the effects of elastoplasticity on the stress development during cooling; it is recommended to further explore elastoplasticity under a bandwidth of parameters and reservoir settings, all of which may have substantial uncertainties. And, as with any numerical tool, input from experiments on representative sample material and validation against field observations are recommended to build confidence in the model approach.

Shear failure can occur in the simulations when using an elastoplastic material model. Even though the stress path for the elastoplastic reservoir remained further away from failure than for an elastic reservoir, shear failure did occur in a number of scenarios. This was mainly during the initial phases of injection when the stress path was most unstable, or for low elastic hardening coefficients. Shear failure may result in, amongst others, plastic flow and the development of shear bands in the reservoir. Even though this is likely not a seismic process, shear failure can result in increased sand production and is therefore better avoided. Here, the elastoplasticity models can aid in defining the optimal operational windows for geothermal production.

5.2 Will faults in shallow unconsolidated sediments slip seismically?

Fault reactivation does not equate to seismicity, as detailed in Section 1.5. The primary scope of this report was the potential to establish fault reactivation, which, based on the SRIMA simulations in 4.1, could occur under certain conditions and material parameters. Here, we shortly discuss if this would lead to seismicity in the shallow unconsolidated sediments.

It is generally accepted that the upper few km's of the crust, especially when covered by (partially consolidated) sediments, are not seismogenic (see for instance the seminal work by (Scholz, 1988)). The pool of relevant literature on observed nucleation and on frictional properties in unconsolidated sediments is therefore limited. The analysis of the source locations of tectonic earthquakes (see Section 2) suggests that earthquake nucleation does not occur in the RVG North Sea group sediments. We note here the caveat that the vertical uncertainty was very large due to sparse network coverage, so that a handfull of events cannot be ruled out to have nucleated in the North Sea group. However, this likely results from the localization algorithms not being able to constrain a depth at all. Paleoseismic analysis did show that rupture propagation (i.e. the growth of the slipping zone after an earthquake has nucleated) did occur in the shallow North Sea Group sediments in the past (at different loading condition than the current one).

Work on frictional properties in sediments consists mostly of studies on subduction zone sediments. The overall tendency is that earthquakes cannot nucleate in these shallow sediments, but that these sediments can accommodate sufficiently large ruptures from

deeper in the subduction zone – similar to the bounding faults of the RVG (see Section 2). Intrinsic fault frictional behaviour that determines stable or unstable slip is often described in the framework of rate-and-state friction with the parameter (a-b), where (a-b)>0 indicates velocity strengthening (stable slip) (Dieterich, 1979; Ruina, 1983). Where reported, the reviewed literature shows that the sediments at low velocity are velocity strengthening (Table 11) and cannot nucleate earthquakes. We suspect this will be the case to for faults in the RVG. However, this should be verified experimentally, through e.g. velocity-stepping experiments. In addition, at the small depths of the North Sea groups the size of the critical nucleation zone – i.e. the fault area that must be slipping before unstable rupture can nucleate (e.g. Rubin & Ampuero, 2005) – could be large, perhaps larger than the perturbed fault area. If that is the case, slip will also be aseismic. In a follow-up study, the critical nucleation zone can be assessed by looking at characteristic slip distance (a measured quantity in friction experiments) and the elastic moduli of the bulk.

Another mechanism for the nucleation of unstable fault slip is the development of fault cohesion through cementation, healing, compaction or diagenesis. A cohesive fault is stronger than a non-cohesive fault, but it can also break in a more brittle manner, leading to unstable slip even if the uncohesive material itself would be rate-strengthening. This has for example been explored for fault gouges for the Groningen Field (e.g. Hunfeld, 2020). Cementation and diagenesis at shallow depth is very limited, and faults in the North Sea Supergroup are likely non-cohesive. This could be analyzed or confirmed by e.g. slide-hold-slide experiments investigating healing of fault gouges.

Table 11: Frictional behaviour of unconsolidated sediments at low slip velocity from literature.

study	provenance	sediment description	mineralogy	static m	(a-b)	P^{eff} (Mpa)
(Rabinowitz et al., 2018)	Hikurangi Trench, New Zealand	calcareous mudstone	43% calcite, 20% clau, 9% qz, 15% feldspar	0.2 - 0.4	0.01	25
(Han et al.,)	Suryum Fault, South Korea	clay-rich gouge	57% clay, 33.9% qz	0.4	0.05	2
(Seyler et al., 2020)	Cascadia Trench, US	mudstone	20% qz, 35% feldspar, 45% clay	0.4 - 0.45	-	2, 5, 8
		sandstone	30% qz, 35% feldspar, 35% clay	0.67	-	2, 5, 8
(Balsamo et al., 2014)	Calabria Fault, Italy	medium-sized sands	44% qz, 29% feldspar, 18% clay, 7% calcite	0.65	velocity-strengthening	14

In summary, the nucleation potential of the RVG North Sea group sediments seems to be low, based on the nucleation depth of the observed earthquakes and on frictional properties of similar sediments measured by other studies. This however remains circumstantial evidence, and we therefore strongly recommend laboratory experiments on material from the RVG North Sea group to confirm this interpretation, in combination with field measurements, modelling and monitoring.

5.3 Implications for seismic hazard

The lower seismogenic potential estimated for the North Sea Groups in the RVG should be reflected in the seismic hazard assessment for projects in the region. However, so far, most evidence is circumstantial. Direct measurements of e.g. frictional properties or plasticity, in combination with monitoring and follow-up modelling, is recommended to guide adaptations

in the SHRA workflow, or to develop a different approach altogether – e.g. a screening where depths up to a certain level are identified as low seismic potential based on certain measurements and/or data. It would also be advisable to establish a background seismic hazard analysis relating to the natural seismicity in the region. This allows to better assess the contribution to potential induced seismic events to the overall seismic hazard.

5.4 Other considerations

The SRIMA geometry also neglects the influence of the free surface at the ground level. This is well defendable when the dimensions of the cooled and pressurized zones are small with respect to the depth at which they are located. For the shallow, thick aquifers that we have been studying here, these assumptions cause larger uncertainties. Several centimeters of compaction are expected in the cooled reservoir, which can lead to subsidence at the surface. Numerical geomechanical calculations are recommended to gain insight in the potential subsidence resulting from cooling.

5.5 Data gaps and prioritization

Here, we discuss data gaps and quality of available data based on the data inventory in Section 3. We then prioritize the data gaps, using the model results for fault reactivation as guidance.

The data inventory indicates a severe lack of data for the Breda Formation and other formations in the RVG. The number of vintage wells in the area is limited, and most wells date from the 80s of the last century – or older. Data collection on the available wells in the North Sea Supergroup interval has usually been limited and/or of poor quality, with the exception of the AST-GT-02 well which specifically targeted the Paleogene and Neogene.

The lithology of the Paleogene and Neogene succession has been described only briefly on the basis of cutting material. A comparison of lithologs of the most relevant wells shows that large differences exist in the description of the Breda Formation. This could indicate that the lithological variation within the Breda Formation is large, or that the lithologs are uncertain. Determination of the net-to-gross using a gamma ray is hampered by the presence of glauconite. The Breda Formation sediments are sometimes described as very clayey, sometimes as very sandy. An expected lithological variation in the Breda Formation sediments is supported by seismic interpretations by (Siebels et al., 2024), although this author mostly refers to lithology descriptions on www.dinoloket.nl, which are mostly based on the analysis of shallow wells.

Although petrophysical evaluations have been made for the Breda Formation in the RVG for various wells, sometimes using poor quality log data, a severe drawback is the absence of core data to calibrate the petrophysical evaluation. Therefore, the uncertainty in porosity and permeability is large.

In addition, little is known of the geomechanical properties of the Breda Formation sediments. Only elastic moduli could be obtained from the conversion from sonic well logs; however, this was obtained from the Oranjeoord well outside of the RVG. Moreover, this conversion yields a wide range of possible values, depending on which lithology-based conversion function is chosen (Section 3.7). Other geomechanical parameter value ranges were based solely on other studies on equivalent material. This resulted in a wide range of values for plastic Cam-clay parameters, frictional parameters, and thermo-elastic parameters. These wide ranges partly stem from the brief description of lithology in the RVG as addressed above, and how

these descriptions relate to the descriptions of lithology in literature sources (e.g., the plasticity parameters per lithology in Section 3.12). In summary, most geomechanical parameter value ranges presented in this report are no more than first order estimates.

The planned SCAN well that are drilled through the North Sea Groups should therefore focus on data collection over the entire Breda Formation, possibly also the under- and overlying units such as the Veldhoven and Oosterhout Formations, aiming at lithological descriptions and petrophysial and geomechanical properties. Data collection should include (multispectral) Gamma Ray, sonic, density and porosity logs, and rock core, both in the reservoir and cap rock. The lateral lithological variability of the Groote Heide and Diessen Formations is largely unknown, this can possibly be tackled by forward stratigraphic modeling, machine learning on seismic and conventional data acquisition, but this needs to be verified using actual well data. In particular, the state of stress is unknown, especially in sandy formations. It is recommended to perform stress tests. Additionally, laboratory measurements on static elastic parameters, plasticity and friction of North Sea Supergroup materials will be helpful, as currently only literature values could be used.

The stochastic approach of SRIMA gives a sensitivity of the input parameters that are important to fault reactivation (through the analysis of the probability of the maximum distance to fault reactivation) (Section 4.1.3). From this, fault reactivation is most sensitive to the horizontal stress, friction coefficient, elastic moduli, and linear thermal expansion coefficient. We propose to prioritize the uncertainty on these four parameters as follows:

- Horizontal stress: these include XLOT/mini-frac tests in the more sandy formations, in addition to those in the seal.
- Elastic moduli: A continuous record of dynamic elastic parameters is obtained when sonic V_P and V_S measurement are employed during the drilling of the planned SCAN wells, as has been done for the Oranjeoord well. These dynamic elastic parameters can be converted to static moduli given a calibration. The calibration can be obtained from laboratory loading-unloading experiments on several representative recovered samples, at the in-situ pressure conditions. Note that these experiments can be combined with those required to obtain plastic deformation parameters, such as stress cycling or creep experiments during which elastic and (visco)plastic strains can be separated.
- Friction coefficient: Straightforward static friction experiments can be obtained on fault gouges from the planned SCAN wells. As it is unlikely that faults are intentionally drilled, or gouge is recovered, representative gouge mixture can be created from recovered host rock samples. Note that these experiments can be combined with velocity-step friction experiments to also obtain the rate-and-state parameters, which is crucial to answer whether the fault material is seismogenic.
- Thermal expansion coefficient: Again, laboratory measurements are the way forward to reduce uncertainty on this parameter. A similar experimental protocol followed in (Soustelle et al., 2022) can be followed to obtain these values. To our knowledge, thermal expansion coefficients in unconsolidated sediments have not been measured yet.

6 Conclusions and recommendations

In this report a study on the fault reactivation potential of the North Sea Groups in the Roer Valley Graben was summarized. The aim of this study was to give a first-order estimate of the fault reactivation potential and seismogenic potential of the North Sea Supergroup in the RVG. The study consisted of a literature review of observed seismicity in the RVG in relation to the depths of the North Sea Supergroup, a data inventory of North Sea Supergroup properties which serves as an input deck for model simulations, model simulations of geothermal operations in RVG targets with the SRIMA tool assuming linear elastic properties in the reservoir, and a few explorative Finite Element models of the same targets to address the effects of elasto-plastic reservoir behaviour on fault reactivation. The results were discussed in the light of the model assumptions and the underlying physics of fault slip, and implications were formulated for the current Seismic Hazard and Risk Assessment for geothermal projects.

The following conclusions were drawn:

- Tectonic earthquakes have been observed in the RVG by the KNMI from the national seismic network. Earthquake nucleation seems restricted to depths well below the North Sea Supergroup. However, the vertical position uncertainty was very large (in the order of kilometers) due to sparse network coverage in the RVG. For some events, indeed, the uncertainty was too large to establish a source depth. These are currently listed as events located at 1.0 km depth in the KNMI catalog, whereas the depth is in fact unconstrained; hence, care must be taken with the published depths. Excluding these events from the catalog, none of the events was located in the North Sea Supergroup (though the uncertainty in depth sometimes overlaps with the North Sea Supergroup). Also, relocation studies near Roermond position all events (well) below the North Sea Supergroup, adding to the evidence that the seismic events nucleate primarily on faults in the underlying, stiffer formations.

- A literature review on the rate and state parameters of siliciclastic materials analogous to the North Sea Supergroup sediments suggests that, once a fault is reactivated in the shallow unconsolidated sediments, it may slip aseismically and will not lead to induced seismicity. This suspicion is in agreement with the previous conclusion but should be further supported by future research such as laboratory experiments.

- In the conservative scenario that a fault was to be located at the injection well, the SRIMA calculations, which assume a linear elastic reservoir, indicated that fault reactivation can occur in > 40-80% of model simulations. At this location, the induced stress changes are largest. However, in the more realistic scenario that the fault is located at some distance from the fault, the probability for fault reactivation decreases. Especially when the fault is located outside of the cooled reservoir volume, the probability for reactivation drops dramatically to <10-20% within 2 times the radius of the cold front, and tends to 0% further away.

- Even though cooling is less than in geothermal projects at depth, reactivation was modelled in SRIMA because the allowable stress change before failure at shallow depth is also smaller; both cooling and allowable stress window scale with depth. The most important parameters controlling occurrence and magnitude of reactivation are, besides the distance between the well and fault mentioned in the previous point, the initial horizontal stress, the slip parameters and the elastic parameters of the subsurface, Young's modulus and thermal expansion coefficient. Knowledge of these parameters helps to finetune the assessment of fault reactivation. Also the injection rate and injected volume will have a substantial effect. Note however, this is under the assumption of linear elastic behavior, which is not likely to be applicable to shallow, poorly consolidated sediments.

- The stress path in an elastoplastic reservoir is more stable than for an elastic reservoir. Hence, compared to the SRIMA simulations, a lower probability of fault reactivation is expected. We do note that shear failure of the bulk reservoir rock was also observed in the elastoplastic reservoir, in particular early in the injection time when the stress path was most destabilizing, for small elastic hardening coefficients, for thicker reservoirs, and for large amounts of cooling. This shear failure however is likely plastic flow of the reservoir rock, instead of brittle faulting.

- Even though fault reactivation was modelled does not mean that fault slip is seismic. considering the literature reviews on the frictional stability of shallow siliciclastic fault materials, the lack of diagenesis, and the observations from seismicity in the RVG. These suggest that faults in the RVG may slip aseismically (see below).

- The use of SRIMA in its current form within a seismic hazard framework is limited for shallow, poorly consolidated reservoirs. Adaptations of the tooling or development of a different screening approach is recommended.

6.1 Recommendations

Based on our study we list the following recommendations:

- Addressing data gaps identified in section 5.5 during future acquisition campaigns and/or future wells in the RVG. Based on the sensitivity analysis in SRIMA, priorities are the horizontal stress, elastic moduli, static coefficient of friction, and thermal expansion coefficient. The in-situ stress can be obtained from XLOT's or mini-fracs, as is also done within the SCAN in various shaly formations; however, no measurements have yet been performed in the geothermal reservoir target. The thermo-elastic parameters ideally require laboratory characterization on samples recovered during drilling, in combination with well log data. For further details on the data gaps, see section 5.5.

- Follow-up modelling of realistic pressure, temperature and stress changes in North Sea Supergroup reservoirs with a reservoir simulator and numerical geomechanical tools. This is important, as the reservoir geology may be quite different from the thinner reservoirs at depth which have a more confined caprock-reservoir-base structure. The outcomes can be used to compare with SRIMA, so that the various assumptions made in the SRIMA tool can be assessed and justified or improved upon.

- Follow-up modelling of inelastic reservoir behaviour. This should contain a laboratory component to determine which material model is best suited to describe the

behaviour of the North Sea Group lithologies under the in-situ conditions, and which input parameters should be used in the modeling. Here it is also important to constrain when shear failure of the material occurs. This is not only relevant for deformation but can also be relevant for sand production. It should also contain a model component to assess the impact of plasticity on the field scale.

- Validation of models with plasticity against field data. Field data that is relevant for calibration is for example Distributed Strain Sensing which can be done by cementing fiber-optic cables along an injection well. Another method may be to perform Pressure Meter Tests in an open hole. During such tests, a packer is inflated and deflated, and volumetric changes of the wellbore are measured from which elastic (and potentially plastic) properties of the wallrock can be derived.

- Evaluate the seismic/aseismic slip potential through laboratory friction experiments (e.g. velocity stepping experiments, slide-hold-slide experiments) on relevant fault gouge materials derived from North Sea Supergroup formations in the RVG, at the in-situ temperature, depth and stress conditions and in-situ fluid composition. The advantage of the relative shallow depth of these formations is that these conditions are easily achieved in a rock mechanics laboratory. The outcome of such a study could lead to a certain depth range which could be derisked with respect of seismic fault reactivation.

- Extending the regional seismic monitoring network and revising relocation algorithms for better depth determination of natural seismicity. This may assist in excluding natural background seismicity in the geothermal target formations.

- Perform local monitoring near active faults in the RVG. This reduces the location uncertainty, leading to a better link between the nucleation depth and certain lithological units.

- Perform monitoring in the vicinity of future geothermal projects to check for conformant behaviour and/or to understand the operational processes at depth. Monitoring of both seismic and aseismic deformation is important, which can be achieved through a combination of microseismic monitoring with geophones and DAS, monitoring deformation with tiltmeters, extensometers, and DSS, and monitoring of surface deformation with INSAR.

- A more audacious, research-oriented approach could be to construct a demonstration site and perform a fault reactivation experiment in the North Sea Supergroup, with all the monitoring described in the previous point. Such a field demonstration, in combination with the laboratory findings, would help to verify the processes that govern the response of the shallow subsurface and so help to derisk the shallow formations.

- Extend model simulations to cover other effects of geothermal operations in shallow formations, such as subsidence (which is likely non-negligible) and caprock integrity.

7 References

(Agurto-Detzel et al., 2017)

References

Atkinson, J. (2017). *The mechanics of soils and foundations* CRC press.

Balsamo, F., Aldega, L., De Paola, N., Faoro, I., & Storti, F. (2014). The signature and mechanics of earthquake ruptures along shallow creeping faults in poorly lithified sediments. *Geology, 42*(5), 435-438.

Batzle, M., & Wang, Z. (1992). Seismic properties of pore fluids. *Geophysics, 57*, 1396-1408.

Baud, P., Vajdova, V., & Wong, T. (2006). Shear-enhanced compaction and strain localization: Inelastic deformation and constitutive modeling of four porous sandstones. *Journal of Geophysical Research: Solid Earth, 111*(B12)

Békési, E., Struijk, M., Bonté, D., Veldkamp, H., Limberger, J., Fokker, P. A., . . . Van Wees, J. D. (2020). An updated geothermal model of the Dutch subsurface based on inversion of temperature data. *Geothermics, 88* doi:10.1016/j.geothermics.2020.101880

Bonté, D., Van Wees, J. D., & Verweij, H. (2012). Subsurface temperature of the onshore Netherlands: new temperature dataset and modelling. *Netherlands Journal of Geosciences, 91*(4), 491-515.

Buijze, L., Fokker, P. A., & Wassing, B. B. T. (2022). Quantification of induced seismicity potential of geothermal operations: Analytical and numerical model approaches. Utrecht: TNO.

Camelbeeck, T., & Van Eck, T. (1994). The Roer Valley Graben earthquake of 13 April 1992 and its seismotectonic setting. *Terra Nova, 6*(3), 291-300.

Cassiani, G., Brovelli, A., & Hueckel, T. (2017). A strain-rate-dependent modified Cam-Clay model for the simulation of soil/rock compaction. *Geomechanics for Energy and the Environment, 11*, 42-51.

Den Haan, E. J., Van Essen, H. M., Visschedijk, M., & Maccabiani, J. (2004). Isotachenmodellen: help hoe kom ik aan de parameters?

Dieterich, J. H. (1979). Modeling of rock friction. 1. Experimental results and constitutive equations. *Journal of Geophysical Research, 84*, 2161.

Fokker, P. A., Buijze, L., & Pluymaekers, M. P. D. (2023). SRIMA: Background Information of Python tool.Retrieved from: https://www.nlog.nl/sites/default/files/2023-11/tno2023_r11303_srima_background_information_of_the_python_tool.pdf

Geel, C. R., de Haan, H., ten Veen, J., Houben, S., Kruisselbrink, A., Foeken, J., Veldkamp, J. G., Peters, E., & van Wees, J. D. (2022). Characterisation of a shallow geothermal resource in The Netherlands: the Brussels Sand Mb. *European Geothermal Congress,* Berlin.

Geluk, M. C., Duin, E. J. T., Dusar, M., Rijkers, R. H. B., & van den Berg, M. W. (1994). Stratigraphy and tectonics of the Roer Valley Graben. *Geologie En Mijnbouw, 73*, 129-141.

Gorjainov, N. N., & Ljachowickij, F. M. (1979). *Seismic Methods in Engineering Geology.* Moscow: Nedra.

Grueschow, E., & Rudnicki, J. W. (2005). Elliptic yield cap constitutive modeling for high porosity sandstone. *International Journal of Solids and Structures, 42*(16-17), 4574-4587.

Han, R., Kim, C. M., Woo, S., Jeong, G. Y., & Hirose, T. Structural records and mechanical characteristics of seismic slip along an active fault crosscutting unconsolidated Quaternary sediments: Suryum fault, SE Korea. *Geosciences Journal, 24*, 379-389.

Hantschel, T., & Kauerauf, A. I. (2009). *Fundamentals of Basin and Petroleum Systems Modeling* Springer. doi:10.1007/978-3-540-72318-9

Heederik, J. P., Brugge, J., Brummer, C. H., Coenegracht, Y. M. A., van Doorn, T. H. M., Huurdeman, A. J. M., . . . Zuurdeeg, B. W. (1989). Geothermische reserves Centrale Slenk, Nederland. Report OS 89-19 Delft: TNO-DGV.

Hinzen, K. G., Reamer, S. K., & Fleischer, C. (2020). Seismicity in the Northern Rhine Area (1995–2018). *Journal of Seismology, 25*, 351-367.

Houtgast, R. F., van Balen, R. T., & Kasse, C. (2005). Late Quaternary evolution of the Feldbiss Fault (Roer Valley Rift System, the Netherlands) based on trenching, and its potential relation to glacial unloading. . *Quaternary Science Reviews, 24*(3-4), 489-508.

Hummelman, H. J., Maljers, D., Menkovic, A., Reindersma, R., Vernes, R., & Stafleu, J. (2019). Totstandkomingsdocument Hydrogeologisch Model (REGIS II). Report R11654 Utrecht: TNO. Retrieved from: https://www.dinoloket.nl/sites/default/files/Totstandkomingsrapport-REGIS-II.pdf

Hunfeld, L. B. (2020). *Frictional properties of simulated fault gouges from the groningen gas field and implications for induced seismicity*

Hutka, G. A., Cacace, M., Hofmann, H., Mathur, B., & Zang, A. (2023). Investigating seismicity rates with Coulomb failure stress models caused by pore pressure and thermal stress from operating a well doublet in a generic geothermal reservoir in the Netherlands. *Netherlands Journal of Geosciences, 102*, e8. doi:10.1017/njg.2023.7

Kirsch, C. (1898). Die theorie der elastizitat und die bedurfnisse der festigkeitslehre. *Zeitschrift Des Vereines Deutscher Ingenieure, 42*, 797-807.

Kivi, I. R., Pujades, E., Rutqvist, J., & Vilarrasa, V. (2022). Cooling-induced reactivation of distant faults during long-term geothermal energy production in hot sedimentary aquifers. *Scientific Reports, 12*(1), 1-13.

Kombrink, H., Doornenbal, J. C., Duin, E. J. T., Den Dulk, M., ten Veen, J. H., & Witmans, N. (2012). New insights into the geological structure of the Netherlands; results of a detailed mapping project. *Netherlands Journal of Geosciences, 91*(04), 419-446. doi:https://doi.org/10.1017/S0016774600000329

Luijendijk, E., van Balen, R. T., ter Voorde, M., & Andriessen, P. A. M. (2011). Reconstructing the Late Cretaceous inversion of the Roer Valley Graben (southern Netherlands) using a new model that integrates burial and provenance history with fission track

thermochronology. *Journal of Geophysical Research, 116*, 1-19. doi:10.1029/2010JB008071

Mathur, B., Hofmann, H., Cacace, M., Hutka, G. A., & Zang, A. (2024). Thermo-hydro-mechanical simulation of cooling-induced fault reactivation in Dutch geothermal reservoirs. *Netherlands Journal of Geosciences, 103*, e1.

Mavko, G., Mukerji, T., & Dvorkin, J. (2020). *The rock physics handbook* Cambridge university press.

Mechelse, E. (2017). *The in-situ stress field in the netherlands: Regional trends, local deviations and an analysis of the stress regimes in the northeast of the netherlands*

Mese, A., & Dvorkin, J. (2000). Static and Dynamic Moduli, Deformation and Failure in Shaley-sand. *DOE Report,*

Michon, L., & van Balen, R. T. (2006). Characterization and quantification of active faulting in the Roer valley rift system based on high precision digital elevation models. *Quaternary Science Reviews, 24*(3-4), 457–474.

Mijnlieff, H., de Vries, S., Jaarsma, B. en Vogelaar, B. (2023) Seismische dreigings- en risicoanalyse voor aardwarmteprojecten in Nederland. Rapport versie 16 november 2023.

Morawietz, S., Heidbach, O., Reiter, K., Ziegler, M., Rajabi, M., Zimmermann, G., . . . Tingay, M. (2020). An open-access stress magnitude database for Germany and adjacent regions. *Geothermal Energy, 8*, 1-39.

Munda, J., Pradhan, P. K., & Nayak, A. K. (2014). Review on the performance of Modified Cam Clay Model for fine grained soil. *Journal of Civil Engineering and Environmental Technology, 1*(5), 65-71.

Munsterman, D. K., ten Veen, J. H., Menkovic, A., Deckers, J., Witmans, N., Verhaegen, J., . . . Busschers, F. S. (2019a). An updated and revised stratigraphic framework for the Miocene and earliest Pliocene strata of the Roer Valley Graben and adjacent blocks. *Netherlands Journal of Geosciences, 98*

Munsterman, D. K., ten Veen, J. H., Menkovic, A., Deckers, J., Witmans, N., Verhaegen, J., . . . Busschers, F. S. (2019b). An updated and revised stratigraphic framework for the Miocene and earliest Pliocene strata of the Roer Valley Graben and adjacent blocks. *Netherlands Journal of Geosciences, 98*

NEN. (2012). National Annex to NEN-EN 1997-1 Eurocode 7: Geotechnical design - Part 1: General rules.

Nguyen, V. H., Gland, N., Dautriat, J., David, C., Wassermann, J., & Guelard, J. (2014). Compaction, permeability evolution and stress path effects in unconsolidated sand and weakly consolidated sandstone. *International Journal of Rock Mechanics and Mining Sciences, 67*, 226-239.

Osinga, S., & Buik, N. (2019). Stress field characterization in the Dinantian carbonates in the Dutch subsurface.EZK, EBN, TNO, Interreg.

Panterra. (2021). Seismic Hazard Screening (SHS): Larger Roer valley graben area definition.

Peters, E., Foeken, J. P. T., Geel, C. R., & Veldkamp, J. G. (2022). Characterization of and production from the Breda Formation in the Roer Valley Graben. Utrecht: TNO. Retrieved from: https://www.warmingup.info/documenten/breda-report_20230120_final_hr.pdf

Pijnenburg, R. P. J. (2019). *Deformation behavior of reservoir sandstones from the seismogenic groningen gas field; an experimental and mechanistic study*

Pijnenburg, R. P. J., Hangx, S. J. T., & Spiers, C. J. (2019). Inelastic deformation of the Slochteren sandstone: Stress-strain relations and implications for induced seismicity in the Groningen gas field. *Journal of Geophysical Research: Solid Earth, 124*(5), 5254-5282. doi:10.1029/2019JB017366

Rabinowitz, H. S., Savage, H. M., Skarbek, R. M., Ikari, M. J., Carpenter, B. M., & Collettini, C. (2018). Frictional behavior of input sediments to the Hikurangi Trench, New Zealand. *Geochemistry, Geophysics, Geosystems, 19*(9), 2973-2990.

Roscoe, K. H., & Burland, J. B. (1968). On the generalized stress-strain behaviour of wet clay. In L. Heyman, & F. A. Leckie (Eds.), *Engineering plasticity* (pp. 535-609). Cambridge: Cambridge University Press.

Rubin, A. M., & Ampuero, J. (2005). Earthquake nucleation on (aging) rate and state faults. *Journal of Geophysical Research: Solid Earth, 110*(B11), B11312. doi:10.1029/2005JB003686

Ruigrok, E., Kruiver, P., & Dost, B. (2023). Construction of earthquake location uncertainty maps for the Netherlands. Technical Report, number: TR-405. de Bilt: KNMI.

Ruina, A. (1983). Slip Instability and State Variable Friction Laws. *Journal of Geophysical Research, 88*(370), 10.

Scholz, C. H. (1988). The brittle-plastic transition and the depth of seismic faulting. *Geologische Rundschau, 77*, 319-328.

Seyler, C. E., Kirkpatrick, J. D., Savage, H. M., Hirose, T., & Faulkner, D. R. (2020). Rupture to the trench? Frictional properties and fracture energy of incoming sediments at the Cascadia subduction zone. *Earth and Planetary Science Letters, 546*, 116413.

Siebels, A., ten Veen, J., Munsterman, D., Deckers, J., Kasse, C., & van Balen, R. (2024). Miocene sequences and depocenters in the Roer Valley Rift system. *Basin Research,* , 1-33. doi:10.1111/bre.12886

Smit, F. (2022). *An overlooked aquifer in the netherlands: Medium depth geothermal potential of the breda formation in the zuiderzee low*

SODM. (2016). Methodiek voor risicoanalyse omtrent geïnduceerde bevingen voor gaswining - Tijdelijke leidraad voor adressering MBB. Report ERSIE 1.2 Den Haag: State Supervision of Mines.

Somerton, W. H. (1992). *Thermal properties and temperature-related behavior of rock/fluid systems*. Amsterdam u.a: Elsevier.

Soustelle, V., ter Heege, J., Buijze, L., & Wassing, B. (2022). Thermomechanical parameters of geothermal analogue reservoir sandstones in the West Netherlands Basin. WarmingUp report. Utrecht:

Spetzler, J. (2023). Hypocenters for the events between March and May 2023 near Klimmen. Technical Report, number: TR-404. de Bilt: KNMI.

TNO. (2020). Probabilistic seismic hazard and risk analysis in the TNO model chain Groningen. Report TNO2020 R11052 Utrecht, the Netherlands: TNO. doi:https://kemprogramma.nl/file/download/57979610/tno2020-r11052-wvd-pshra-tno-model-chain-groningen-gelakt.pdf

van Balen, R. T., Bakker, M. A. J., Kasse, C., Wallinga, J., & Woolderink, H. A. G. (2019). A late glacial surface rupturing earthquake at the Peel boundary fault zone, Roer Valley Rift System, the Netherlands. . *Quaternary Science Reviews, 218*, 254-266.

van Balen, R. T., Kasse, C., Wallinga, J., & Woolderink, H. A. G. (2021). .Middle to Late Pleistocene faulting history of the Heerlerheide fault, Roer Valley Rift System, influenced by glacio-isostasy and mining-induced displacement. *Quaternary Science Reviews, 268*

van Balen, R. T., Lapperre, R. E., Woolderink, H. A. G., Wallinga, J., & Kasse, C. (2024). Magnitudes and surface rupture lengths of paleo-earthquakes at the NW-part of the Peel Boundary fault zone, Roer Valley Rift System. *Tectonophysics, 230322*

van Doorn, T., Leyzers-Vis, C., Salomons, N., van Dalfsen, W., Speelman, H., & Zijl, W. (1985). Aardwarmtewinning en grootschalige warmte-opslag in Tertiaire en Onder-Kwartaire afzettingen. Report 85KAR02EX Haarlem: Rijks Geologische Dienst.

Van Eck, T., Goutbeek, F., Haak, H., & Dost, B. (2006). Seismic hazard due to small-magnitude, shallow-source, induced earthquakes in The Netherlands. *Engineering Geology, 87*, 105. doi:10.1016/j.enggeo.2006.06.005

van Eekelen, S. J., & van den Berg, P. (1994). The delft egg model, a constitutive model for clay. *DIANA Computational Mechanics '94: Proceedings of the First International Diana Conference on Computational Mechanics,* Springer,

Veldkamp, J. G., & Hegen, D. (2020). Temperature modelling of the Dutch subsurface at the depth of the Dinantian (downloadable from https://nlog.nl/en/scan). Utrecht: SCAN.

Vernes, R. W., & van Doorn, T. H. M. (2005). Van gidslaag naar hydrogeologische eenheid. Toelichting op de totstandkoming van de dataverzameling REGIS II. Report 05-038-B Utrecht: TNO-NITG.

Verweij, J. M., & Hegen, D. (2015). Integrated pressure information system for the onshore and offshore Netherlands. Report TNO 2015 R10056 Utrecht, The Netherlands: TNO.

Vivas, C., Hu, Z., & Salehi, S. (2023). Texture-Dependent Thermal Properties of Sandstone Rocks Examined by Scanning Electron Microscopy for Thermal Energy Storage Applications. *ASME Open Journal of Engineering, 2*

Vörös, R., & Baisch, S. (2022). Induced seismicity and seismic risk management – a showcase from the Californië geothermal field (the Netherlands). *Netherlands Journal of Geosciences, 101*, e15. doi:10.1017/njg.2022.12

Wang, Z., & Nur, A. (2000). *Seismic and Acoustic Velocities in Reservoir Rocks, vol. 3, Recent Developments*. Tulsa, OK: Society of Exploration Geophysicists.

Wong, T., David, C., & Zhu, W. (1997). The transition from brittle faulting to cataclastic flow in porous sandstones: Mechanical deformation. *Journal of Geophysical Research: Solid Earth, 102*(B2), 3009-3025.

Wood, D. M. (1990). *Soil Behaviour and Critical State Soil Mechanics* Cambridge University Press.

Zijerveld, L., Stephenson, R., Cloetingh, S., Duin., E., van den, & Berg, M. W. &. (1992). Subsidence analysis and modelling of the Roer Valley Graben. *Tectonophysics, 208*, 159-171.

Appendix A Main lithostratigraphic units where geothermal potential exists in the RVG

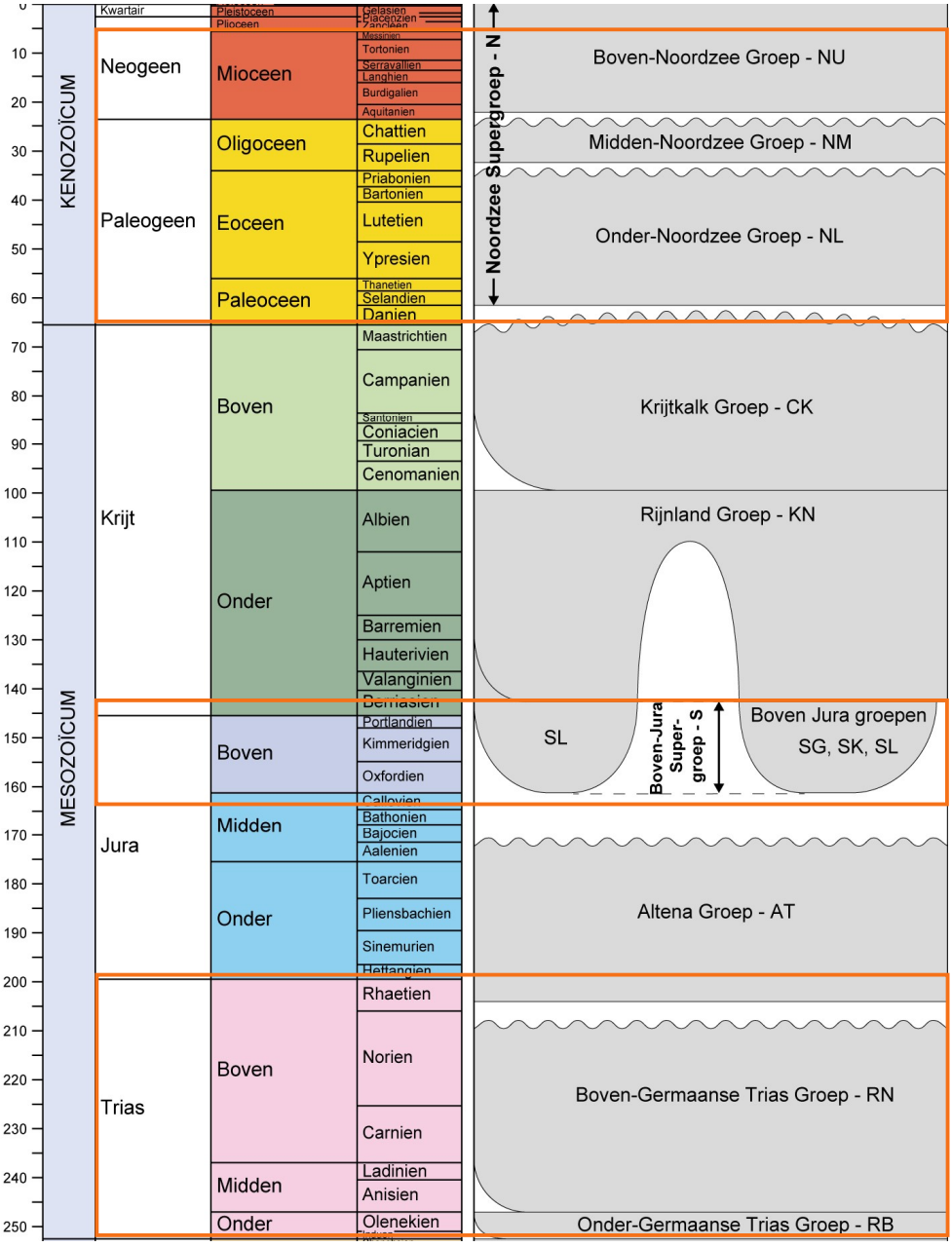

Appendix B Chronostratigraphy and lithostratigraphic units in the North Sea Group in the RVG

Chronostratigraphy (time scale non-linear)				North Sea Supergroup stratigraphic units (formation level)				
					Marine	Fluvial		
						Eastern rivers	Rhine	Meuse
Cenozoic	Quaternary	Holocene		Upper North Sea Group	Naaldwijk Formation		Echteld Formation	Beegden Formation
		Pleistocene	Upper				Kreftenheye Formation	
					Eem Formation		Urk Formation	
			Middle			Appelscha Formation	Sterksel Formation	
			Calabrian					
						Peize Formation	Waalre Formation	
			Gelasian		Maassluis Formation			
	Neogene	Pliocene			Oosterhout Formation		Kiezeloolite Formation	
		Miocene			Breda Formation		Inden Formation	
				Middle North Sea Group	Veldhoven Formation			
	Paleogene	Oligocene			Rupel Formation			
					Tongeren Formation			
		Eocene		Lower North Sea Group	Dongen Formation			
		Paleocene			Landen Formation			

Note that the now obsolete Tertiary spans the Paleogene and Neogene

Appendix C Potential geothermal reservoirs in the RVG

This study focuses on the Breda Formation. In the RVG, Geothermal potential is recognized more aquifers, mostly of Paleogene age or older (Figure 59 Figure 59). Only a brief description is provided here. Because the Paleogene units were not targeted by the few exploration wells which were aimed at older units, no detailed descriptions of the lithostratigraphy exist for these units in the RVG.

- In the central part of the RVG (mostly between Eindhoven and Roermond), in various aquifers of Paleogene age (Table 12).
- In the northwestern part (around Waalwijk and between Den Bosch and Veghel), potential is expected in sediments belonging to the Nieuwerkerk Formation (Delft/Alblasserdam Members).
- Along the northeastern edges (Culemborg – Zaltbommel) and southwestern (Breda – Weert) and in the southeast (between Helmond and Weert), geothermal potential possibly exists in aquifers of Triassic age.

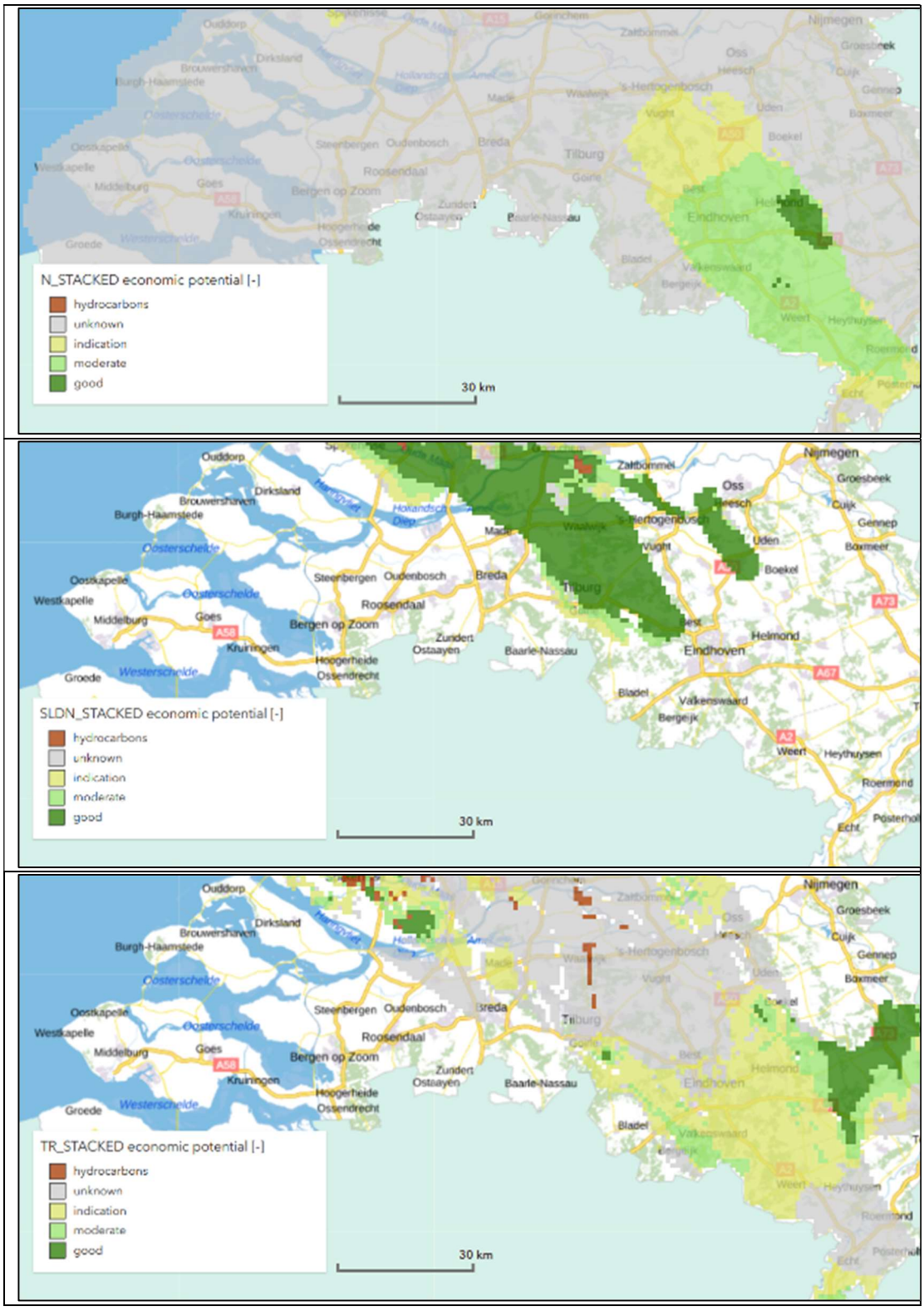

Figure 59 Currently recognized geothermal potential in the Roer Valley Graben in aquifers of Triassic, Jurassic and Paleogene age (base to top). Source: www.thermogis.nl.

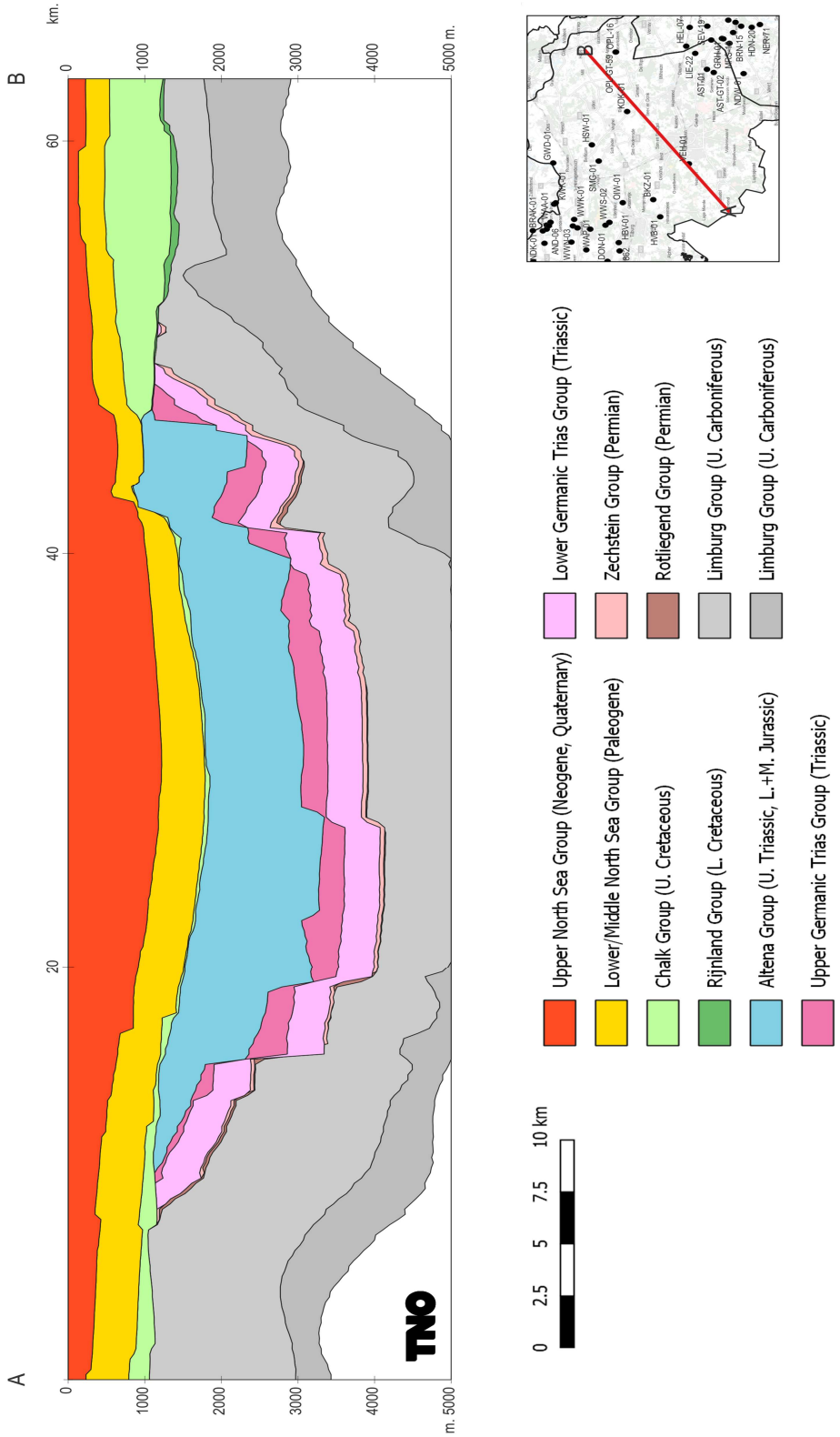

Figure 60 Cross section over the RVG showing units distribution. Neogene in red, Paleogene in yellow. Source: DGM-Deep v5.

In the RVG thick successions of rocks belonging to the Altena Group exist between ~1200 and ~3000m (Figure 60), but those rocks are not recognized as potential aquifers because they consist mostly of marl and shale.
Younger units of Miocene to early Pleistocene age (Breda, Oosterhout, Maassluis and younger) were not considered in ThermoGIS because of their generally shallow burial and therefore low temperature. Recent studies ((Smit, 2022; Peters et al., 2022)) suggest that the Breda Formation offers geothermal potential where it is buried relatively deeply, such as the Roer Valley Graben (Table 12). A preliminary view on the geothermal potential of a part of the RVG is shown on the ThermoGIS website (https://www.thermogis.nl/en/breda-formation)

Table 12 Paleogene and Neogene aquifers with geothermal potential in the RVG.

Group name	Group code	Formation name	Formation code	Member name	Member code
Upper North Sea Group	NU	Breda Formation	NUBR	(Groote Heide / Diessen)*	*
Middle North Sea Group	NM	Veldhoven Formation	NMVE	Someren Member	NMVESO
				Voort Member	NMVEVO
		Rupel Formation	NMRU	Steensel Member	NMRUST
				Berg Member	NMRUBE
Lower North Sea Group	NL	Dongen Formation	NLDO	Oosteind Member	NLDOOO
		Landen Formation	NLLA	Reusel Member	NLLARE
				Orp Member	NLLAOR

* (Munsterman et al., 2019a) propose to split the Breda Formation in a lower Groote Heide and upper Diessen Formation. This new stratigraphy is not yet implemented in the Stratigraphic Nomenclator of the Netherlands but will be followed in this report.

The (technical) geothermal potential of all Lower and Middle North Sea Group units shown in Appendix A was calculated in ThermoGIS (www.thermogis.nl) using data on depth, thickness, net-to-gross, permeability and temperature, and a standardized doublet layout.
Figure 61 shows that the Paleogene aquifers reach their maximum thickness in the southeastern part of the RVG, between Eindhoven and Weert. Appendix shows maps of the top depth and thickness of the nine aquifers listed in Table 12. The Groote Heide and Diessen aquifers were mapped on seismic and gridded on 50x50m (unpublished), while the aquifers in the Middle and Lower North Sea Groups were mapped using interpolated depths and thicknesses from well data which were then stacked on top of the DGM-Deep v5 base North Sea Group grid.

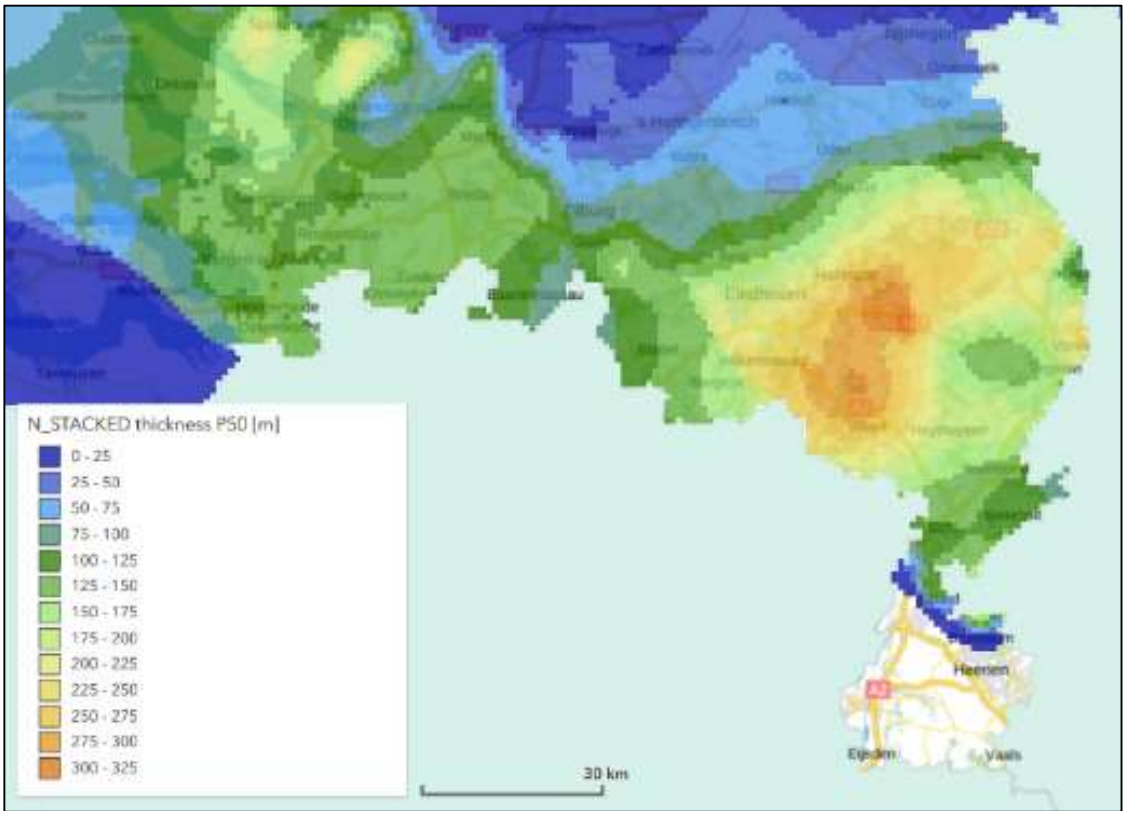

Figure 61 Cumulative thickness of the Paleogene aquifers in the Roer Valley Graben. Source: www.thermogis.nl

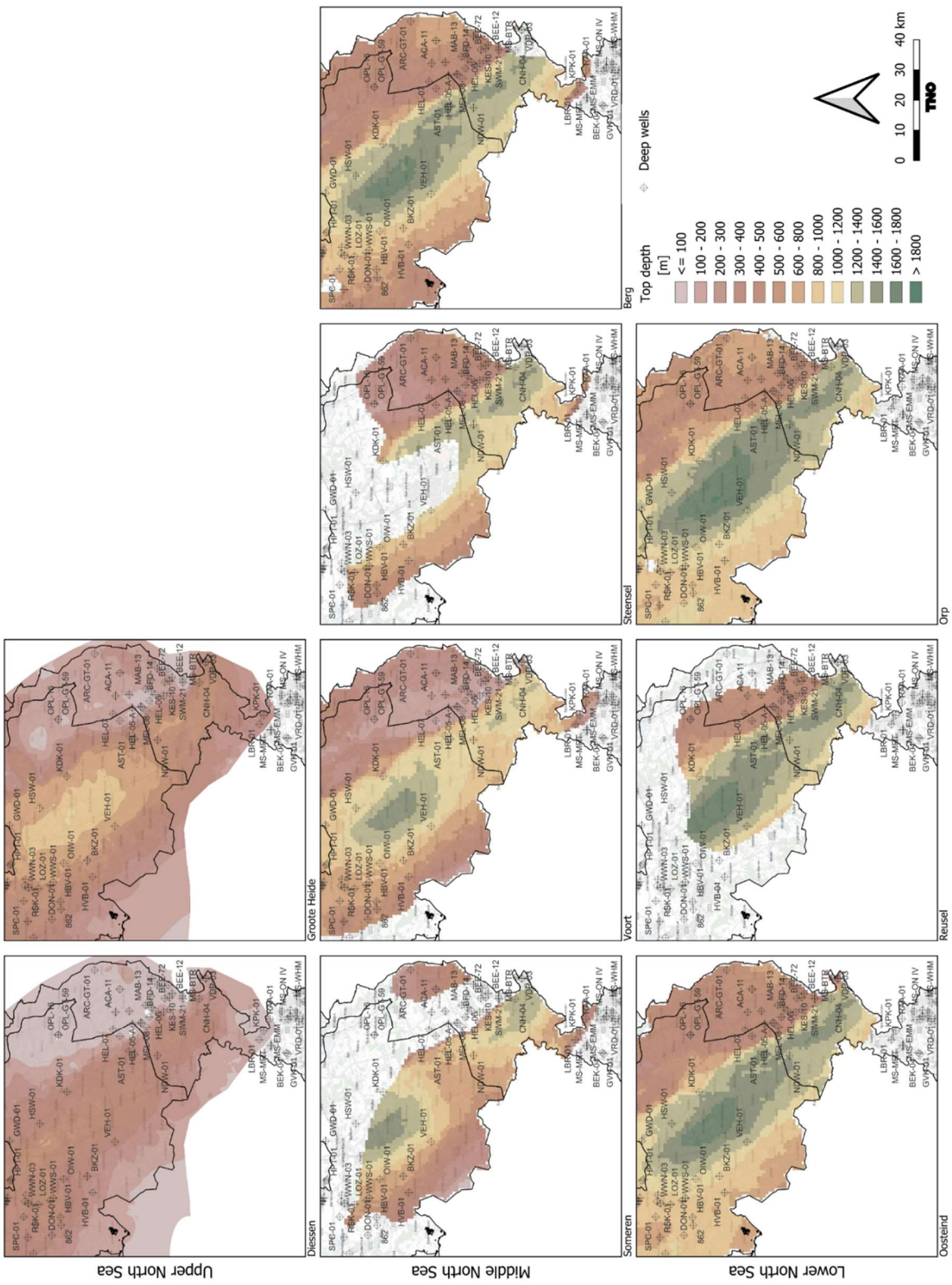

Figure 62 Top depth of the nine stratigraphic units in the North Sea Supergroup in which geothermal potential is recognized.

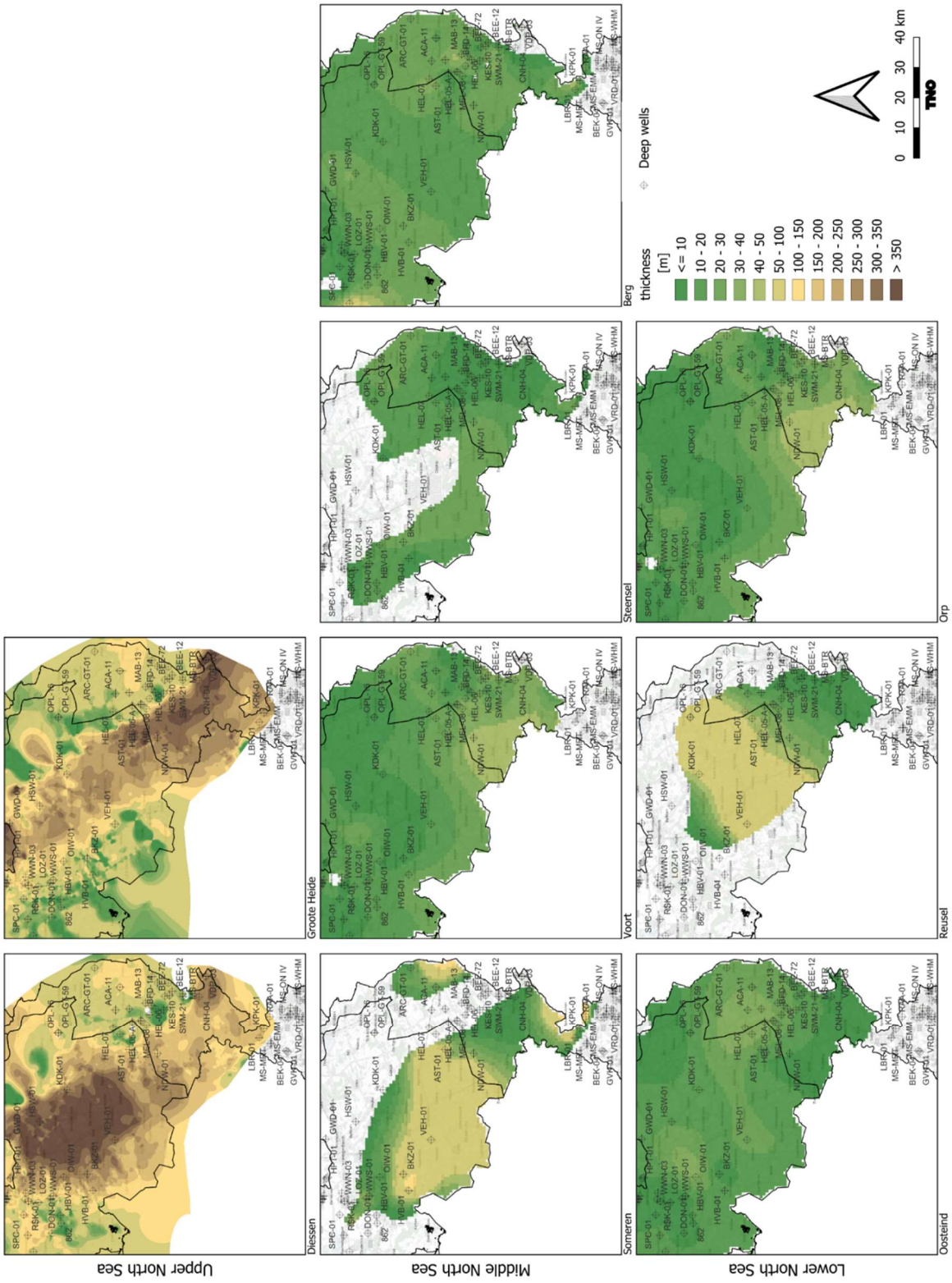

Figure 63 Thickness of the nine stratigraphic units in the North Sea Supergroup in which geothermal potential is recognized.

Appendix D Depth and thickness of the Groote Heide and Diessen Formations

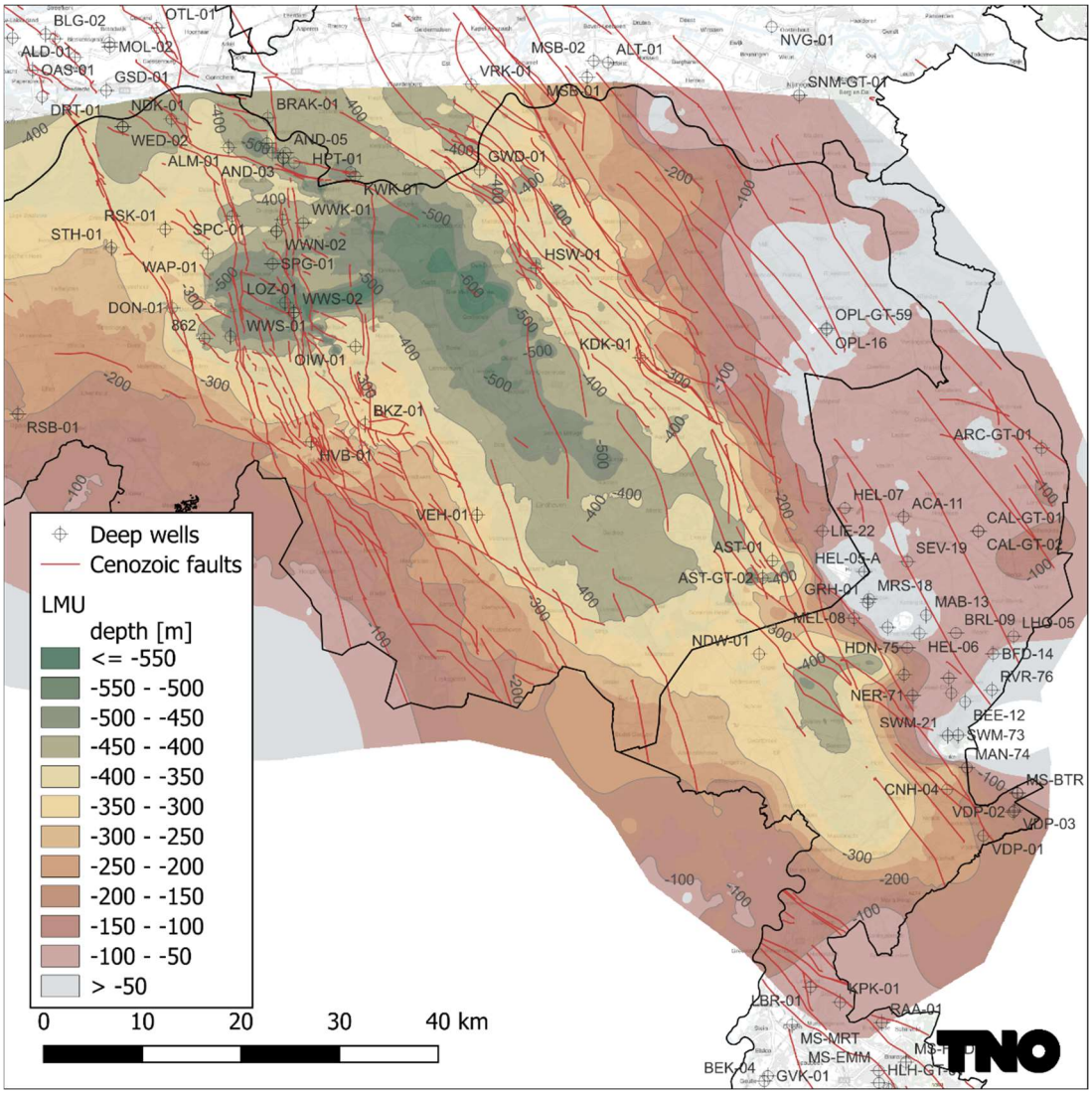

Figure 64: Top depth Diessen Formation (Late Miocene Unconformity)

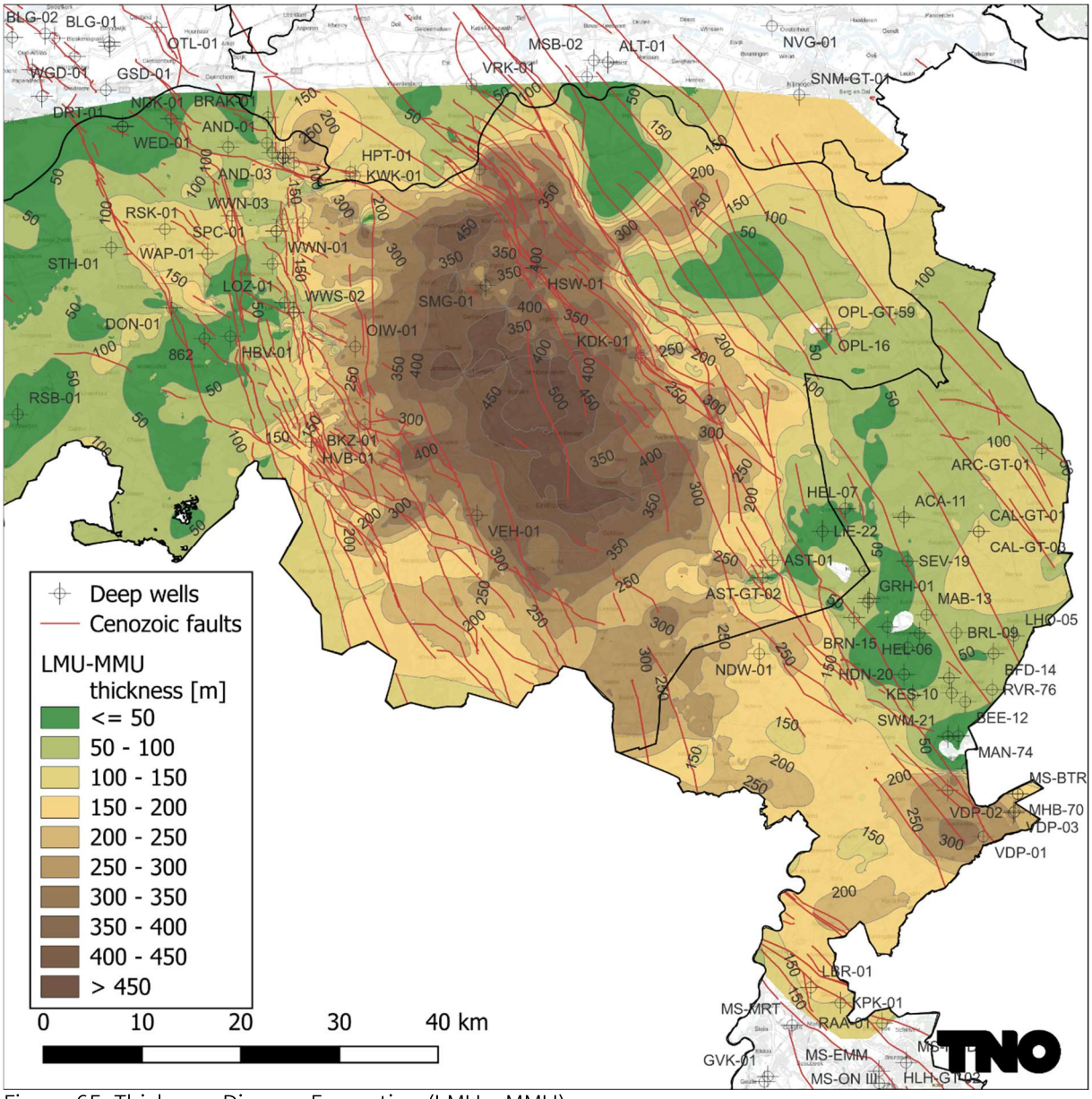

Figure 65: Thickness Diessen Formation (LMU – MMU)

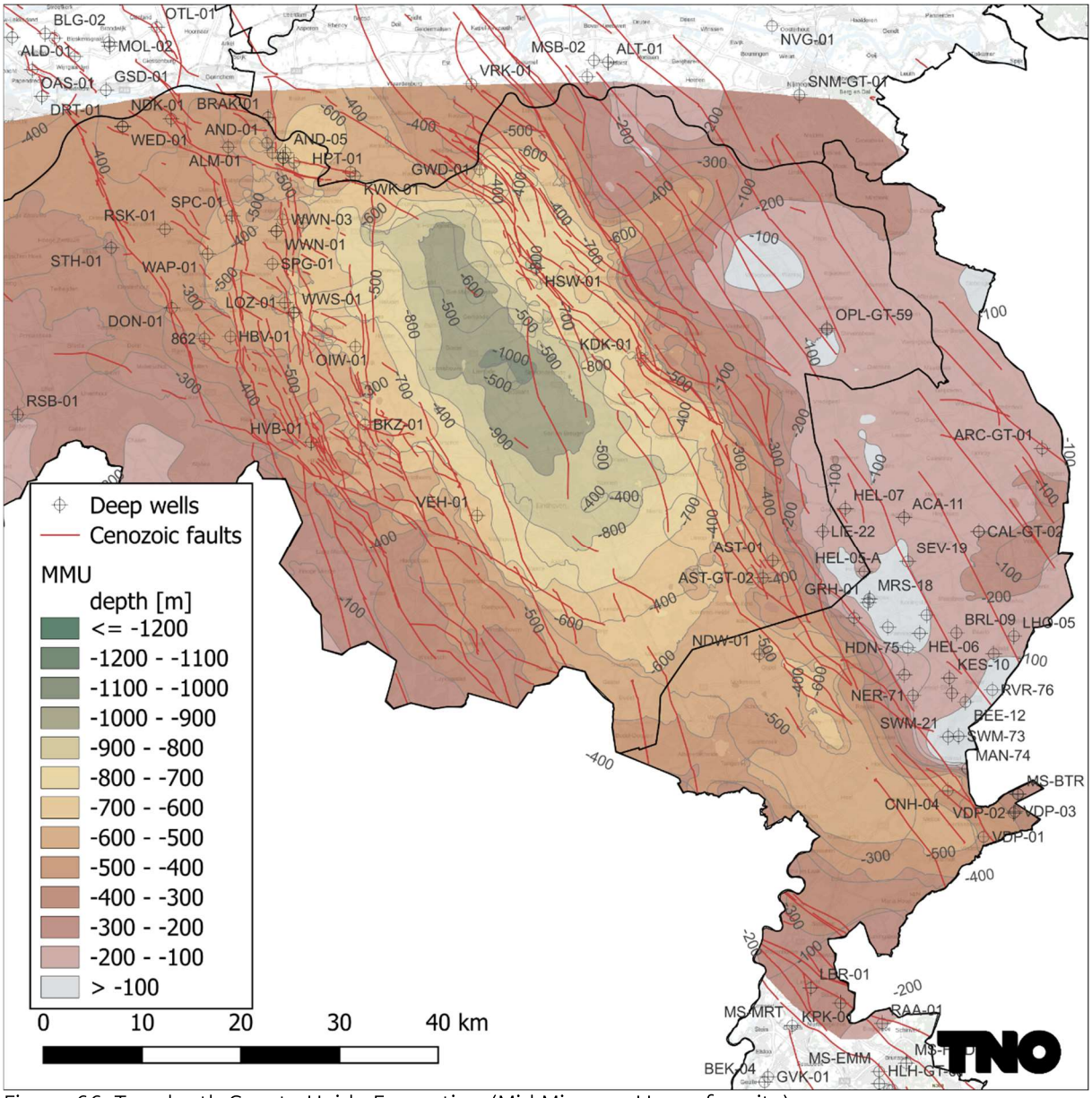

Figure 66: Top depth Groote Heide Formation (Mid Miocene Unconformity)

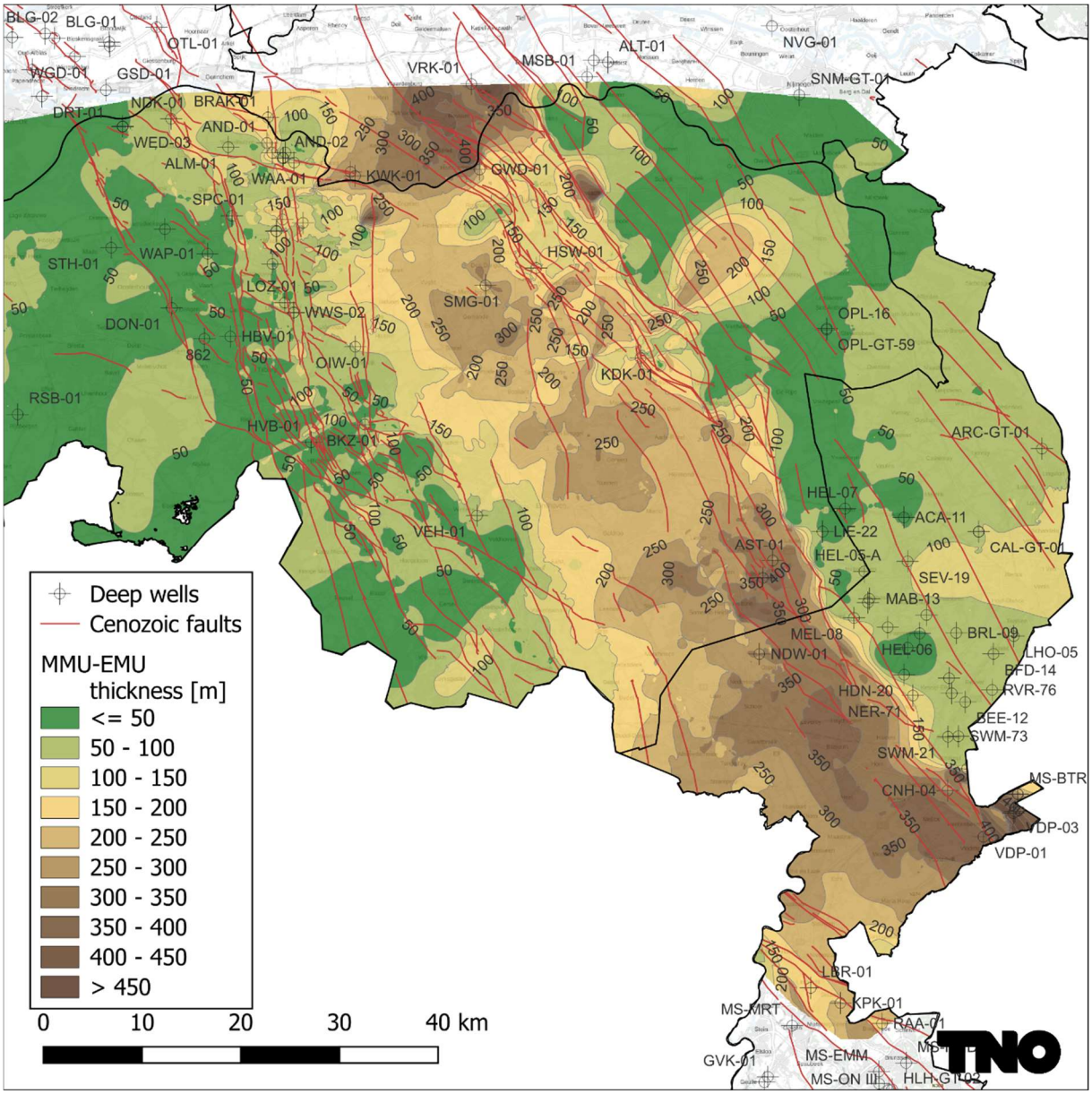

Figure 67: Thickness Groote Heide Formation (MMU – EMU)

Energy & Materials Transition

Princetonlaan
3584 CB Utrecht
www.tno.nl